

# **Flight-Determined, Subsonic, Lateral-Directional Stability and Control Derivatives of the Thrust-Vectoring F-18 High Angle of Attack Research Vehicle (HARV), and Comparisons to the Basic F-18 and Predicted Derivatives**

*Kenneth W. Iliff  
Dryden Flight Research Center  
Edwards, California*

*Kon-Sheng Charles Wang  
SPARTA, Incorporated  
Lancaster, California*



## The NASA STI Program Office . . . in Profile

Since its founding, NASA has been dedicated to the advancement of aeronautics and space science. The NASA Scientific and Technical Information (STI) Program Office plays a key part in helping NASA maintain this important role.

The NASA STI Program Office is operated by Langley Research Center, the lead center for NASA's scientific and technical information. The NASA STI Program Office provides access to the NASA STI Database, the largest collection of aeronautical and space science STI in the world. The Program Office is also NASA's institutional mechanism for disseminating the results of its research and development activities. These results are published by NASA in the NASA STI Report Series, which includes the following report types:

- **TECHNICAL PUBLICATION.** Reports of completed research or a major significant phase of research that present the results of NASA programs and include extensive data or theoretical analysis. Includes compilations of significant scientific and technical data and information deemed to be of continuing reference value. NASA's counterpart of peer-reviewed formal professional papers but has less stringent limitations on manuscript length and extent of graphic presentations.
- **TECHNICAL MEMORANDUM.** Scientific and technical findings that are preliminary or of specialized interest, e.g., quick release reports, working papers, and bibliographies that contain minimal annotation. Does not contain extensive analysis.
- **CONTRACTOR REPORT.** Scientific and technical findings by NASA-sponsored contractors and grantees.
- **CONFERENCE PUBLICATION.** Collected papers from scientific and technical conferences, symposia, seminars, or other meetings sponsored or cosponsored by NASA.
- **SPECIAL PUBLICATION.** Scientific, technical, or historical information from NASA programs, projects, and mission, often concerned with subjects having substantial public interest.
- **TECHNICAL TRANSLATION.** English-language translations of foreign scientific and technical material pertinent to NASA's mission.

Specialized services that complement the STI Program Office's diverse offerings include creating custom thesauri, building customized databases, organizing and publishing research results . . . even providing videos.

For more information about the NASA STI Program Office, see the following:

- Access the NASA STI Program Home Page at <http://www.sti.nasa.gov>
- E-mail your question via the Internet to [help@sti.nasa.gov](mailto:help@sti.nasa.gov)
- Fax your question to the NASA Access Help Desk at (301) 621-0134
- Telephone the NASA Access Help Desk at (301) 621-0390
- Write to:  
NASA Access Help Desk  
NASA Center for AeroSpace Information  
7121 Standard Drive  
Hanover, MD 21076-1320



# **Flight-Determined, Subsonic, Lateral-Directional Stability and Control Derivatives of the Thrust-Vectoring F-18 High Angle of Attack Research Vehicle (HARV), and Comparisons to the Basic F-18 and Predicted Derivatives**

*Kenneth W. Iliff  
Dryden Flight Research Center  
Edwards, California*

*Kon-Sheng Charles Wang  
SPARTA, Incorporated  
Lancaster, California*

National Aeronautics and  
Space Administration

Dryden Flight Research Center  
Edwards, California 93523-0273

## NOTICE

Use of trade names or names of manufacturers in this document does not constitute an official endorsement of such products or manufacturers, either expressed or implied, by the National Aeronautics and Space Administration.

Available from the following:

NASA Center for AeroSpace Information (CASI)  
7121 Standard Drive  
Hanover, MD 21076-1320  
(301) 621-0390

National Technical Information Service (NTIS)  
5285 Port Royal Road  
Springfield, VA 22161-2171  
(703) 487-4650

# CONTENTS

	<u>Page</u>
ABSTRACT .....	1
NOMENCLATURE .....	1
INTRODUCTION .....	6
VEHICLE DESCRIPTION .....	8
Hardware Configuration .....	8
Thrust-Vectoring Control System .....	10
Software Configuration .....	11
Controls Laws .....	12
Thrust-Vectoring Mixer .....	13
INSTRUMENTATION AND DATA ACQUISITION .....	14
METHODS OF ANALYSIS .....	15
Parameter Identification Formulation .....	16
Equations of Motion .....	18
RESULTS AND DISCUSSION .....	21
High Angle of Attack Research Vehicle Stability and Control Maneuvers .....	21
Stability and Control Derivative Results .....	24
HARV Derivatives .....	24
Comparison of HARV and Basic F-18 Derivatives .....	29
Summary of HARV, Basic F-18, and Predicted Derivatives .....	35
CONCLUSIONS .....	35
REFERENCES .....	38
FIGURES .....	43

## TABLES

1. F-18 aerodynamic control surface position and rate limits .....	9
2. F-18 HARV thrust-vectoring vane system specifications .....	10
3. Comparison of unmodified and modified F-18 HARV .....	11
4. Summary of OBES-commanded control input amplitudes .....	22

## FIGURES

1. F-18 High Angle of Attack Research Vehicle (HARV) .....	43
2. Three-view drawing of the F-18 HARV with major dimensions shown .....	44
3. Thrust-vectoring control system (TVCS) hardware modification .....	45
4. Four-view drawing of the TVCS .....	46
5. The maximum likelihood estimation concept with state and measurement noise .....	47
6. Time history data from a typical 10° AOA lateral-directional PID maneuver .....	48
7. Time history data from a typical 30° AOA lateral-directional PID maneuver .....	52
8. HARV sideslip derivatives as functions of AOA .....	56
9. HARV differential horizontal stabilator derivatives as functions of AOA .....	57
10. HARV aileron derivatives as functions of AOA .....	59
11. HARV rudder derivatives as functions of AOA .....	60
12. HARV rotary derivatives as functions of AOA .....	62
13. HARV thrust-vectoring derivatives as functions of AOA .....	64
14. HARV aerodynamic biases as functions of AOA .....	65
15. Basic F-18 and HARV sideslip derivatives as functions of AOA .....	67
16. Basic F-18 and HARV equivalent lateral control derivatives as functions of AOA and basic F-18 control input waveforms. ....	68
17. Basic F-18 and HARV rudder derivatives as functions of AOA .....	71
18. Basic F-18 and HARV rotary derivatives as functions of AOA .....	72
19. Prediction and HARV sideslip derivatives as functions of AOA .....	74
20. Prediction and HARV equivalent lateral control derivatives as functions of AOA .....	76
21. Prediction and HARV rudder derivatives as functions of AOA .....	77
22. Prediction and HARV rotary derivatives as functions of AOA .....	79
23. Prediction and HARV differential horizontal stabilator derivatives as functions of AOA .....	81
24. Prediction and HARV aileron derivatives as functions of AOA .....	82

## ABSTRACT

The subsonic, lateral-directional, stability and control derivatives of the thrust-vectoring F-18 High Angle of Attack Research Vehicle (HARV) are extracted from flight data using a maximum likelihood parameter identification technique. State noise is accounted for in the identification formulation and is used to model the uncommanded forcing functions caused by unsteady aerodynamics. Preprogrammed maneuvers provided independent control surface inputs, eliminating problems of identifiability related to correlations between the aircraft controls and states. The HARV derivatives are plotted as functions of angles of attack between  $10^\circ$  and  $70^\circ$  and compared to flight estimates from the basic F-18 aircraft and to predictions from ground and wind-tunnel tests. Unlike maneuvers of the basic F-18 aircraft, the HARV maneuvers were very precise and repeatable, resulting in tightly clustered estimates with small uncertainty levels. Significant differences were found between flight and prediction; however, some of these differences may be attributed to differences in the range of sideslip or input amplitude over which a given derivative was evaluated, and to differences between the HARV external configuration and that of the basic F-18 aircraft, upon which most of the prediction was based. Some HARV derivative fairings have been adjusted using basic F-18 derivatives (with low uncertainties) to help account for differences in variable ranges and the lack of HARV maneuvers at certain angles of attack.

## NOMENCLATURE

### Acronyms

ANSER	Actuated Nose Strakes for Enhanced Rolling
AOA	angle of attack, deg
CFD	computational fluid dynamics
CG	center of gravity
DPRAM	dual-port random access memory
FCC	flight control computer
FCS	flight control system
HARV	High Angle of Attack Research Vehicle
HATP	High Angle of Attack Technology Program
LEF	leading-edge flap
LEX	leading-edge extension
MAC	mean aerodynamic chord, ft
MC	mission computer
OBES	onboard excitation system

PCM	pulse code modulation
PID	parameter identification
RFCS	research flight control system
SSI	single-surface input
TEF	trailing-edge flap (also used as a subscript)
TVCS	thrust-vectoring control system

## Symbols

$a_Y$	lateral acceleration, g
<b>A, B, C</b>	system matrices
<b>D, F, G</b>	
$b$	reference span, ft
$c$	reference chord, ft
$C_A$	coefficient of axial force
$C_l$	coefficient of rolling moment
$C_{l_p}$	coefficient of rolling moment due to roll rate, $\text{rad}^{-1}$
$C_{l_r}$	coefficient of rolling moment due to yaw rate, $\text{rad}^{-1}$
$C_{l_0}$	rolling moment bias
$C_{l_\beta}$	coefficient of rolling moment due to angle of sideslip, $\text{deg}^{-1}$
$C_{l_{\delta_a}}$	coefficient of rolling moment due to aileron deflection, $\text{deg}^{-1}$
$C_{l_{\delta_{dh}}}$	coefficient of rolling moment due to differential horizontal stabilator deflection, $\text{deg}^{-1}$
$C_{l_{\delta_L}}$	coefficient of rolling moment due to equivalent lateral control deflection, $\text{deg}^{-1}$
$C_{l_{\delta_{pv}}}$	coefficient of rolling moment due to pitch vane deflection, $\text{ft/deg}$
$C_{l_{\delta_r}}$	coefficient of rolling moment due to rudder deflection, $\text{deg}^{-1}$
$C_{l_{\delta_{yv}}}$	coefficient of rolling moment due to yaw vane deflection, $\text{ft/deg}$
$C_m$	coefficient of pitching moment
$C_N$	coefficient of normal force



$C_{N_{\delta_{pv}}}$	coefficient of normal force due to pitch vane deflection, $\text{deg}^{-1}$
$C_n$	coefficient of yawing moment
$C_{n_p}$	coefficient of yawing moment due to roll rate, $\text{rad}^{-1}$
$C_{n_r}$	coefficient of yawing moment due to yaw rate, $\text{rad}^{-1}$
$C_{n_0}$	yawing moment bias
$C_{n_{\beta}}$	coefficient of yawing moment due to angle of sideslip, $\text{deg}^{-1}$
$C_{n_{\delta_a}}$	coefficient of yawing moment due to aileron deflection, $\text{deg}^{-1}$
$C_{n_{\delta_{dh}}}$	coefficient of yawing moment due to differential horizontal stabilator deflection, $\text{deg}^{-1}$
$C_{n_{\delta_L}}$	coefficient of yawing moment due to equivalent lateral control deflection, $\text{deg}^{-1}$
$C_{n_{\delta_{pv}}}$	coefficient of yawing moment due to pitch vane deflection, $\text{ft/deg}$
$C_{n_{\delta_r}}$	coefficient of yawing moment due to rudder deflection, $\text{deg}^{-1}$
$C_{n_{\delta_{yv}}}$	coefficient of yawing moment due to yaw vane deflection, $\text{ft/deg}$
$C_Y$	coefficient of lateral force
$C_{Y_p}$	coefficient of lateral force due to roll rate, $\text{rad}^{-1}$
$C_{Y_r}$	coefficient of lateral force due to yaw rate, $\text{rad}^{-1}$
$C_{Y_0}$	lateral force bias
$C_{Y_{\beta}}$	coefficient of lateral force due to angle of sideslip, $\text{deg}^{-1}$
$C_{Y_{\delta_a}}$	coefficient of lateral force due to aileron deflection, $\text{deg}^{-1}$
$C_{Y_{\delta_{dh}}}$	coefficient of lateral force due to differential horizontal stabilator deflection, $\text{deg}^{-1}$
$C_{Y_{\delta_L}}$	coefficient of lateral force due to equivalent lateral control deflection, $\text{deg}^{-1}$
$C_{Y_{\delta_{pv}}}$	coefficient of lateral force due to pitch vane deflection, $\text{deg}^{-1}$
$C_{Y_{\delta_r}}$	coefficient of lateral force due to rudder deflection, $\text{deg}^{-1}$
$C_{Y_{\delta_{yv}}}$	coefficient of lateral force due to yaw vane deflection, $\text{deg}^{-1}$
$f$	system state function
$f_{\dot{p}}$	state noise coefficient for $\dot{p}$

$f_{\dot{r}}$	state noise coefficient for $\dot{r}$
$f_{\dot{\beta}}$	state noise coefficient for $\dot{\beta}$
$g$	gravitational force, 32.2 ft/sec <sup>2</sup>
$g$	system observation function
$\mathbf{GG}^*$	measurement noise covariance matrix
$\mathbf{H}$	approximation to the information matrix
$i$	general index
$I_x, I_y, I_z$	moments of inertia, slug-ft <sup>2</sup>
$I_{xy}, I_{xz}, I_{yz}$	cross products of inertia, slug-ft <sup>2</sup>
$J$	cost function
$L$	iteration number
$m$	aircraft mass, slug
$\mathbf{n}$	state noise vector
$n_{\dot{p}}$	state noise vector for $\dot{p}$
$n_{\dot{r}}$	state noise vector for $\dot{r}$
$n_{\dot{\beta}}$	state noise vector for $\dot{\beta}$
$N$	number of time points
$p$	roll rate, deg/sec
$\dot{p}$	roll acceleration, deg/sec <sup>2</sup>
$q$	pitch rate, deg/sec
$\dot{q}$	pitch acceleration, deg/sec <sup>2</sup>
$\bar{q}$	dynamic pressure, lbf/ft <sup>2</sup>
$r$	yaw rate, deg/sec
$\dot{r}$	yaw acceleration, deg/sec <sup>2</sup>
$\mathbf{R}$	innovation covariance matrix
$s$	reference area, ft <sup>2</sup>

$t$	time, sec
$t_0$	initial time
$T$	computed total engine thrust, lbf
$T_R$	computed right engine thrust, lbf
$T_L$	computed left engine thrust, lbf
$\mathbf{u}$	known control input vector
$V$	aircraft velocity, ft/sec
$\dot{V}$	rate of change of aircraft velocity, ft/sec <sup>2</sup>
$V_1$	left engine upper vane position, deg
$V_2$	left engine outer (or outboard) vane position, deg
$V_3$	left engine inner (or inboard) vane position, deg
$V_4$	right engine upper vane position, deg
$V_5$	right engine outer (or outboard) vane position, deg
$V_6$	right engine inner (or inboard) vane position, deg
$\mathbf{x}$	state vector
$\mathbf{x}_0$	state vector at initial time
$\dot{\mathbf{x}}$	time derivative of state vector
$\mathbf{z}$	observation vector
$\tilde{\mathbf{z}}_\xi$	predicted Kalman filter estimate
$\alpha$	angle of attack, deg
$\dot{\alpha}$	rate of change of angle of attack, deg/sec
$\alpha_m$	measured value of $\alpha$ , deg
$\beta$	angle of sideslip, deg
$\dot{\beta}$	rate of change of angle of sideslip, deg/sec
$\Delta$	difference
$\delta$	deflection

$\delta_a$	aileron deflection, deg
$\delta_{a_p}$	pilot aileron input, arc-in.
$\delta_{dh}$	differential horizontal tail (stabilator) deflection, deg
$\delta_L$	equivalent lateral control deflection (only applies to basic F-18 aircraft), deg
$\delta_{pv}$	equivalent pitch vane input (deflection $\times$ thrust), deg-lbf
$\delta_r$	rudder deflection, deg
$\delta_{r_p}$	pilot rudder input, in.
$\delta_{yv}$	equivalent yaw vane input (deflection $\times$ thrust), deg-lbf
$\eta$	measurement noise vector
$\theta$	pitch attitude, deg
$\dot{\theta}$	rate of change of pitch attitude, deg/sec
$\theta_m$	measured value of $\theta$ , deg
$\xi$	unknown parameter vector
$\hat{\xi}$	estimate of $\xi$
$\phi$	roll attitude, deg
$\dot{\phi}$	rate of change of roll attitude, deg/sec
$\phi_m$	measured value of $\phi$ , deg
$\dot{\psi}$	rate of change of heading attitude, deg/sec
$*$	transpose of a vector or matrix
$\nabla_{\xi}$	gradient with respect to $\xi$

## INTRODUCTION

High-angle-of-attack (high-AOA) technology for military aircraft has been an area of active research in recent years. Motivated by the tactical advantage of enhanced high-AOA agility and poststall maneuverability, aircraft designers and researchers from industry and government have moved beyond simply studying stall and spin characteristics and have been exploring the poststall region of the high-AOA flight envelope. Recent involvement by NASA in these efforts began in the mid-1980's with the establishment of the High Angle of Attack Technology Program (HATP), a multiyear program to

understand and explore aircraft flight at high AOA (refs. 1–3). Biannual conferences hosted by NASA between 1990 and 1996 were dedicated to the latest developments in high-AOA technology (refs. 4–6).

The two prime objectives of the HATP were to provide a flight-validated aircraft design methodology through experimental and computational methods that simulate and predict high-AOA aerodynamics, flight dynamics, and flying qualities and to improve aircraft agility at high AOA while expanding the usable high-AOA envelope. The development of these capabilities involved a close integration of ground-based and flight activity, including wind-tunnel tests (refs. 7–10), computational fluid dynamics (CFD) modeling (refs. 11–15), piloted simulations, advanced flight controls (refs. 16–20), and flight tests. This activity focused on three key areas: high-AOA aerodynamics, advanced high-AOA control concepts, and maneuver management. Access to full-scale flight conditions was deemed essential to address inherent shortcomings of subscale model and ground tests. In addition, flight validation would provide a more accurate evaluation of the emerging technologies, methods, and concepts being used than the subscale model and ground test.

The aircraft selected for the flight portion of the HATP was an F/A-18 airplane (McDonnell Douglas Corp., St. Louis, Missouri), subsequently named the High Angle of Attack Research Vehicle (HARV) (fig. 1). Previously used for high-AOA and spin research testing by the U. S. Navy at the Naval Air Test Center (Patuxent River, Maryland), the aircraft was last flown by the Navy in September 1982. Two years later, in October 1984, the aircraft was transferred to NASA and trucked to the NASA Dryden Flight Research Center (Edwards, California). In the fall of 1985, major efforts to reassemble the aircraft began, including removing unnecessary flight test wiring and installing a new research data system. On April 2, 1987, the first flight of the HARV (NASA tail number 840) was performed at NASA Dryden. On May 15, 1996, after flight number 388, testing was completed in accordance with the three-phase program schedule of the HATP. Reference 21 provides a more detailed overview of the HARV flight program and an accompanying reference list.

Phase I began in April 1987 and continued through 1989. During this period, the HARV flew 101 research missions, investigating high-AOA aerodynamics and handling characteristics to a maximum of  $55^\circ$  AOA. Phase I examined developmental issues of the HARV research instrumentation suite and established initial aerodynamic correlations between predictions and in-flight measurements (refs. 22–26). Particular attention was given to the burst location of strong vortices that formed off the wing-body strake (leading-edge extension (LEX)) at high AOA and the role of the vortices in inducing tail buffet (refs. 27–31). Parameter identification (PID) was also performed on the HARV during Phase I to initially assess stability and control derivatives obtained from wind-tunnel tests and early flight tests by the manufacturer and U. S. Navy (refs. 32–34).

Phase II involved major hardware and software modifications to the HARV: a multiaxis thrust-vectoring control system (TVCS) consisting of externally-mounted nozzle postexit vanes, and a specialized research flight control system (RFCS). The TVCS and RFCS are described in detail in the next section. The design was intended for research purposes only and not for production. This second phase, spanning from mid-1991 to late 1994, further expanded the HARV flight envelope. Demonstrated capabilities included stabilized flight at  $70^\circ$  AOA and rolling at high rates at  $65^\circ$  AOA.

Phase III flight activities, begun in 1995 and completed in May 1996, investigated advanced aerodynamic control concepts. These tests focused on the implementation of actuated forebody strakes conformally mounted on the nose of the HARV to enhance lateral-directional control at high AOA (refs. 35, 36).

A continuing objective of the flight program was the study of stability and control characteristics of the HARV during thrust-vectoring flight, particularly in the low-speed, high- $\text{AOA}$  regime. This paper presents flight-determined, subsonic, lateral-directional stability and control derivatives of the HARV extracted from dynamic flight data between  $10^\circ$  and  $70^\circ$   $\text{AOA}$  in increments of  $10^\circ$   $\text{AOA}$ . (A companion paper, reference 37, presents flight-determined, subsonic, longitudinal stability and control derivatives of the HARV.) The 26 flight maneuvers analyzed herein were performed during flights 155, 226, 248, 250, and 274, which occurred between 1992 and 1994. Subsonic Mach numbers varied from 0.52 for the low- $\text{AOA}$  maneuvers to 0.23 for the high- $\text{AOA}$  maneuvers.

The maneuvers were implemented by a control system feature providing preprogrammed single-surface inputs (SSIs) of aerodynamic controls and independent thrust-vectoring controls. Each input, known as a doublet, approximates a single cycle of a square wave. The control system feature effectively eliminated correlations and near-linear dependency problems between combinations of control and state variables introduced by the basic F-18 control augmentation system. The derivatives were extracted with a NASA Dryden-developed PID technique using a maximum likelihood estimator that accounts for both state and measurement noise in the linearized aircraft equations of motion. State noise was used to model the uncommanded forcing functions caused by separated and vortical flows over the aircraft, particularly at high  $\text{AOA}$ . Aerodynamic coefficients in the equations of motion were modified to account for the effects of thrust vectoring. The resulting derivative estimates are plotted as functions of  $\text{AOA}$  between  $10^\circ$  and  $70^\circ$ , and are discussed in relation to flight-determined derivatives of the basic F-18 aircraft and to predicted values obtained from thrust-vectoring ground tests and a simulation primarily based on wind-tunnel data of the basic F-18 aircraft. The effects of configuration differences and maneuver input quality are also considered in the comparisons. The HARV stability and control derivatives estimated from flight data in this paper are  $C_{l_\beta}$ ,  $C_{l_p}$ ,  $C_{l_r}$ ,  $C_{l_{\delta_a}}$ ,  $C_{l_{\delta_{dh}}}$ ,  $C_{l_{\delta_r}}$ ,  $C_{l_{\delta_{yv}}}$ ,  $C_{l_0}$ ,  $C_{n_\beta}$ ,  $C_{n_p}$ ,  $C_{n_r}$ ,  $C_{n_{\delta_a}}$ ,  $C_{n_{\delta_{dh}}}$ ,  $C_{n_{\delta_r}}$ ,  $C_{n_{\delta_{yv}}}$ ,  $C_{n_0}$ ,  $C_{Y_\beta}$ ,  $C_{Y_{\delta_a}}$ ,  $C_{Y_{\delta_{dh}}}$ ,  $C_{Y_{\delta_r}}$ ,  $C_{Y_{\delta_{yv}}}$ , and  $C_{Y_0}$ .

## VEHICLE DESCRIPTION

Many details about the vehicle described in this section were previously published (ref. 17, 38–40). These documents provide a more complete treatment of this and related topics. The following sections describe the hardware configuration, TVCS, software configuration, control laws, and thrust-vectoring mixer of the HARV.

### Hardware Configuration

The aircraft test bed was the sixth full-scale developmental F-18 airplane, a single-place, twin-engine, fighter-attack aircraft built for the U. S. Navy by McDonnell Douglas Corporation (St. Louis, Missouri) and Northrop Corporation (Los Angeles, California). The U. S. Navy previously used this particular aircraft (serial number 160780) for high- $\text{AOA}$  and spin testing. The F-18 HARV is powered by two General Electric (Lynn, Massachusetts) F404-GE-400 afterburning engines, rated at approximately 16,000-lbf static thrust at sea level. The aircraft features a midwing configuration with a wing-body strake, or wing-root LEX, that extends from the forward portion of the fuselage and blends into the wing. The configuration studied herein was used from 1992 to 1994 and included the LEX fence modification introduced in early 1989 to reduce vertical tail buffet caused by impingement of the LEX vortex; this configuration did not include the actuated forebody strakes used during Phase III. As flown, the HARV

carried no external stores and was highly instrumented for research purposes. The wingtip launching rails and missiles were replaced with specially designed airdata sensors and camera pods (described in the “Instrumentation and Data Acquisition” section). The in-flight refueling capability and tail arresting hook were retained. Figure 2 shows a three-view drawing of the HARV and its major physical characteristics.

The HARV has five pairs of conventional aerodynamic control surfaces: stabilators, rudders, ailerons, leading-edge flaps (LEFs), and trailing-edge flaps (TEFs). The twin vertical stabilizers, with trailing-edge rudders, are canted outboard at approximately  $20^\circ$  from the vertical. Conventional pitch control is provided by the collective deflection of the all-movable horizontal stabilators, symmetric LEFs, and symmetric TEFs. Roll control uses aileron deflection ( $\delta_a$ ), differential horizontal stabilator deflection ( $\delta_{dh}$ ), and asymmetric LEFs and TEFs. Directional control is provided by symmetric rudder deflection ( $\delta_r$ ) and a rudder-to-aileron interconnect. In addition, the flight control system (FCS) augments lateral-directional control with an aileron-to-rudder interconnect. Symmetric aileron droop and rudder toe-in are employed in the power approach configuration. A speed brake is located on the upper aft fuselage, between the vertical stabilizers. Table 1, reproduced from reference 38, lists maximum control surface position and rate limits, which are identical for both the HARV and basic F-18 aircraft.

Table 1. F-18 aerodynamic control surface position and rate limits.

Surface	Position limit, deg	Rate limit, deg/sec
Stabilator		
Trailing edge up	24.0	40
Trailing edge down	10.5	40
Aileron		
Trailing edge up	24.0	100
Trailing edge down	45.0	100
Rudder		
Trailing edge left	30.0	82
Trailing edge right	30.0	82
Trailing-edge flap (TEF):		
Up	8.0	18
Down	45.0	18
Leading-edge flap (LEF):		
Up	3.0	15
Down	33.0	15
Speed brake:		
Trailing edge up	60.0	20–30

## Thrust-Vectoring Control System

The addition of a TVCS required significant hardware and software modifications to the aircraft. As figure 3 shows, externally-mounted nozzle postexit vanes were added to vector engine thrust and provide additional pitching and yawing moments. The engines were modified to accommodate the thrust-vectoring vane installation by removing the divergent flap portion of the engine nozzle. Controlled deflection of the vanes (three for each engine) into the engine exhaust plume provides thrust-vectoring capability. The location and geometry of the thrust vanes (fig. 4) resulted from tradeoffs between thrust-vectoring performance and possible interference with aerodynamic surfaces and the vanes themselves. The larger top vanes generate a greater nosedown pitching moment, and the smaller inboard and outboard vanes used together generate sufficient noseup pitching moment. The upper vanes work in conjunction with either outboard or inboard vane to produce yawing moment. Details on the thrust-vane mixer controller, which coordinates the combined motions of both aerodynamic and thrust-vectoring controls, are provided in the “Thrust-Vectoring Mixer” section. Vane actuation is accomplished using modified aileron electrohydraulic actuators. Table 2 shows vane system specifications from reference 38.

Table 2. HARV thrust-vectoring vane system specifications.

Vane size, in.	
Upper	20 × 20
Inner and outer	20 × 15
Vane area, in <sup>2</sup> (ft <sup>2</sup> )	
Upper	358.76 (2.49)
Inner and outer	263.64 (1.83)
Vane position limit, deg	−10 to 25
Vane rate limit, deg/sec	80
TVCS total weight, lb	2200

To provide clearance for the outer vane actuator housing, the inside trailing edges of the stabilators were modified slightly. The area of a single unmodified stabilator is 44.13 ft<sup>2</sup>, and the area removed was 0.89 ft<sup>2</sup>. This minor area reduction did not significantly reduce stabilator effectiveness. An emergency spin-recovery parachute was installed on the upper aft portion of the fuselage between the two engines. The HARV also has an emergency hydraulic and electrical system in case of inadvertent loss of engine power. Engine control was modified to provide a pilot-selectable, turbine discharge–temperature bias control for additional engine stall margin at high AOA.

Table 3, from reference 21, compares the unmodified and modified F-18 HARV. The total weight difference of 4119 lb includes approximately 2200 lb for the TVCS itself; 1500 lb for the spin-recovery parachute, emergency systems, and ballast (located in the nosecone for pitch balance); and 419 lb for equipment and wiring not directly associated with the TVCS. The final TVCS design does not represent a production prototype, but is strictly an experimental installation for research evaluation of the thrust-vectoring control concept.



Table 3. Comparison of unmodified and modified F-18 HARV.

Parameter	Unmodified* (Phase I)	Modified* (Phases II and III)
Weight, lb	31,980	36,099
Reference wing area, ft <sup>2</sup>	400	400
Reference MAC, ft	11.52	11.52
Reference span, ft	37.4	37.4
Center of gravity		
Percent MAC	21.9	23.8
Fuselage reference station, in.	454.33	456.88
Waterline, in.	105.24	105.35
Roll inertia, slug-ft <sup>2</sup>	22,040	22,789
Pitch inertia, slug-ft <sup>2</sup>	124,554	176,809
Yaw inertia, slug-ft <sup>2</sup>	139,382	191,744
Product of inertia, slug-ft <sup>2</sup>	-2,039	-2,305
Overall length, ft	56	56
Wing aspect ratio	3.5	3.5
Stabilator span, ft	21.6	21.6
Stabilator area (total of both), ft <sup>2</sup>	88.26	86.48

\*In each case, the fuel weight is 6480 lb, which represents an approximately 60-percent fuel condition. The landing gear is up; the configuration is clean; and pilot and support equipment are included in the weight.

## Software Configuration

The TVCS hardware modifications required corresponding software modifications to the FCS and mission computer (MC) (refs. 17, 39). The FCS for the basic F-18 airplane consists of quadruply-redundant 701E (General Electric, Lynn, Massachusetts) flight control computers (FCCs) running the standard F/A-18 V10.1 flight control law, which is a digitally mechanized fly-by-wire control augmentation system. The basic FCS was modified for the HARV by adding an analog interface to the thrust-vectoring vane actuators and an RFCS programmed in Ada (ref. 40). The analog input card and RFCS were installed in spare card slots in the basic 701E FCC. The basic FCC maintains overall and primary control of the aircraft, controls input/output processing functions, communicates with the MC for outer-loop control, and displays information through a military standard 1553 data bus.

The RFCS was added to provide a flexible platform for control law research. The RFCS central processing unit is a PACE (Performance Semiconductor Corp., Sunnyvale, California) military standard 1750A architecture processor slaved to the primary 701E computer. With the RFCS engaged, the 701E computer selects the RFCS actuator commands computed by the 1750A computer rather than the HARV V10.1 control law. Dual-port random access memory (DPRAM) provides the communication link between the 701E and 1750A computers. The RFCS contains 32,000 words of electrically erasable programmable read-only memory, 16,000 words of ultraviolet programmable read-only memory, 2,000 words of random-access memory, and 2,000 words of DPRAM. All RFCS command inputs,

feedback inputs, monitor data, and actuator command outputs are communicated to the FCC through the DPRAM, such that the RFCS can be considered an embedded control system.

The aircraft is only under RFCS control during the up-and-away research phases of a HARV flight. The RFCS is armed by a cockpit toggle switch and engaged (or activated) by the existing nosewheel steering switch on the control stick. The RFCS is manually disengaged through the arm switch or a paddle switch on the control stick. Autodisengagement may occur if predefined limits on rates, accelerations, engine sensors, or airdata sensors are exceeded. The 701E FCC retains complete failure detection and fault management as well as appropriate mode switching in the event of certain failures. The basic F-18 V10.1 control laws and RFCS control laws run independently, in parallel, and are continuously computed throughout the flight envelope. The backup nature of this architecture allows the RFCS software to be classified as non-safety-of-flight. The basic control laws are used with the RFCS disengaged during normal flight, including takeoff and landing.

A useful and important research tool called the onboard excitation system (OBES) was also incorporated in the RFCS. Software in the OBES held preprogrammed research and envelope expansion maneuvers, which were used for flutter envelope clearance, control power research, and aerodynamic and control law PID. For aerodynamic PID, the OBES, when activated by the pilot, would command SSIs through the RFCS to particular control surfaces. By permitting single-surface aerodynamic control deflections, control surface correlation problems were eliminated from the PID analysis. Typically, the feedback and control augmentation systems of modern fighter aircraft introduce relatively high correlations (near-linear dependency) between combinations of the aircraft controls and states, complicating the identification of individual control surface effectiveness (ref. 41). Independent thrust-vectoring vane deflections were also available with the OBES; these deflections were not single-vane but rather single-axis deflections, using all vanes to excite responses in either the pitch or yaw axis.

## Controls Laws

The RFCS control laws were originally developed by McDonnell Aircraft Company (St. Louis, Missouri) with the goal of demonstrating the research utility of the TVCS and to allow flight envelope expansion of the RFCS software (ref. 17). The control laws were designed to provide stabilized flight and large amplitude maneuvering capability at high AOA. This capability was achieved through the integration of both aerodynamic and propulsive controls. Initial design emphasis was placed on the stabilized flight task. The RFCS control laws were designed with a modular approach and implemented in Ada. The RFCS software can be separated into longitudinal, lateral-directional, thrust-vane mixer, and gross-thrust estimation modules. The latter two modules are discussed in the next section.

The longitudinal control law is an AOA command system that uses pilot stick position, AOA, pitch rate ( $q$ ), and inertial coupling feedback (through the product of angular rates  $p$  and  $r$ ) as inputs. Inertial coupling feedbacks are used to counteract undesirable cross-axis motion generated at high angular rates. Both stabilator and pitch thrust vectoring are used for rapid commands, but steady-state vectoring is driven to zero deflection (washed out) if collective stabilator is not saturated. This scheme helps to minimize thrust loss caused by vectoring and reduces thermal loads on the vanes. Trimmed flight at greater than approximately  $55^\circ$  AOA requires a nonzero steady-state pitch thrust vectoring because of stabilator saturation. The control stick is geared to provide an AOA of  $70^\circ$  at 5 in. of aft stick deflection. The control system selects airdata-measured AOA at less than  $25^\circ$  AOA and selects inertial navigation system-computed AOA at greater than  $30^\circ$  AOA. The control system fades between the two AOA sources between  $25^\circ$  and  $30^\circ$  AOA.

The lateral-directional control laws use stability-axis roll and yaw rate, lateral acceleration, sideslip rate, and inertial coupling (the product of  $p$  and  $q$ , directional only) as feedback signals. Differential stabilator, aileron, differential TEFs, rudder, and yaw vectoring are used for stabilization, coordination, and maneuvering flight. Differential LEFs are not used. Differential stabilator command is limited as a function of AOA and by symmetric stabilator command to maintain pitch command priority. The lateral-directional control law provides a feet-on-the-floor stability-axis roll rate command capability; lateral stick commands stability-axis roll rate separately from rudder pedal inputs, which command sideslip angle. At the lowest AOA and highest subsonic Mach numbers, the RFCS uses lateral-directional commands from the basic F-18 control laws with the addition of some yaw thrust vectoring to augment rudder power. Whereas the longitudinal control laws were designed using a model-following technique, the lateral-directional controls used an eigenstructure-assignment technique.

As new software versions of the RFCS control law integrating the thrust-vectoring system became available, configuration control of the various versions was necessary. The original control law was designed by McDonnell Aircraft Company, as described earlier, and revisions to it included RFCS version sets 22, 24, 26, and 28. These early versions were used during most of Phase II and were collectively referred to as the NASA-0 RFCS control law. During the end of Phase II, the NASA Langley Research Center (Hampton, Virginia), with help from NASA Dryden, developed a control law called NASA-1A, which first flew successfully on flight 256 on June 3, 1994. The NASA-1A control law used a technique called variable-output feedback gain to design the longitudinal axis. An eigenstructure-assignment design procedure using control power, robustness, agility, and flying qualities tradeoffs was implemented in the lateral-directional axes in combination with a control power allocation technique called pseudocontrols. During Phase III, the addition of nose-mounted conformal strakes called Actuated Nose Strakes for Enhanced Rolling (ANSER) required a new control law to complement the NASA-1A thrust-vectoring control law. Reference 21 provides additional discussion of and references for these control system features.

When the RFCS is armed, the basic F-18 control system sets the turning vanes to a predetermined ready position (the  $0^\circ$  vane deflection position). The V10.1 control laws continue to control the aircraft until the pilot engages the RFCS, at which point the turning vanes move to the edge of the exhaust plume boundary (approximately  $8^\circ$ – $10^\circ$  vane deflection, depending on nozzle pressure ratio) and the RFCS control laws take over. The integrated coordination of the six thrust-vectoring vanes is performed by the RFCS function known as the “mixer.”

## **Thrust-Vectoring Mixer**

To interface the flight control laws with the thrust-vectoring vanes, a “mixer” was developed to translate the pitch and yaw thrust-vectoring commands from the RFCS into appropriate vane commands for distribution to the actuators. Although individually commanding the six thrust-vectoring vanes from within the inner-loop control laws (similar to aerodynamic surfaces) is possible, the mixer function was designed to accomplish the complex task of computing the proper thrust-vane deflections required to achieve the desired moments from a separate software module.

The mixer was developed by McDonnell Aircraft Company based upon the results of high-pressure cold-jet tests conducted at NASA Langley using a 14.25-percent-scale nozzle of the TVCS (refs. 42–45). Because the total moment achieved from thrust vectoring is a function of the vane deflection angle as well as the thrust level, the RFCS calculates pitch and yaw thrust-vectoring commands in terms of degrees of

vectored-thrust deflection on the basis of a reference gross thrust. The mixer then uses the results of a real-time thrust estimation algorithm to scale the RFCS-commanded thrust-vectoring moments to the thrust available and to adjust the vane angles to produce the desired control moments. In this way, the apparent thrust-vectoring effectiveness is independent of engine thrust (within the range of the vane position limits and accuracy of the thrust computation). Gross thrust for each engine is individually estimated from nozzle exit radius, engine pressure ratio, and power lever angle for the left or right engine (ref. 46). The mixer requires nozzle pressure ratio, estimated gross thrust, and nozzle exit radius from each engine, and the desired vectoring commands to produce the six thrust-vane actuator commands. Position, rate, and load limiting are also accounted for by the mixer. The theory and implementation of the mixer has been presented in an original corporate report (ref. 47). In addition to the NASA Langley 14.25-percent-scale cold-jet tests, reference 48 describes independent subscale laboratory tests to predict thrust-vectoring effectiveness.

Toward the end of Phase II of the HARV flight program, new versions of the mixer were studied. The original mixer was subsequently called mixer 1; however, only one of the several revisions, mixer 4.2, was carried through to flight. Mixer 4.2 was incorporated in the NASA-1A control law, which was first successfully flown during flight 256 on June 3, 1994. The development of mixer 4.2 was motivated because mixer 1 had no roll-vectoring capability (only pitch and yaw), nor did mixer 1 prioritize pitch and yaw vectoring when a combination of these commands could not be simultaneously achieved. The new mixer was developed with a numerical optimization technique based on thrust-vectoring effectiveness and thrust-loss data from ground tests and considerations of optimal vane placement of inactive vanes. The primary design requirement was to achieve the commanded thrust-vectoring moments with the smallest error practical while incorporating a pitch, yaw, and roll priority logic and meeting structural limitations. A complete description of the design methodology and optimization process used to develop the new mixer has previously been published (ref. 49).

The first four flights addressed in this paper (flights 155, 226, 248, and 250) were flown with the earlier NASA-0 and mixer 1 software and cover 25 of the 26 PID maneuvers studied herein. The remaining (26<sup>th</sup>) maneuver (at approximately 70° AOA) was performed on flight 274, and the NASA-1A and mixer 4.2 software versions were operating. At 70° AOA, however, differences in software versions did not affect the maneuver in any way and thus affected none of the results of this paper.

## **INSTRUMENTATION AND DATA ACQUISITION**

The MC controlled the 1553 multiplex data bus, which provided a standard interface for all equipment connected to the bus (such as monitoring instrumentation and recording systems). The MC also was the interface between the flight control sensors and computers to the pilot's digital display indicators. The indicators display system status, caution, and failure annunciation in addition to primary flight information. Selected flight information could also be presented on the pilot's head-up display.

Research instrumentation included three-axis linear accelerometers, attitude and angular-rate gyros, control surface position transducers, and redundant airdata sensors. Angle-of-attack information was available using production airdata sensors mounted on the forward fuselage, but only to a maximum of approximately 35° AOA because of sensor position limits. For this reason, AOA, AOA rate, angle of sideslip, and sideslip rate were computed in the MC using data from the inertial navigation system. In addition to inertially-derived airdata, two high-AOA airdata systems were developed. One system used

swiveling (self-aligning) pitot probes with conventional AOA and sideslip vanes mounted on both wingtips (ref. 50). A second system used a pneumatic flush airdata system consisting of several pressure sensors located around the tip of the HARV nose cone (ref. 51–53). Airdata from both systems were used for postflight data analysis. Additionally, airdata from the wingtip swivel probes were used for real-time cockpit display and control room monitoring. Airdata used in the present PID analysis were taken from the wingtip probes.

Many other parameters were measured to study high-AOA flight. Additional instrumentation included 75 thermocouples and 14 strain gages on the thrust-vectoring system for monitoring temperatures and loads. Nearly 400 static-pressure orifices were installed on the forebody and LEX to characterize the forebody pressure distribution (refs. 25 and 26). Off-surface flow visualization of the forebody and LEX vortices were obtained using a smoke generation system that emits particles at the nosetip and LEX apex (refs. 27 and 54). Four video cameras and one still camera were used to photograph the flow. Surface flow visualization was examined using conventional tufts as well as an emitted fluid technique (ref. 23). Flow visualization and pressure data were used to correlate with and validate external-flow CFD simulations (refs. 11–15) and full-scale wind-tunnel predictions (refs. 7, 8).

Both engines were instrumented to monitor engine operation and were equipped with a real-time thrust-measurement system (ref. 46). The right engine had additional instrumentation for engine and inlet diagnostics with 63 pressure sensors located along the inlet lip and down the duct to measure inlet distortion at high AOA. An inlet rake complex with 40 high-response pressure sensors was also installed just forward of the right engine compressor face to study compressor stalls during high-AOA dynamic flight (ref. 55). Data from the inlet sensors and inlet rake complex were also used to validate internal-flow CFD simulations of the F-18 HARV inlet (refs. 56 and 57).

Data measurements and video signals were telemetered to ground stations for real-time monitoring in the control room and recorded for postflight analysis. The telemetry system consisted of two independent, asynchronous pulse code modulation (PCM) data encoders, each with a basic PCM word size of 10 bits. All outputs of the encoders were sent by telemetry to the ground because no onboard recording of PCM data was available. Special provisions were incorporated in the data acquisition system for high-resolution signals of certain types of data. As many as 2000 parameters could be telemetered on the two PCM telemetry streams, with data rates as high as 2142 Hz on select signals.

Flight data used in the present PID analysis were acquired from ground-recorded data and thinned to a final sample rate of 40 Hz. Measurements of AOA and sideslip were corrected for center-of-gravity (CG) offset. Corrections for upwash, sidewash, and boom-bending effects were also made for boom-obtained airdata. Linear accelerometer data were corrected in the PID program for instrument offsets from the CG. Transducers were also available for measuring engine operation and fuel consumption, from which instantaneous mass and inertia characteristics could be calculated. Furthermore, before the maneuvers were analyzed, the data were corrected for time lags introduced by sensor dynamics and signal filtering. Making these corrections was critical to adequately estimate stability and control derivatives (ref. 41).

## **METHODS OF ANALYSIS**

The formulation of the PID method is described in this section. The associated equations of motion used in the method are also presented.

## Parameter Identification Formulation

A primary purpose of the HARV flight program was to evaluate the aircraft configuration during high-AOA flight. When flying at high AOA, significant flow separation and vortical flow over the aircraft cause the vehicle to exhibit uncommanded responses. A discussion of maneuver difficulties and related analysis issues under these conditions for the 3/8-scale F-15 Remotely Piloted Research Vehicle at AOAs from  $-20^\circ$  to  $53^\circ$  has previously been published (ref. 58). At high AOA, the uncommanded motions vary from relatively small amplitude, high-frequency disturbances to very large wing rocking motions or complete rolloff from the flight condition. In addition to being bothersome to the pilot, the motions also complicate the extraction of stability and control derivatives from the planned stability and control maneuvers (ref. 58). The OBES aided the present analysis by augmenting the RFCS control laws and allowing for SSIs. To better analyze the existing maneuvers, accounting for the uncommanded portions of the aircraft motion was necessary.

The procedure implemented in this analysis used state noise to model the uncommanded forcing functions. This technique has previously been described in detail (refs. 59–61). The technique applied to the HARV data also required that the normal aircraft equations of motion be linear in the aerodynamic coefficients; this requirement presented no particular difficulty because the normal stability and control derivatives were already locally linear approximations of nonlinear aircraft aerodynamics.

To perform the analysis presented in this report, an existing parameter estimation computer program was modified to reflect the additional complexity required to include the effects of the state noise (inputs caused by separated and vortical flows) on the stability and control maneuvers. A brief description of the state noise algorithm follows.

A precise, mathematically probabilistic statement of the parameter estimation problem is possible. The first step is to define the general system model (aircraft equations of motion). This model can be written in the continuous/discrete form as follows:

$$\mathbf{x}(t_0) = \mathbf{x}_0 \quad (1)$$

$$\dot{\mathbf{x}}(t) = f[\mathbf{x}(t), \mathbf{u}(t), \boldsymbol{\xi}] + \mathbf{F}(\boldsymbol{\xi})\mathbf{n}(t) \quad (2)$$

$$\mathbf{z}(t_i) = g[\mathbf{x}(t_i), \mathbf{u}(t_i), \boldsymbol{\xi}] + \mathbf{G}(\boldsymbol{\xi})\boldsymbol{\eta}_i \quad (3)$$

where  $\mathbf{x}$  is the state vector,  $\mathbf{z}$  is the observation vector,  $f$  and  $g$  are system state and observation functions,  $\mathbf{u}$  is the known control input vector,  $\boldsymbol{\xi}$  is the unknown parameter vector,  $\mathbf{n}$  is the state noise vector,  $\boldsymbol{\eta}$  is the measurement noise vector,  $\mathbf{F}$  and  $\mathbf{G}$  are system matrices, and  $t$  is time. The state noise vector is assumed to be zero-mean, white, Gaussian, and stationary; and the measurement noise vector is assumed to be a sequence of independent Gaussian random variables with zero-mean and identity covariance. For each possible estimate of the unknown parameters, a probability that the aircraft response time histories attain values near the observed values can then be defined. The maximum likelihood estimates are defined as those estimates that maximize this probability. Maximum likelihood estimation has many desirable statistical characteristics; for example, the estimator yields asymptotically unbiased, consistent, and efficient estimates.

If equations (2) and (3) are linearized (as is the case for the stability and control derivatives in the aircraft problem), then

$$\mathbf{x}(t_0) = \mathbf{x}_0 \quad (4)$$

$$\dot{\mathbf{x}}(t) = \mathbf{A}\mathbf{x}(t) + \mathbf{B}\mathbf{u}(t) + \mathbf{F}\mathbf{n}(t) \quad (5)$$

$$\mathbf{z}(t_i) = \mathbf{C}\mathbf{x}(t_i) + \mathbf{D}\mathbf{u}(t_i) + \mathbf{G}\eta_i \quad (6)$$

where  $\mathbf{A}$ ,  $\mathbf{B}$ ,  $\mathbf{C}$ , and  $\mathbf{D}$  are system matrices.

When state noise is important, the nonlinear forms of equations (1) to (3) are intractable. For the linear model defined by equations (4) to (6), the cost function that accounts for state noise (that is, a function of the difference between the measured and computed time histories) is as follows:

$$J(\xi) = \frac{1}{2} \sum_{i=1}^N [\mathbf{z}(t_i) - \tilde{\mathbf{z}}_{\xi}(t_i)]^* \mathbf{R}^{-1} [\mathbf{z}(t_i) - \tilde{\mathbf{z}}_{\xi}(t_i)] + \frac{1}{2} N \ln |\mathbf{R}| \quad (7)$$

where  $\mathbf{R}$  is the innovation covariance matrix and  $N$  is the number of time points. The  $\mathbf{z}_{\xi}(t_i)$  term in equation (7) is the Kalman-filtered estimate of  $\mathbf{z}$ .

To minimize the cost function  $J(\xi)$ , the Newton-Raphson algorithm can be applied, which chooses successive estimates of the vector of unknown coefficients,  $\hat{\xi}$ . Let  $L$  be the iteration number. The  $L + 1$  estimate of  $\hat{\xi}$  is then obtained from the  $L$  estimate as follows:

$$\hat{\xi}_{L+1} = \hat{\xi}_L - [\nabla_{\xi}^2 J(\hat{\xi}_L)]^{-1} [\nabla_{\xi}^* J(\hat{\xi}_L)] \quad (8)$$

If  $\mathbf{R}$  is assumed fixed, the first and second gradients are defined as follows:

$$\nabla_{\xi} J(\xi) = - \sum_{i=1}^N [\mathbf{z}(t_i) - \tilde{\mathbf{z}}_{\xi}(t_i)]^* (\mathbf{G}\mathbf{G}^*)^{-1} [\nabla_{\xi} \tilde{\mathbf{z}}_{\xi}(t_i)] \quad (9)$$

$$\begin{aligned} \nabla_{\xi}^2 J(\xi) = & \sum_{i=1}^N [\nabla_{\xi} \tilde{\mathbf{z}}_{\xi}(t_i)]^* (\mathbf{G}\mathbf{G}^*)^{-1} [\nabla_{\xi} \tilde{\mathbf{z}}_{\xi}(t_i)] \\ & - \sum_{i=1}^N [\mathbf{z}(t_i) - \tilde{\mathbf{z}}_{\xi}(t_i)]^* (\mathbf{G}\mathbf{G}^*)^{-1} [\nabla_{\xi}^2 \tilde{\mathbf{z}}_{\xi}(t_i)] \end{aligned} \quad (10)$$

where  $\mathbf{G}\mathbf{G}^*$  is the measurement noise covariance matrix. The Gauss-Newton approximation to the second gradient is as follows:

$$\nabla_{\xi}^2 J(\xi) \cong \sum_{i=1}^N [\nabla_{\xi} \tilde{\mathbf{z}}_{\xi}(t_i)]^* (\mathbf{G}\mathbf{G}^*)^{-1} [\nabla_{\xi} \tilde{\mathbf{z}}_{\xi}(t_i)] \quad (11)$$

The Gauss-Newton approximation, which in past reports by the first author was sometimes referred to as modified Newton-Raphson, is computationally much easier than the Newton-Raphson approximation because the second gradient of the innovation never needs to be calculated.

Figure 5 shows the maximum likelihood estimation concept. The measured response is compared with the estimated response, and the difference between these responses is called the response error. The cost function of equation (7) includes this response error. The minimization algorithm is used to find the coefficient values that minimize the cost function. Each iteration of this algorithm provides a new estimate of the unknown coefficients on the basis of the response error. These new estimates are then used to update values of the coefficients of the mathematical model, providing a new estimated response and, therefore, a new response error. Updating of the mathematical model continues iteratively until a convergence criterion is satisfied (that is, when the ratio of the change in total cost to the total cost,  $\Delta J(\xi)/J(\xi)$ , is less than 0.000001). The estimates resulting from this procedure are the maximum likelihood estimates.

The maximum likelihood estimator also provides a measure of the reliability of each estimate based on the information obtained from each dynamic maneuver. This measure of the reliability, analogous to the standard deviation, is called the Cramér-Rao bound (refs. 60, 62). The Cramér-Rao bound, as computed by current programs, should generally be used as a measure of relative, rather than absolute, accuracy. The bound is obtained from the approximation to the information matrix,  $\mathbf{H}$ , which is based on equation (11); the actual information matrix is defined when evaluated at the correct values (not the maximum likelihood estimates) of all the coefficients. The bound for each unknown coefficient is the square root of the corresponding diagonal element of  $\mathbf{H}^{-1}$ ; that is, for the  $i^{\text{th}}$  unknown, the Cramér-Rao bound is  $\sqrt{(\mathbf{H}^{-1})_{i,i}}$ . The stability and control derivatives presented in the “Results and Discussion” section were analyzed assuming that state noise was present in all maneuver cases.

## Equations of Motion

The linearized aircraft equations of motion used in the PID analysis are derived from a general system of nine coupled, nonlinear differential equations that describe the aircraft motion (refs. 63, 64). These nonlinear equations assume a rigid vehicle and a flat, nonrotating Earth. The time rate of change of mass and inertia is assumed negligible, and fuel-sloshing effects are ignored. No small angle approximations are used, but the absolute values of angle of sideslip,  $\beta$ , and pitch attitude,  $\theta$ , must be less than  $90^\circ$  because of singularities at  $\pm 90^\circ$ . The aircraft velocity must not be 0. No symmetry assumptions are made. Engine thrust terms are included, assuming the engine alignment and thrust vector are along the X axis. (Terms accounting for thrust vectoring are included in the expressions for the aerodynamic coefficients, to be described later). The equations are written in body axes referenced to the CG. All angles are in degrees. The  $\dot{V}$  and  $\dot{\psi}$  equations are not relevant to the present analysis and therefore are not included. The remaining system of state equations is as follows:

$$\begin{aligned} \dot{\alpha} = & q - \tan \beta (p \cos \alpha + r \sin \alpha) - \left[ \bar{q} s / (m V \cos \beta) \right] (C_N \cos \alpha - C_A \sin \alpha) \\ & + \left[ g / (V \cos \beta) \right] \left\{ \cos \theta \cos \phi \cos \alpha + \sin \theta \sin \alpha - \left[ T / (mg) \right] \sin \alpha \right\} \end{aligned} \quad (12)$$



$$\begin{aligned}\dot{\beta} = & p \sin \alpha - r \cos \alpha + \cos \beta \left[ (\bar{q}s)C_Y/(mV) + (g/V)\cos \theta \sin \phi \right] \\ & + \sin \beta \left\{ \left[ \bar{q}s(C_N \sin \alpha + C_A \cos \alpha) \right]/(mV) \right. \\ & \left. - (g/V) \left[ \cos \theta \cos \phi \sin \alpha - \sin \theta \cos \alpha - (T/(mg)) \cos \alpha \right] \right\}\end{aligned}\quad (13)$$

$$\dot{p}I_x - \dot{q}I_{xy} - \dot{r}I_{xz} = \bar{q}s b C_l + qr(I_y - I_z) + (q^2 - r^2)I_{yz} + pqI_{xz} - rpI_{xy} \quad (14)$$

$$\dot{q}I_y - \dot{r}I_{yz} - \dot{p}I_{xy} = \bar{q}s c C_m + rp(I_z - I_x) + (r^2 - p^2)I_{xz} + qrI_{xy} - pqI_{yz} \quad (15)$$

$$\dot{r}I_z - \dot{p}I_{xz} - \dot{q}I_{yz} = \bar{q}s b C_n + pq(I_x - I_y) + (p^2 - q^2)I_{xy} + prI_{yz} - qrI_{xz} \quad (16)$$

$$\dot{\theta} = q \cos \phi - r \sin \phi \quad (17)$$

$$\dot{\phi} = p + r \cos \phi \tan \theta + q \sin \phi \tan \theta \quad (18)$$

Most aircraft, including the HARV examined here, are symmetric about the x-z plane. This symmetry can be used with small-angle approximations to separate the equations of motion into two largely independent sets describing the longitudinal and lateral-directional motions of the aircraft. Certain nonlinear terms are linearized through the use of measured data. A comprehensive treatment of the aircraft PID linearization problem is given in references 63 and 65.

Symmetry and small perturbation approximations allow the lateral-directional equations of motion (eqs. 13, 14, 16, and 18) to be expressed in forms that contain locally linear approximations in the aerodynamic coefficients as required by equation 5 (repeated here):

$$\dot{\mathbf{x}}(t) = \mathbf{A}\mathbf{x}(t) + \mathbf{B}\mathbf{u}(t) + \mathbf{F}\mathbf{n}(t)$$

The aerodynamic terms of interest in equations 13, 14, and 16 are  $C_Y$ ,  $C_l$ , and  $C_n$ , the coefficients of lateral force, rolling moment, and yawing moment, respectively. The coefficients  $C_Y$ ,  $C_l$ , and  $C_n$  are expanded as follows:

$$\begin{aligned}C_Y = & C_{Y_\beta} \beta + (C_{Y_p} p + C_{Y_r} r) b / (2V) + C_{Y_{\delta_a}} \delta_a + C_{Y_{\delta_r}} \delta_r + C_{Y_{\delta_{dh}}} \delta_{dh} + C_{Y_0} \\ & + C_{Y_{\delta_{pv}}} \delta_{pv} / (\bar{q}s) + C_{Y_{\delta_{yv}}} \delta_{yv} / (\bar{q}s)\end{aligned}\quad (19)$$

$$\begin{aligned}C_l = & C_{l_\beta} \beta + (C_{l_p} p + C_{l_r} r) b / (2V) + C_{l_{\delta_a}} \delta_a + C_{l_{\delta_r}} \delta_r + C_{l_{\delta_{dh}}} \delta_{dh} + C_{l_0} \\ & + C_{l_{\delta_{pv}}} \delta_{pv} / (\bar{q}s b) + C_{l_{\delta_{yv}}} \delta_{yv} / (\bar{q}s b)\end{aligned}\quad (20)$$

$$C_n = C_{n_\beta} \beta + (C_{n_p} p + C_{n_r} r) b / (2V) + C_{n_{\delta_a}} \delta_a + C_{n_{\delta_r}} \delta_r + C_{n_{\delta_{dh}}} \delta_{dh} + C_{n_0} \\ + C_{n_{\delta_{pv}}} \delta_{pv} / (\bar{q} s b) + C_{n_{\delta_{yv}}} \delta_{yv} / (\bar{q} s b) \quad (21)$$

The unknown stability and control derivatives to be estimated by PID are  $C_{Y_\beta}$ ,  $C_{Y_{\delta_a}}$ ,  $C_{Y_{\delta_{dh}}}$ ,  $C_{Y_{\delta_r}}$ ,  $C_{Y_{\delta_{yv}}}$ ,  $C_{Y_0}$ ,  $C_{l_\beta}$ ,  $C_{l_p}$ ,  $C_{l_r}$ ,  $C_{l_{\delta_a}}$ ,  $C_{l_{\delta_{dh}}}$ ,  $C_{l_{\delta_r}}$ ,  $C_{l_{\delta_{yv}}}$ ,  $C_{l_0}$ ,  $C_{n_\beta}$ ,  $C_{n_p}$ ,  $C_{n_r}$ ,  $C_{n_{\delta_a}}$ ,  $C_{n_{\delta_{dh}}}$ ,  $C_{n_{\delta_r}}$ ,  $C_{n_{\delta_{yv}}}$ , and  $C_{n_0}$ . The  $C_{Y_{\delta_{pv}}}$ ,  $C_{l_{\delta_{pv}}}$ , and  $C_{n_{\delta_{pv}}}$  derivatives were not estimated because those derivatives did not significantly affect the analysis. For the HARV,  $C_{Y_p}$  and  $C_{Y_r}$  were found to be small and are not estimated. Note that  $C_{Y_{\delta_{yv}}}$ ,  $C_{l_{\delta_{yv}}}$ , and  $C_{n_{\delta_{yv}}}$  are the coefficients resulting from yaw vane inputs. The stability and control derivatives are related to equation 5 through the following expressions for system matrices **A**, **B**, and **F** with corresponding state, control, and noise vectors **x**, **u**, and **n**:

$$\mathbf{A} = \begin{bmatrix} C_{Y_\beta} [\bar{q} s / (mV)] & \sin \alpha_m & -\cos \alpha_m & (g/V) \cos \theta_m \sin \phi_m \\ C_{l_\beta} (\bar{q} s b / I_x) & C_{l_p} (\bar{q} s b / I_x) [b / (2V)] & C_{l_r} (\bar{q} s b / I_x) [b / (2V)] & 0 \\ C_{n_\beta} (\bar{q} s b / I_z) & C_{n_p} (\bar{q} s b / I_z) [b / (2V)] & C_{n_r} (\bar{q} s b / I_z) [b / (2V)] & 0 \\ 0 & 1 & \tan \theta_m \cos \phi_m & 0 \end{bmatrix} \quad (22)$$

$$\mathbf{B} = \begin{bmatrix} C_{Y_{\delta_a}} [\bar{q} s / (mV)] & C_{Y_{\delta_{dh}}} [\bar{q} s / (mV)] & C_{Y_{\delta_r}} [\bar{q} s / (mV)] & C_{Y_{\delta_{yv}}} [1 / (mV)] & C_{Y_0} [\bar{q} s / (mV)] \\ C_{l_{\delta_a}} (\bar{q} s b / I_x) & C_{l_{\delta_{dh}}} (\bar{q} s b / I_x) & C_{l_{\delta_r}} (\bar{q} s b / I_x) & C_{l_{\delta_{yv}}} (1 / I_x) & C_{l_0} (\bar{q} s b / I_x) \\ C_{n_{\delta_a}} (\bar{q} s b / I_z) & C_{n_{\delta_{dh}}} (\bar{q} s b / I_z) & C_{n_{\delta_r}} (\bar{q} s b / I_z) & C_{n_{\delta_{yv}}} (1 / I_z) & C_{n_0} (\bar{q} s b / I_z) \\ 0 & 0 & 0 & 0 & 0 \end{bmatrix} \quad (23)$$

$$\mathbf{F} = \begin{bmatrix} f_{\dot{\beta}} & 0 & 0 \\ 0 & f_{\dot{p}} & 0 \\ 0 & 0 & f_{\dot{r}} \\ 0 & 0 & 0 \end{bmatrix} \quad (24)$$

$$\mathbf{x} = [\beta \quad p \quad r \quad \phi]^* \quad (25)$$

$$\mathbf{u} = [\delta_a \quad \delta_{dh} \quad \delta_r \quad \delta_{yv} \quad 1]^* \quad (26)$$

$$\mathbf{n} = [n_{\dot{\beta}} \quad n_{\dot{p}} \quad n_{\dot{r}}]^* \quad (27)$$

where  $\alpha_m$ ,  $\theta_m$ , and  $\phi_m$  are the measured values of  $\alpha$ ,  $\theta$ , and  $\phi$ . The state noise coefficients are  $f_{\dot{\beta}}$ ,  $f_{\dot{p}}$ , and  $f_{\dot{r}}$ , and the state noise is defined as  $n_{\dot{\beta}}$ ,  $n_{\dot{p}}$ , and  $n_{\dot{r}}$ .

## RESULTS AND DISCUSSION

The 26 stability and control maneuvers examined herein were all analyzed with the PID technique described in the previous section. All maneuvers were subsonic (from Mach 0.23 to 0.52) and performed as small perturbation maneuvers about the 1-g flight condition at AOAs of approximately 10°, 20°, 30°, 40°, 50°, 60°, and 70°. The maneuvers were performed by the OBES while the vehicle was under RFCS control as described in the “Software Configuration” section. All maneuvers were analyzed assuming state noise was present as described earlier, although those maneuvers at approximately 10° AOA did not exhibit significant uncommanded motions caused by unsteady flow phenomena.

The OBES maneuvers were ideal for derivative extraction in that each of the four lateral-directional control surfaces ( $\delta_{dh}$ ,  $\delta_r$ ,  $\delta_a$ , and  $\delta_{yv}$ ) was independently commanded using a separate 4-sec doublet during each maneuver. Table 4 shows the control input amplitudes commanded by the OBES for all 26 maneuvers. Some variation in control input excitation and dynamic response was exhibited during maneuvers 10, 12, 16, and 20, which were flown on the first HARV PID flight (flight 155). Experience gained from these maneuvers proved useful in determining proper doublet sizes for maneuvers on subsequent flights. In some of the figures to follow, these early maneuvers are highlighted with flagged solid symbols.

The main deficiency of the maneuvers analyzed in this paper is that the maneuvers were performed at 10° AOA increments. A 10° increment is not sufficient (too large) to completely define the derivatives as functions of AOA, as substantial changes in a derivative can occur within as few as 2° or 3° AOA.

### High Angle of Attack Research Vehicle Stability and Control Maneuvers

Figure 6 shows a typical lateral-directional maneuver performed at approximately 10° AOA by the HARV. Figure 6(a) shows the flight condition parameters for the 24-sec maneuver. The AOA varied between 9° and 11°, the altitude was 30,300 ft, the Mach number was 0.50, and the dynamic pressure varied between 110 and 113 lb/ft<sup>2</sup>. Figure 6(b) shows the lateral-directional response variables used for PID: angle of sideslip ( $\beta$ ), roll rate ( $p$ ), yaw rate ( $r$ ), and lateral acceleration ( $a_Y$ ). Figure 6(c) shows the control inputs used to excite the vehicle response: differential stabilator deflection ( $\delta_{dh}$ ), rudder deflection ( $\delta_r$ ), aileron deflection ( $\delta_a$ ), equivalent pitch vane deflection ( $\delta_{pv}$ ), and equivalent yaw vane deflection ( $\delta_{yv}$ ). Figure 6(d) shows the individual vane deflections,  $V_1$ ,  $V_2$ ,  $V_3$ ,  $V_4$ ,  $V_5$ , and  $V_6$  plotted along with the computed left and right engine thrust,  $T_L$  and  $T_R$ , and the computed total engine thrust,  $T$ .

As figure 3 shows,  $V_1$ ,  $V_2$ , and  $V_3$  are the upper, outer, and inner vane deflections for the left engine; and  $V_4$ ,  $V_5$ , and  $V_6$  are the upper, outer, and inner vane deflections for the right engine. If the vanes are

Table 4. Summary of OBES-commanded control input amplitudes.

Maneuver number	Average $\alpha$ , deg	$\Delta\beta$ , deg	$\Delta\delta_{dh}$ , deg	$\Delta\delta_r$ , deg	$\Delta\delta_a$ , deg	$\Delta(\delta_{yv}/T)$ , deg
1	9.52	9.5	3	5	5	10
2	9.67	9	3	5	5	10
3	9.91	9	3	5	5	10
4	9.92	9	3	5	5	10
5	10.27	9	3	5	5	10
6	20.03	9	6	11	11	18
7	20.17	9	6	11	11	18
8	20.26	10	6	11	11	18
9	20.38	9	6	11	11	18
10	24.52	7	3	8	8	10
11	29.29	10	6	11	11	18
12	29.53	7	3	8	8	10
13	29.87	10	6	11	11	18
14	29.89	10	6	11	11	18
15	30.04	10	6	11	11	18
16	39.03	8	3	8	8	10
17	41.05	10	6	11	11	18
18	41.38	10	6	11	11	18
19	41.67	10	6	11	11	18
20	49.46	7	3	8	8	10
21	49.70	8	3	10	11	18
22	49.97	9	3	10	11	18
23	58.53	9	0	8	15	18
24	59.53	12	0	8	15	10
25	59.65	11	0	8	15	8
26	66.73	10	5	10	10	5

assumed to be touching the exhaust plume, the equivalent pitch vane and yaw vane inputs in figure 6(c) are defined by and calculated with the following equations:

$$\delta_{pv} = \left\{ \frac{\left[ V_1 - \left( \frac{V_2 + V_3}{2} \right) + V_4 - \left( \frac{V_6 + V_5}{2} \right) \right]}{2} \right\}^T \quad (28)$$

$$\delta_{yv} = \left\{ \frac{\left[ \frac{(V_2 - V_3)}{2} + \frac{(V_6 - V_5)}{2} \right]}{2} \right\} T \quad (29)$$

where  $T$  is equal to  $T_L + T_R$ . In figure 6(d), the individual vanes are plotted as lateral-directional effector pairs. That is, where the overplotted vane signals agree, a force and moment will result in the lateral-directional axes. Where the signals do not agree, a force and moment will result in the longitudinal axes. The degree to which the plotted vane signals of figure 6(d) agree or disagree in producing an adequate lateral-directional response is illustrated by examining the  $\delta_{pv}$  and  $\delta_{yv}$  signals in figure 6(c) that are computed from equations 27 and 28.

The maneuver shown in figure 6 was performed by the OBES with the aircraft under RFCS control, as were all 26 HARV maneuvers discussed in this report. The aircraft responses that are shown in figure 6(b) were the result of the control input excitation given in figure 6(c). Doublets were commanded by the OBES on each of the four vehicle controls in the following sequential order:  $\delta_{dh}$ ,  $\delta_r$ ,  $\delta_a$ , and  $\delta_{yv}$ . Figure 6(c) also shows the effect of feedback on these controls, for although the command is for a pure doublet, the actual control deflection is somewhat modified. These four somewhat-modified control doublets are all very distinct and independent, which is very desirable for PID analysis.

The primary reason to excite individual control doublets (using SSIs) is to guarantee that independent information exists for all of the controls and states. This independence assures the identifiability of each stability and control derivative. With a feedback system, the control motions can be defined as a function of the responses that are fed back and of the other control positions, thereby making the states and control positions almost linearly dependent (ref. 41), which is undesirable for identifiability. The independent doublet on each control assures that this near-linear dependence will not occur. All five maneuvers performed at approximately  $10^\circ$  AOA were very similar to the maneuver shown in figure 6. The SSI approach to PID maneuvers has been investigated on several other flight research programs, including the 3/8-scale F-15 Remotely Piloted Research Vehicle (ref. 58), the Space Shuttle Orbiter (ref. 66), and the recent and similarly thrust-vectoring X-31 vehicle (ref. 67).

Figure 7 shows a 25-sec lateral-directional maneuver that varies between  $28^\circ$  and  $32^\circ$  AOA. Figure 7(a) shows the flight condition; figure 7(b) shows the response variables; figure 7(c) shows the control variables; and figure 7(d) shows the engine thrust and vane positions. In later discussions where the HARV PID analysis is compared to the basic F-18 PID analysis described in reference 34, the time histories in figures 6 and 7 can be compared directly to the time histories in figures 4 and 7 of reference 34.

All 26 maneuvers were similar to the 2 maneuvers just presented in terms of maneuver duration, doublet sequence, and doublet shape as illustrated by the control doublets shown in figures 6(c) and 7(c). Nonetheless, the maneuver and input summary of table 4 shows two exceptions. First, the three maneuvers at approximately  $60^\circ$  AOA (maneuver numbers 23, 24, and 25) did not include doublets in  $\delta_{dh}$  (because the horizontal stabilator was near its maximum deflection limit); therefore, no  $\delta_{dh}$  derivatives were estimated for these maneuvers. Second, as previously mentioned, four of the earliest maneuvers had noticeably different doublet amplitudes than later maneuvers at similar AOA conditions. These maneuvers (numbers 10, 12, 16, and 20) are identified with flagged solid symbols in some of the stability and control derivative results to be presented. The  $10^\circ$  AOA maneuver shown in figure 6 is maneuver number 3 from table 4, and the  $30^\circ$  AOA maneuver shown in figure 7 is maneuver number 13.

The amplitudes of  $\beta$ ,  $\delta_{yv}/T$ , and the control inputs ( $\delta_{dh}$ ,  $\delta_r$ ,  $\delta_a$ ) shown in table 4 need some explanation. The amplitude of  $\Delta\beta$  and  $\Delta(\delta_{yv}/T)$  is the amount of maximum variation (peak-to-peak value) in  $\beta$  and  $\delta_{yv}/T$  during the maneuver. For example, comparisons of the  $\beta$  variation in figures 6(b) and 7(b) with corresponding values of  $\Delta\beta$  in table 4 (for maneuver numbers 3 and 13, respectively) illustrate how these values were selected. Conversely, the amplitude of a control input in table 4 is roughly the average value of the dwell (deflected) portion of the control input from its value just before and after the doublet, which can be nonzero at high AOA. In other words, the  $\Delta\delta$  given in the table denote control doublets of  $\pm\Delta\delta$  about a nominal deflection value (which may or may not be  $0^\circ$ ), and does not imply a total peak-to-peak variation as is the case with  $\Delta\beta$  and  $\Delta(\delta_{yv}/T)$ . Although the OBES command was for a pure doublet, the F-18 control system and the RFCS somewhat modify the control input, as figures 6(c) and 7(c) show.

## Stability and Control Derivative Results

The stability and control derivatives resulting from PID are presented and discussed in this section. Each derivative is plotted as a function of AOA where the symbols are the flight-determined estimates—also referred to as the flight estimates or flight values—and the vertical lines are the uncertainty levels. The uncertainty levels (ref. 41) shown on the plots are obtained by multiplying the Cramér-Rao bound of each estimate by a factor of 5. Theoretically, information on maneuver quality such as the duration of the maneuver, amount of response signal noise at the time of the control input, excitation of the response variables ( $\beta$ ,  $p$ ,  $r$ , and  $a_Y$ ), and the fit of the maneuver is contained in the value of the uncertainty level. A large uncertainty level indicates low information on the estimated derivative for that maneuver, and a small level indicates high information. In addition, several curves are plotted on top of the derivatives and represent one or more of the following (depending on the particular plot):

- fairings of the HARV flight estimates based on the authors' interpretation of the data.
- fairings of the prediction obtained from cold-jet thrust-vectoring tests (ref. 42) and a simulation based primarily on wind-tunnel data of the basic F-18 aircraft (refs. 68, 69).
- fairings of the basic F-18 flight estimates (ref. 34).
- final fairings based on both HARV and basic F-18 flight estimates.

The fairing of flight estimates is based primarily on the uncertainty levels, the scatter of adjacent estimates around a given AOA, and engineering judgment of the maneuver quality. Note that the aerodynamic wind-tunnel data used to characterize the prediction fairing was for the basic F-18 configuration and did not account for the external modifications made on the HARV, which included the thrust-vectoring apparatus and the LEX fences as discussed in the “Hardware Configuration” section.

The estimation of stability and control derivatives at high AOA is always difficult because of the uncertainty of the aerodynamic mathematical model and the occurrence of uncommanded responses during the dynamic maneuver. Although the derivatives are plotted as functions of AOA, other variables (such as altitude, Reynolds number, Mach number, and horizontal stabilator position) account for some of the scatter seen in the plotted estimates.

## HARV Derivatives

Figure 8 shows the sideslip derivatives  $C_{l_\beta}$ ,  $C_{n_\beta}$ , and  $C_{Y_\beta}$  as functions of AOA. The agreement of the flight-determined  $C_{l_\beta}$  with prediction (fig. 8(a)) is good at less than  $20^\circ$  AOA and at  $50^\circ$  AOA. The

estimates for the flight data are closely clustered (with the possible exception at approximately 20° AOA) and have relatively small uncertainty levels. The small uncertainties provide a fairly high confidence in the flight estimates, including those estimates at high AOA where associated vortex flows can complicate PID. Differences between the conditions at which the flight estimates are obtained and those at which the predicted values are obtained exist, however. The flight estimates of  $C_{l_\beta}$  were determined over a  $\Delta\beta$  range of variation of a maximum of 10°; this variation was true for nearly all of the flight maneuvers, as table 4 and figures 6(b) and 7(b) show. Because the  $\beta$  derivatives are usually nonlinear with sideslip angle, the range of sideslip over which the derivatives are defined makes a difference. The sideslip range for the predictions is likely smaller than the flight range  $\Delta\beta$ . In addition to differences in sideslip range, the LEX fences installed on the HARV would certainly be expected to affect  $C_{l_\beta}$  (especially in the AOA region greater than 25° dominated by strong vortical flow), a factor not accounted for in the predictions.

Figure 8(b) shows the general trend of decreasing  $C_{n_\beta}$  with AOA for flight and predicted values with good agreement from 30° to 40° AOA. The flight estimates are tightly clustered with small uncertainty levels around most AOAs. Again, possible explanations for the disagreement at other AOAs may include the range of sideslip variation of the flight maneuvers and HARV configuration modifications. In addition to any effect of the LEX fences, the additional surface area resulting from the aft-mounted thrust-vectoring apparatus would tend to make the flight-determined  $C_{n_\beta}$  somewhat larger than  $C_{n_\beta}$  would be without the apparatus.

Figure 8(c) shows flight-determined  $C_{Y_\beta}$  as a function of AOA with comparison to prediction. The flight estimates are somewhat higher (more positive) than predicted at less than 40° AOA, with good agreement at greater than 40° AOA. The tight clustering of flight data and small uncertainty levels at less than 40° AOA underscore the disagreement between flight and prediction, with possible explanations again including sideslip range and configuration differences.

Figure 9(a) shows the coefficient of rolling moment due to differential horizontal stabilator deflection,  $C_{l_{\delta_{dh}}}$ , with flight and predicted values as a function of AOA. The flight values show considerably more effectiveness from 10° to 30° AOA than the predicted values. The predicted values were corrected for stabilator position, which does not seem to explain the discrepancy. The flight variation for differential stabilator deflection,  $\Delta\delta_{dh}$ , is  $\pm 3^\circ$  or  $\pm 6^\circ$ , depending on the particular maneuver (table 4). (Figure 6(c) shows maneuver number 3 with a  $\pm 3^\circ$  variation, and figure 7(c) shows maneuver number 13 with a  $\pm 6^\circ$  variation.) Over what  $\delta_{dh}$  range the predicted values are determined is not known, but if the range were significantly different than the flight range, then that may account for the difference. The flight estimates are of very high quality, including those estimates at high AOA, as can be seen by the small amount of scatter and the relatively small uncertainty levels at the low AOAs.

Figure 9(b) shows the comparison between flight and predicted values for  $C_{n_{\delta_{dh}}}$ . The flight estimates show an increasingly larger negative value (adverse yaw) with increasing AOA in comparison with the prediction. The flight estimates are seen to be very good, as illustrated by the tight clustering of data at less than 50° AOA and the relatively small uncertainty levels at less than 40° AOA. The differences between flight and prediction are large and are probably only partially explained by differences in the respective ranges of  $\delta_{dh}$ .

Figure 9(c) shows the coefficient of lateral force due to differential horizontal stabilator deflection,  $C_{Y_{\delta_{dh}}}$ , for flight and predicted values as a function of AOA. Both values are quite small, but some differences can be seen, especially at approximately 40° AOA. The predicted values could be used as a fairing of the flight estimates everywhere except at approximately 40° AOA.

Figure 10(a) shows the comparison of the flight and predicted values for  $C_{l_{\delta_a}}$ . The flight value is 10 to 25 percent lower than predicted throughout the AOA range. The flight estimates are seen to be good, especially for high AOA, as the estimates are tightly clustered with relatively small uncertainty levels at less than 50° AOA. At approximately 10° AOA, the flight maneuvers have  $\Delta\delta_a$  amplitudes of approximately  $\pm 5^\circ$ , and elsewhere the maneuvers have  $\Delta\delta_a$  amplitudes of approximately  $\pm 11^\circ$ , except for the four flagged solid symbols. The four flagged values correspond to  $\Delta\delta_a$  amplitudes of approximately  $\pm 8^\circ$ . To study the  $\Delta\delta_a$  inputs closely, refer to figures 6(c) and 7(c) and table 4. The two flagged solid symbols at 25° and 30° AOA are in good agreement with the prediction, which may indicate that the prediction is based on a  $\Delta\delta_a$  range smaller than the  $\pm 11^\circ$  range of the other maneuvers.

Figure 10(b) shows the flight and predicted values of  $C_{n_{\delta_a}}$ . The flight values are smaller (less negative) than predicted throughout the range of AOA. A possible explanation for this feature is that the range of  $\Delta\delta_a$  for the prediction may be different than the range of  $\Delta\delta_a$  for the flight maneuvers as discussed above. This difference between flight and prediction fairings is substantial.

Figure 10(c) shows the comparison of flight and predicted values for  $C_{Y_{\delta_a}}$ . Both sets of values are small, but the flight and predicted values are of opposite sign at less than 30° AOA.

Figure 11(a) shows the flight and predicted values of  $C_{l_{\delta_r}}$  as a function of AOA. Good agreement exists at less than 30° AOA. The flight values are more positive than the predicted values at 30° AOA and greater. As table 4 shows, the maneuvers at approximately 10° AOA have a  $\Delta\delta_r$  of  $\pm 5^\circ$ , and most of the maneuvers at 20° AOA have a  $\Delta\delta_r$  of  $\pm 11^\circ$ . Given the good agreement at approximately 10° and at



20° AOA, the range of  $\Delta\delta_r$  for flight and predicted values does not seem like a plausible explanation for the differences between flight and prediction seen at the high AOAs.

Figure 11(b) shows the comparison of  $C_{n_{\delta_r}}$  for flight and predicted values. Very good agreement exists between flight and predicted values throughout the AOA range, with the predicted effectiveness being somewhat larger (more negative) than the flight estimates at approximately 10° AOA and slightly less negative for AOAs greater than 20°.

Figure 11(c) shows the comparison of  $C_{Y_{\delta_r}}$  for flight and predicted values. Again, the agreement is very good throughout the AOA range. The predicted values make a plausible fairing of the flight estimates.

Figure 12 shows the rotary derivatives  $C_{l_p}$ ,  $C_{n_p}$ ,  $C_{l_r}$ , and  $C_{n_r}$  as functions of AOA along with comparisons of flight and predicted values. The flight values of  $C_{l_p}$  (fig. 12(a)) are less damped than predicted at greater than 25° AOA. The flight and predicted values of  $C_{n_p}$  (fig. 12(b)) are both very small at less than 50° AOA and agree well with each other at 30° AOA and less. The flight values of  $C_{l_r}$  (fig. 12(c)) are less than predicted throughout the AOA range. Both flight and predicted values of  $C_{n_r}$  (fig. 12(d)) are damped for all AOAs, with the flight values being significantly more damped at 20° and 50° AOA.

Figures 13(a), 13(b), and 13(c) show the coefficients of rolling moment, yawing moment, and lateral force due to yaw vane deflection ( $C_{l_{\delta_{yv}}}$ ,  $C_{n_{\delta_{yv}}}$ , and  $C_{Y_{\delta_{yv}}}$ , respectively). These coefficients are different than the other stability and control derivatives discussed in this report because of the nature of the thrust-vectoring control. The moment and force are a result of the deflection of the engine exhaust plume when the thrust-vectoring vanes are actuated. The mechanization and software driving the thrust vectoring are described in the “Vehicle Description” section. Details on the prediction of the effectiveness of the thrust vectoring have previously been published (refs. 42–45). Thrust-vectoring effectiveness is defined in terms of the effective plume-deflection angle, measured from the nominal (undeflected) thrust line. When the vane is against or inside the plume, this effectiveness has been calculated from prediction in reference 42 to be 0.563 deg/deg or 0.00982 rad/deg, which is the ratio of plume deflection to vane deflection for nozzle pressure ratios of 2. The data in reference 42 also show that a similar value is true for nozzle pressure ratios of 3 and 5. All 26 maneuvers presented here had nozzle pressure ratios between 3 and 5.

Yaw vane effectiveness is different than the other stability and control derivatives studied in this report in that the  $\delta_{yv}$  derivatives are not functions of flight condition such as velocity or dynamic pressure. Because of this difference, the  $C_{l_{\delta_{yv}}}$ ,  $C_{n_{\delta_{yv}}}$ , and  $C_{Y_{\delta_{yv}}}$  derivatives are normalized by dividing the moment (ft-lb) and force (lbf) by both the thrust and the vane deflection (as given in eq. 29). Therefore, the units of  $C_{l_{\delta_{yv}}}$  and  $C_{n_{\delta_{yv}}}$  are ft/deg, and the units of  $C_{Y_{\delta_{yv}}}$  are  $\text{deg}^{-1}$ . The thrust is calculated for each sample point using the method described in reference 46. Then,  $\delta_{yv}$  is calculated by equation 29 and is used as an input to the equations of motion. The derivatives  $C_{l_{\delta_{yv}}}$ ,  $C_{n_{\delta_{yv}}}$ , and  $C_{Y_{\delta_{yv}}}$  are then estimated the same way as all the other derivatives, as described in the “Parameter Identification Formulation” section. The predicted value of  $C_{l_{\delta_{yv}}}$  (fig. 13(a)) is 0 ft/deg; the predicted value of  $C_{n_{\delta_{yv}}}$  (fig. 13(b)), based on a moment arm of approximately 20 ft between the aircraft CG and the center of the vanes, is 0.196 ft/deg; and the predicted value of  $C_{Y_{\delta_{yv}}}$  (fig. 13(c)) is  $-0.0098 \text{ deg}^{-1}$ .

Figure 13(a) shows the comparison between flight and predicted values of  $C_{l_{\delta_{yv}}}$  as a function of AOA. The “zero value” of both flight and prediction are in excellent agreement. This value is expected, as no intended rolling moment due to  $\delta_{yv}$  is introduced by the TVCS.

Figure 13(b) shows the comparison of flight and predicted values of  $C_{n_{\delta_{yv}}}$  as a function of AOA. The flight estimates are slightly higher than predicted for AOAs less than  $30^\circ$  and are in good agreement elsewhere. The flagged solid symbols indicate the four maneuvers from the first flight where the variation in vane deflection,  $\Delta\delta_{yv}$ , was  $\pm 10^\circ$ , in contrast to the other maneuvers at  $20^\circ$  AOA and greater in which the variation was  $\pm 18^\circ$ . All four of these flagged flight estimates show the highest values of  $C_{n_{\delta_{yv}}}$  for their AOA range, and therefore indicate that vane effectiveness may be somewhat higher for small  $\delta_{yv}$  deflections than for large deflections, which is consistent with findings in reference 42. Moreover, the five flight estimates grouped at approximately  $10^\circ$  AOA, in which the  $\Delta\delta_{yv}$  was only  $\pm 10^\circ$ , clearly show a higher estimate than predicted.

To see how the flight estimates can be higher than predicted is difficult because the prediction represents the ideal case where the vane effectiveness is at a maximum (corresponding to a plume-to-vane deflection ratio of  $0.563 \text{ deg/deg}$  (ref. 42)); an explanation of this difference is attempted. Reference 37 presents loads data for the instrumented left-engine vanes. The reference discusses the presence of a resulting load on the undeflected vanes opposite the deflected vanes (a condition called “plume pinching”). The reference also shows that the deflected vanes are essentially touching or just inside the

plume such that the effectiveness of the vanes is not affected by an uncertainty in the relationship between the vane positions and the exhaust plume. Therefore, along with other possible explanations, the most likely explanation for the difference in prediction and flight is that the thrust calculation used to define  $\delta_{yv}$  for  $\Delta\delta_{yv} = \pm 10^\circ$  is at least 10 percent too high, which is particularly evident for maneuvers at  $10^\circ$  AOA (which all have  $\Delta\delta_{yv} = \pm 10^\circ$ ).

Figure 13(c) shows the comparison of  $C_{Y_{\delta_{yv}}}$  for flight and predicted values as a function of AOA. Virtually all of the flight estimates are more negative than predicted. Again, the most negative estimates tend to be from maneuvers with small vane deflections; that is, the maneuvers with flagged solid symbols and those at approximately  $10^\circ$  AOA. These values, along with the explanation given above, support the probability that the thrust estimate may be 10 percent too high at  $10^\circ$  AOA, where  $\Delta\delta_{yv} = \pm 10^\circ$ , as was seen for  $C_{n_{\delta_{yv}}}$ .

Based on the above discussion, the argument can be made that the calculated thrust used in this analysis was at least 10 percent too high for flight maneuvers with the lower  $\Delta\delta_{yv}$  ( $\pm 10^\circ$ ). Further supporting this conclusion, reference 37 also shows flight estimates of  $C_{N_{\delta_{pv}}}$  to be 10 percent higher for small vane deflections at low AOA than their ideal values where no plume pinching occurred. All three derivatives,  $C_{N_{\delta_{pv}}}$ ,  $C_{n_{\delta_{yv}}}$ , and  $C_{Y_{\delta_{yv}}}$ , are independently estimated, and all three show that the calculated thrust is probably too high.

Figure 14 shows the flight estimates of  $C_{l_0}$ ,  $C_{n_0}$ , and  $C_{Y_0}$  as functions of AOA. At greater than  $50^\circ$  AOA, these coefficients show significant values other than zero. This characteristic is not unusual for very high AOA flight conditions, where strong vortices exist off the forebody and LEX of the HARV. The biases  $C_{l_0}$  and  $C_{n_0}$  show very definite and strong trends indicating that these vortices are probably asymmetric. The next section will compare the flight-determined derivatives of the HARV with those of the basic F-18 aircraft that were previously reported (ref. 34).

## Comparison of HARV and Basic F-18 Derivatives

The results of PID for the basic F-18 aircraft (without thrust-vectoring modifications) were previously published in reference 34. In this section, those results will be compared with the HARV results from the previous section. As reported in reference 34, the stability and control maneuvers for the basic F-18 aircraft were less than ideal. Both the basic F-18 and HARV maneuvers were hampered by uncommanded responses resulting from separated and vortical flows typical of flight at high AOAs. However, the basic F-18 maneuvers had several other drawbacks that made them even less desirable, as discussed in detail in reference 34. These drawbacks were primarily caused by the basic F-18 control

system introducing relatively high correlations (near-linear dependence) between the control variables and the feedback response variables. In addition, the various interconnects between the aileron ( $\delta_a$ ), differential stabilator ( $\delta_{dh}$ ), and rudder ( $\delta_r$ ) deflections made separation of the individual effects of these control derivatives less than ideal. In contrast, because of the implementation of the RFCS and the OBES on the HARV, the effects of the feedback variables and control dependencies were nearly eliminated, as described in the “HARV Stability and Control Maneuvers” section.

In the remainder of this section, the stability and control derivative estimates and associated uncertainty levels for the HARV and for the basic F-18 aircraft (taken from reference 34) will be plotted alongside each other. These plots will be discussed, and a combined “final” flight fairing will be defined based on the results from both aircraft. Some small configuration differences exist (such as the LEX fences and the thrust-vectoring mechanism) that will not be completely accounted for in the final fairings. The HARV estimates will be represented by “o” symbols and the basic F-18 estimates by “x” symbols. As with the other flight fairings, the “final” fairing will also be determined by considering the uncertainty levels (Cramér-Rao bound times 5 for all data points), the scatter of the adjacent estimates, and engineering judgment of the maneuver quality. In some instances, a dual fairing may be appropriate, indicating separate fairings for different ranges of the primary variable (for example, different sideslip or control input ranges). These different ranges will be mentioned in each applicable case. In general, any fairing at less than 9° AOA will be based on the basic F-18 aircraft because no HARV data exist in this range.

Figure 15(a) shows the flight estimates of  $C_{l_\beta}$  for both the HARV and the basic F-18 aircraft (ref. 34) as a function of AOA. The uncertainty levels between 9° and 40° AOA are significantly smaller for the HARV estimates than for the F-18 estimates. At less than 30° AOA, good agreement exists between the HARV and F-18 estimates. Between 30° and 39° AOA, the estimates are exclusively basic F-18 estimates with a large amount of scatter and large uncertainty levels. These points do not effect the final fairing because of the tight clustering and small uncertainty levels of the HARV estimates at approximately 30° and 40° AOA. However, at approximately 43° AOA, a basic F-18 estimate exists that has a very small uncertainty level that is significantly smaller than any of the nearby HARV estimates. Therefore, the final fairing deviates from the trend of the HARV-only data. This deviation may seem unwarranted, but a change of 2° or 3° AOA in flight can show a marked change in the separated and vortical flows at high AOA and thus in  $C_{l_\beta}$ . The balance of the fairing (the portion at greater than 50° AOA) is based solely on the HARV estimates because no F-18 estimates are available.

Figure 15(b) shows HARV and basic F-18 flight estimates for  $C_{n_\beta}$ . At greater than 39° AOA, both sets of data agree; and between 19° and 39° AOA, the HARV estimates are more tightly clustered and have locally smaller uncertainty levels than the F-18 estimates. Therefore, the final fairing at greater than 19° AOA is identical to the HARV fairing. At approximately 14° AOA, two F-18 estimates exist with reasonably good uncertainty levels, so the final fairing includes the uncertainty levels for these two points in the absence of any nearby HARV estimates. At less than 9°, many F-18 estimates exist with small uncertainty levels and no HARV estimates. The final fairing includes these points although the fairing requires a rapid change in  $C_{n_\beta}$  because the data at less than 9° are tightly clustered and have small

uncertainty levels. This change occurs over  $2^\circ$  or  $3^\circ$  AOA, and these types of changes in  $C_{n_\beta}$  magnitude (0.0006) are not uncommon. However, the rapid change may also be caused by a difference in the range of  $\beta$  during the stability and control maneuver. The range of  $\beta$  ( $\Delta\beta$ ) for all of the F-18 maneuvers was less than  $4^\circ$ . The  $\Delta\beta$  for all the HARV maneuvers was approximately  $9^\circ$ , as shown in table 4. Therefore, this rapid change in the fairing may actually indicate that two fairings are needed; one for the  $\Delta\beta$  of  $4^\circ$  for the F-18 estimates and one for the  $\Delta\beta$  of  $9^\circ$  for the HARV estimates. The same may also be true for the two F-18 estimates at  $20^\circ$  AOA because the estimates were extracted for a  $\Delta\beta$  maneuver of  $6^\circ$ ; the HARV estimates at  $20^\circ$  AOA were extracted from maneuvers with a  $\Delta\beta$  of  $9^\circ$  to  $10^\circ$ .

Figure 15(c) has all of the flight estimates of  $C_{Y_\beta}$  from both the HARV and basic F-18 aircraft as functions of AOA. As before, the final fairing at less than  $9^\circ$  AOA is the same as the basic F-18 fairing (ref. 34). The final fairing between  $20^\circ$  and  $30^\circ$  AOA has been lowered somewhat from the HARV-only fairing to incorporate the basic F-18 estimates with similar uncertainty levels as the single HARV estimate between  $20^\circ$  and  $30^\circ$  AOA.

Figure 16 shows all of the flight estimates for the equivalent lateral control deflection,  $\delta_L$ . Figures 16(a), 16(b), and 16(c) present derivatives  $C_{l_{\delta_L}}$ ,  $C_{n_{\delta_L}}$ , and  $C_{Y_{\delta_L}}$ , respectively, as functions of AOA. The  $\delta_L$  derivatives are defined as follows:

$$C_{l_{\delta_L}} = C_{l_{\delta_a}} + 0.42C_{l_{\delta_{dh}}} \quad (30)$$

$$C_{n_{\delta_L}} = C_{n_{\delta_a}} + 0.42C_{n_{\delta_{dh}}} \quad (31)$$

$$C_{Y_{\delta_L}} = C_{Y_{\delta_a}} + 0.42C_{Y_{\delta_{dh}}} \quad (32)$$

These derivatives result from the control system of the basic F-18 aircraft (explained in detail in ref. 34) simultaneously moving  $\delta_a$  and  $\delta_{dh}$  according to equations 30 to 32 for flight at greater than  $15^\circ$  AOA. In order to compare the basic F-18 and HARV estimates, the HARV estimates, uncertainties, and fairing for the  $\delta_a$  and  $\delta_{dh}$  derivatives were converted to the equivalent  $\delta_L$  derivative using equations 30 to 32 (fig. 16). Note that flight estimates of the basic F-18 aircraft are only plotted for AOAs greater than  $15^\circ$ ; at less than  $15^\circ$  AOA, additional control surfaces move simultaneously with  $\delta_a$  and  $\delta_{dh}$  such that the resulting control derivative cannot be compared directly with the HARV using equations 30 to 32.

Figure 16(a) compares HARV and basic F-18 flight estimates of  $C_{l_{\delta_L}}$  as a function of AOA. Two final fairings (solid curves) are shown. The longer fairing is identical to the HARV fairing, and the shorter fairing is nearly the same as the fairing reported in reference 34 for the basic F-18 aircraft between  $20^\circ$  and  $45^\circ$  AOA. The reason for showing two final fairings is because the shapes and amplitudes of the

$\delta_a$  and  $\delta_{dh}$  doublets are different between the HARV and basic F-18 aircraft. The shapes of all of the HARV doublets are the same: the doublet rises rapidly from the “zero” position to the doublet amplitude in one direction, holds that value for approximately 2 sec, then rapidly switches sign to the doublet amplitude in the opposite direction, holds that value for approximately 2 sec, and then returns to zero to complete the 4-sec doublet. These waveforms can be seen in the control inputs of figures 6(c) and 7(c). Between 20° and 49.5° AOA (see table 4), all but four of the HARV maneuvers have doublet amplitudes of  $\Delta\delta_a = \pm 11^\circ$  and  $\Delta\delta_{dh} = \pm 6^\circ$ . The other four maneuvers have doublet amplitudes of  $\Delta\delta_a = \pm 8^\circ$  and  $\Delta\delta_{dh} = \pm 3^\circ$  and are denoted as flagged solid symbols in figure 16(a).

In contrast, for the basic F-18 aircraft, the entire  $\delta_L$  maneuver doublet is completed in approximately 1 to 1.5 sec, which is three to four times as rapid as the complete HARV 4-sec doublet. These waveforms can be seen in the control inputs of figure 7(c) of reference 34, repeated here as figure 16(d). In addition, the maximum amplitude for the basic F-18 doublet is determined by the control system; figure 6 in reference 34 shows that the maximum amplitude for  $\delta_a = 6^\circ$  and for  $\delta_{dh} = 2.6^\circ$  for flight at 25° and at greater than 25° AOA. Reference 34 also shows that basic F-18 doublets resemble sinusoids rather than classic square waves, minimizing the dwell time spent at the maximum amplitudes (see fig.16(d)). Thus by comparison, whereas almost all of the HARV  $\delta_a$  doublets dwell near  $\pm 11^\circ$  for 4 sec and the  $\delta_{dh}$  doublets dwell near  $\pm 6^\circ$  for 4 sec, the basic F-18  $\delta_a$  doublets dwell near  $\pm 6^\circ$  for less than 1 sec, and the  $\delta_{dh}$  doublets dwell near  $\pm 2.6^\circ$  for less than 1 sec. Moreover, whereas for nearly all of the HARV maneuvers, the average positive values for  $\delta_a$  is  $11^\circ$  and for  $\delta_{dh}$  is  $6^\circ$ ; for the basic F-18 maneuvers, the average positive value for  $\delta_a$  is  $3^\circ$  and for  $\delta_{dh}$  is  $1.75^\circ$  or less. Similar averages for negative values of each input can be seen for each aircraft.

Thus, referring again to figure 16(a), the unflagged HARV maneuvers have  $|\delta_a| \approx 11^\circ$  and  $|\delta_{dh}| \approx 6^\circ$ , and the basic F-18 maneuvers have  $|\delta_a| \approx 3^\circ$  and  $|\delta_{dh}| \approx 1.75^\circ$ . These values mean that  $|\delta_L|$  for the unflagged HARV maneuvers is 3 to 4 times  $|\delta_L|$  for the basic F-18 aircraft. Therefore, the longer solid fairing in figure 16(a) represents  $C_{l_{\delta_L}}$  for  $|\delta_a| \approx 11^\circ$  and  $|\delta_{dh}| \approx 6^\circ$ , and the shorter solid fairing represents  $C_{l_{\delta_L}}$  for  $|\delta_a| \approx 3^\circ$  and  $|\delta_{dh}| \approx 1.75^\circ$ . The flagged circles for the most part lie between the two fairings as would be expected because they represent HARV estimates with 30 percent lower  $\delta_a$  and 50 percent lower  $\delta_{dh}$  amplitude than the rest of the HARV estimates.

Figure 16(b) shows both HARV and basic F-18 flight estimates for  $C_{n_{\delta_L}}$  as a function of AOA. Two final fairings are given here with the same rationale as was given above for  $C_{l_{\delta_L}}$ . The shorter fairing has been adjusted slightly from the basic F-18 fairing (ref. 34) to conform better with the overall fairing of the

HARV estimates. The longer final fairing and the HARV fairing overlap each other. Interpreted together, the two fairings show that more adverse yaw exists for large deflections than for small deflections.

Figure 16(c) shows the comparison of the flight estimate of  $C_{Y_{\delta_L}}$  as a function of AOA. The final fairing is the unaltered HARV fairing presented in the last section, and the fairing adequately represents all of the data and is consistent with the scatter and uncertainty levels of the estimates.

Figure 17(a) shows HARV and basic F-18 flight estimates of  $C_{l_{\delta_r}}$  as a function of AOA. The HARV flight fairing is consistent with all of the basic F-18 flight estimates and uncertainty levels except for the F-18 estimate at approximately 43° AOA. The final fairing is raised slightly in this local AOA region to accommodate this point. The final fairing is also drawn to agree with the basic F-18 estimates at less than 9° AOA because no HARV estimates were obtained in this region.

Figure 17(b) shows the flight estimates of  $C_{n_{\delta_r}}$  as a function of AOA. The final fairing at greater than 9° AOA is the same as the HARV fairing, except for lowering the fairing a little between 20° and 30° AOA. This adjustment is made to include several basic F-18 estimates with relatively small uncertainty levels. The fairing at less than 9° AOA needs some explanation because the fairing shows a rapid reduction in rudder effectiveness between 8° and 10° AOA. Estimate clusters at 6° to 8° AOA for the basic F-18 aircraft and estimate clusters at approximately 10° AOA for the HARV are tightly clustered with small uncertainty levels. In order to assess if this jump may be caused by differences in doublet amplitude (as was the case for  $C_{l_{\delta_L}}$ ), similar observations are considered for  $C_{n_{\delta_r}}$ . The 4-sec HARV doublets at approximately 10° AOA used  $|\delta_r| = 5^\circ$  (see table 4). The 1-sec doublets of the basic F-18 aircraft from 6° to 8° AOA varied from  $|\delta_r|$  of 3° to 20°. As figure 17(b) shows, this range of  $|\delta_r|$  for the basic F-18 aircraft nonetheless resulted in similar values of  $C_{n_{\delta_r}}$  estimates and uncertainty levels. This range also spans the HARV doublet amplitude of  $|\delta_r| = 5^\circ$ . Therefore, the jump in  $C_{n_{\delta_r}}$  cannot be attributed to differences in  $|\delta_r|$  alone. A possibility exists that the longer dwell time (2 sec) for the HARV (as opposed to 0 to 0.3 sec for the basic F-18 aircraft) may be a contributing factor, but insufficient information exists to conclude that. Therefore, the most likely cause of the jump in the value of  $C_{n_{\delta_r}}$  is an effect of AOA. This jump is similar to that found for  $C_{n_{\beta}}$ , but to a lesser extent than was just shown for  $C_{n_{\delta_r}}$ .

Figure 17(c) shows HARV and basic F-18 flight estimates for  $C_{Y_{\delta_r}}$  as a function of AOA. The HARV flight fairing is a very good final fairing of all of the data. The basic F-18 fairing is used to complete the final fairing at less than 9° AOA.

Figure 18 shows all of the flight estimates for the rotary derivatives ( $C_{l_p}$ ,  $C_{n_p}$ ,  $C_{l_r}$ , and  $C_{n_r}$ ) as functions of AOA. At less than  $9^\circ$  AOA, the basic F-18 flight fairing (ref. 34) is used for all the rotary derivatives because the fairing merges nicely with all of the data in this AOA range. At greater than  $9^\circ$  AOA, the HARV flight fairing is used for all of the rotary derivatives except when estimates from the basic F-18 aircraft indicate small modifications to the HARV fairing. The fairing for  $C_{l_p}$  in figure 18(a) is modified at approximately  $15^\circ$  to better reflect the two data points from the basic F-18 airplane. The fairing for  $C_{l_r}$  in figure 18(c) is modified at  $10^\circ$  AOA to allow a more reasonable merging of the two original flight fairings. A modification from the HARV fairing at approximately  $25^\circ$  AOA was made in figure 18(d) for  $C_{n_r}$  to better represent the single HARV estimate and several of the basic F-18 estimates. The comparison of the rotary derivatives shows that the HARV estimates are more tightly clustered and the uncertainty levels are, in general, considerably smaller than those of the basic F-18 estimates in all regions. These conclusions result from the consistent HARV maneuver implementations and the reduced correlations between control and rotary derivatives, both of which are direct results of the RFCS and OBES implementations (see the “Software Configuration” section). These conclusions are particularly evident in the two most important rotary derivatives,  $C_{l_p}$  and  $C_{n_r}$ , at less than  $50^\circ$  AOA. Both  $C_{l_p}$  and  $C_{n_r}$  can be troublesome derivatives to estimate at low AOA but are often nearly impossible to obtain at high AOA. For the HARV, however, the high quality data system, the excellent maneuvers with low effective feedback gains and independent control deflections, and the state noise PID algorithm have all contributed to improving the estimation of the rotary derivatives.

Overall, the HARV estimates are seen to define the final flight fairings much better because of their tight clustering and relatively small uncertainty levels. These estimate characteristics are primarily a result of the excellent quality and near repeatability of the flight maneuvers and the modeling of the uncommanded motions with the state noise algorithm described in the PID methodology section. The two primary factors for modifying the HARV flight fairings with basic F-18 estimates were the effect of different amplitude ranges for  $\beta$  and for  $\delta_a$  and  $\delta_{dh}$  inputs, and the paucity of HARV estimates for AOA other than those clustered at  $10^\circ$ ,  $20^\circ$ ,  $30^\circ$ ,  $40^\circ$ , and  $50^\circ$  AOA. These two reasons are not inherent drawbacks to the HARV maneuvers or PID method; these reasons are issues only because the complete maneuver set did not include maneuvers to define these characteristics. That  $10^\circ$  AOA increments are too large to define the trends of stability and control derivatives is well known. That  $2^\circ$  AOA increments are needed to provide meaningful AOA trends throughout the flight envelope can be argued. The final fairings for  $C_{n_\beta}$  and  $C_{n_{\delta_r}}$  between  $5^\circ$  and  $10^\circ$  AOA certainly help support the argument for  $2^\circ$  increments at less than  $10^\circ$  AOA. Increments of  $5^\circ$  are probably adequate for most of the high-AOA region. If more detailed PID characterization is needed, additional maneuvers can be flown to fill in the desired AOA values. If better definition of the stability and control derivatives is needed as a function of variable or control deflection range, an appropriate adjustment (reprogramming) in the OBES can be made to provide



suitable maneuvers with either larger or smaller size doublets. These considerations were not requirements for the HARV program, but the discussions in this section indicate that these considerations would have provided a more straightforward and well-defined interpretation of the HARV data than using the much less desirable basic F-18 estimates.

## Summary of HARV, Basic F-18, and Predicted Derivatives

Figures 19 to 24 show summaries of the fairings for each derivative as a function of AOA. These stand-alone fairings (without data points and uncertainty levels) make seeing the trends between flight and prediction easier. The differences between the HARV-only fairing and final fairing were discussed in the last section, but presenting the differences in this format provides a clear comparison. Again, the predictions do not account for the LEX fences nor the thrust-vectoring apparatus, which may explain some of the differences seen.

The final fairing made the agreement between flight and prediction slightly better than the HARV fairing alone for the following derivatives:  $C_{l_\beta}$ ,  $C_{Y_\beta}$ ,  $C_{n_{\delta_L}}$ ,  $C_{n_{\delta_r}}$ ,  $C_{l_p}$ , and  $C_{n_r}$ . The final fairing made the agreement between flight and prediction slightly worse for  $C_{l_{\delta_L}}$  and  $C_{l_{\delta_r}}$ . Figure 23 shows fairings for the  $\delta_{dh}$  derivatives, and figure 24 shows the  $\delta_a$  derivatives. In these figures, the final fairing is the same as the HARV fairing because no estimates exist from the basic F-18 aircraft to suggest modification. Identifying individual  $\delta_{dh}$  and  $\delta_a$  derivatives from the basic F-18 aircraft was not possible because of the various interconnects and correlations introduced by the basic F-18 flight control system, as explained earlier. The  $\delta_{yv}$  derivatives shown in figure 13 have no counterpart for the basic F-18 aircraft; therefore, they are not repeated for these figures.

## CONCLUSIONS

The lateral-directional stability and control derivatives of the F-18 High Angle of Attack Research Vehicle (HARV) equipped with thrust vectoring have been determined from subsonic, dynamic flight data using a maximum likelihood parameter identification (PID) technique. The technique uses the linearized aircraft equations of motion and accounts for thrust-vectoring terms and state and measurement noise. State noise is used to model the uncommanded forcing function caused by unsteady flows at high angles of attack. A specialized research flight control system (RFCS) controls the integration of aerodynamic and thrust-vectoring controls. The PID maneuvers were performed “hands-off” by an onboard excitation system (OBES) working through the RFCS to allow for single-surface inputs. The

independent inputs were ideal for parameter identification by eliminating correlations between control variables and response variables introduced by feedback from the high-gain control augmentation system. A total of 26 maneuvers has been analyzed, each maneuver featuring doublets in aileron ( $\delta_a$ ), differential stabilator ( $\delta_{dh}$ ), and rudder ( $\delta_r$ ) deflection and equivalent yaw vane input ( $\delta_{yv}$ ). The following derivatives are determined from the flight maneuvers and are plotted as functions of angle of attack:  $C_{l_\beta}$ ,  $C_{l_p}$ ,  $C_{l_r}$ ,  $C_{l_{\delta_a}}$ ,  $C_{l_{\delta_{dh}}}$ ,  $C_{l_{\delta_r}}$ ,  $C_{l_{\delta_{yv}}}$ ,  $C_{l_0}$ ,  $C_{n_\beta}$ ,  $C_{n_p}$ ,  $C_{n_r}$ ,  $C_{n_{\delta_a}}$ ,  $C_{n_{\delta_{dh}}}$ ,  $C_{n_{\delta_r}}$ ,  $C_{n_{\delta_{yv}}}$ ,  $C_{n_0}$ ,  $C_{Y_\beta}$ ,  $C_{Y_{\delta_a}}$ ,  $C_{Y_{\delta_{dh}}}$ ,  $C_{Y_{\delta_r}}$ ,  $C_{Y_{\delta_{yv}}}$ , and  $C_{Y_0}$ . Comparisons have been made with predictions obtained from laboratory cold-jet thrust-vectoring tests and a simulation based primarily on wind-tunnel data from the basic F-18 aircraft. Comparisons have also been made to flight-determined derivatives of the basic F-18 aircraft. Configurationally, the basic F-18 aircraft differs from the HARV by not having leading-edge-extension fences nor the aft-mounted thrust-vectoring apparatus. These configuration differences probably contributed to some of the difference seen between flight-determined and predicted derivatives values.

The results are presented in three sets of figures: first, showing HARV flight-determined derivatives with fairings for the flight values and for predicted values; second, showing flight-determined derivatives of both the HARV and basic F-18 with fairings for both aircraft and for a “final” fairing combining the two sets of derivatives; and third, showing the HARV flight fairing, the prediction fairing, and the “final” fairing. In addition to the stability and control derivative values extracted by PID, these results reveal several important conclusions:

- The preprogrammed doublet maneuvers performed by the OBES were repeatable and accurate in wave form (in terms of amplitude, dwell time, full-cycle duration, and overall square-wave shape), resulting in tight clustering of flight-estimated derivatives near a given angle of attack, low data scatter, and small uncertainty levels. In contrast, pilot-input doublets performed with the basic F-18 aircraft were deficient in wave form and repeatability, resulting in significantly greater data scatter and large uncertainty levels.
- The main deficiency of the HARV maneuvers in the current study was that the maneuvers were performed at 10° angle-of-attack increments. These increments were too large to adequately define the derivatives as functions of angle of attack because notable differences can occur over 2° or 3° angle of attack, as shown by comparing HARV derivatives with basic F-18 derivatives at other angles of attack. These increments were known to be too large, but at the time, no HARV program requirement existed to investigate smaller increments. Increments of 2° or 3° angle of attack would have been ideal, although increments of 5° angle of attack would probably have been sufficient.
- Uncommanded responses at high angles of attack caused by separated and vortical flows were accounted for and modeled as state noise in the PID formulation.

- The thrust-vectoring derivatives  $C_{Y_{\delta_{yv}}}$  and  $C_{n_{\delta_{yv}}}$  show more effectiveness for smaller  $\delta_{yv}$  inputs than for larger  $\delta_{yv}$  inputs, with the most likely explanation being that the thrust calculation used to define  $\delta_{yv}$  is a minimum of 10 percent too high.
- HARV derivative fairings were modified as indicated by considering estimates from the basic F-18 aircraft that had small uncertainty levels, which helped account for differences in variable ranges and the paucity of HARV maneuvers at angles of attack other than 10°, 20°, 30°, 40°, and 50°. This modification resulted in slightly improved comparisons between flight and prediction for  $C_{l_\beta}$ ,  $C_{Y_\beta}$ ,  $C_{n_{\delta_L}}$ ,  $C_{n_{\delta_r}}$ ,  $C_{l_p}$ , and  $C_{n_r}$  and slightly degraded comparisons for  $C_{l_{\delta_L}}$  and  $C_{l_{\delta_r}}$ .

*Dryden Flight Research Center  
National Aeronautics and Space Administration  
Edwards, California, March 30, 1998*

## REFERENCES

1. Chambers, J. R., "High-Angle-of-Attack Aerodynamics: Lessons Learned," AIAA-86-1774, June 1986.
2. Chambers, Joseph R., "High-Angle-of-Attack Technology: Progress and Challenges," in *High-Angle-of-Attack Technology - Volume 1*, NASA CP-3149 Part 1, May 1992, pp. 1–22. (Note: ITAR restricted. Distribution authorized to U. S Government agencies and their contractors; other requests shall be referred to WL/FIMS, Wright-Patterson AFB, Ohio 45433-6503.)
3. Gilbert, William P. and Donald H. Gatlin, "Review of the NASA High-Alpha Technology Program," *High-Angle-of-Attack Technology - Volume 1*, NASA CP-3149 Part 1, May 1992, pp. 23–59.
4. Chambers, Joseph R., William P. Gilbert, and Luat T. Nguyen, eds., *High-Angle-of-Attack Technology - Volume 1*, NASA CP-3149 Part 1, May 1992.
5. Matheny, Neil W., compiler, *High-Angle-of-Attack Projects and Technology Conference*, vols. 1–4, NASA CP-3207, Apr. 1992.
6. Regenie, Victoria, compiler, *Fourth NASA High Alpha Conference*, vols. 1–4, NASA CP-10143, July 1994.
7. Meyn, Larry A., Wendy R. Lanser, and Kevin D. James, "Full-Scale High Angle-of-Attack Tests of an F/A-18," AIAA-92-2676, June 1992.
8. Pettit, Chris L., Dansen L. Brown, Michael P. Banford, and Ed Pendleton, "Full-Scale Wind-Tunnel Pressure Measurements of an F/A-18 Tail During Buffet," *Journal of Aircraft*, vol. 33, no. 6, Nov.–Dec. 1996, pp. 1148–1156.
9. Asbury, Scott C. and Francis J. Capone, *Multiaxis Thrust-Vectoring Characteristics of Model Representative of the F-18 High-Alpha Research Vehicle at Angles of Attack From 0° to 70°*, NASA TP-3531, Dec. 1995.
10. Erickson, Gary E., *Wind Tunnel Investigation of Vortex Flows on F/A-18 Configuration at Subsonic Through Transonic Speed*, NASA TP-3111, Dec. 1991.
11. Cummings, Russell M., Yehia M. Rizk, Lewis B. Schiff, and Neal M. Chaderjian, "Navier-Stokes Predictions of the Flowfield Around the F-18 (HARV) Wing and Fuselage at Large Incidence," AIAA-90-0099, Jan. 1990.
12. Rizk, Yehia M. and Ken Gee, "Unsteady Simulation of Viscous Flowfield Around F-18 Aircraft at Large Incidence," *Journal of Aircraft*, vol. 29, no. 6, Nov.–Dec. 1992, pp. 986–992.
13. Murman, Scott M., Lewis B. Schiff, and Yehia M. Rizk, "Numerical Simulation of the Flow About an F-18 Aircraft in the High-Alpha Regime," AIAA-93-3405, Aug. 1993.
14. Murman, Scott M., Yehia M. Rizk, and Lewis B. Schiff, "Coupled Numerical Simulation of the External and Engine Inlet Flows for the F-18 at Large Incidence," AIAA-92-2621, June 1992.

15. Ghaffari, Farhad, *Navier-Stokes, Flight, and Wind Tunnel Flow Analysis for the F/A-18 Aircraft*, NASA TP-3478, Dec. 1994.
16. Gilbert, William P., Luat T. Nguyen, and Joseph Gera, "Control Research in the NASA High-Alpha Technology Program," in AGARD-CP-465, *Aerodynamics of Combat Aircraft Control and of Ground Effects*, pp. 3-1-3-18.
17. Pahle, Joseph W., Bruce Powers, Victoria Regenie, Vince Chacon, Steve Degroote, and Steven Murnyak, *Research Flight-Control System Development for the F-18 High Alpha Research Vehicle*, NASA TM-104232, Apr. 1991.
18. Foster, John V., W. T. Bundick, and Joseph W. Pahle, "Controls for Agility Research in the NASA High-Alpha Technology Program," SAE 912148, Sept. 1991.
19. Davidson, John B., John V. Foster, Aaron J. Ostroff, Frederick J. Lallman, Patrick C. Murphy, Keith D. Hoffler, and Michael D. Messina, "Development of a Control Law Design Process Utilizing Advanced Synthesis Methods with Application to the NASA F-18 HARV," in *High-Angle-of-Attack Projects and Technology Conference*, vol. 4, NASA CP-3207, Apr. 1992, pp. 111-157. (Note: ITAR restricted. Distribution authorized to U. S Government agencies and their contractors; other requests shall be referred to WL/FIMS, Wright-Patterson AFB, Ohio 45433-6503.)
20. Ostroff, Aaron J., Keith D. Hoffler, and Melissa S. Proffitt, *High-Alpha Research Vehicle (HARV) Longitudinal Controller: Design, Analyses, and Simulation Results*, NASA TP-3446, July 1994.
21. Bowers, Albion H., Joseph W. Pahle, R. Joseph Wilson, Bradley C. Flick, and Richard L. Rood, *An Overview of the NASA F-18 High Alpha Research Vehicle*, NASA TM-4772, Oct. 1996.
22. Fisher, David F., John H. Del Frate, and Fanny A. Zuniga, *Summary of In-Flight Flow Visualization Obtained From the NASA High Alpha Research Vehicle*, NASA TM-101734, Jan. 1991.
23. Fisher, David F., David M. Richwine, and Daniel W. Banks, *Surface Flow Visualization of Separated Flows on the Forebody of an F-18 Aircraft and Wind-Tunnel Model*, NASA TM-100436, May 1988. (Also available as AIAA-88-2112.)
24. Fisher, David F., John H. Del Frate, and David M. Richwine, *In-Flight Flow Visualization Characteristics of the NASA F-18 High Alpha Research Vehicle at High Angles of Attack*, NASA TM-4193, May 1990.
25. Fisher, David F., D. W. Banks, and David M. Richwine, *F-18 High Alpha Research Vehicle Surface Pressures: Initial In-Flight Results and Correlation With Flow Visualization and Wind-Tunnel Data*, NASA TM-101724, 1990.
26. Del Frate, John H., David F. Fisher, and Fanny A. Zuniga, *In-Flight Flow Visualization With Pressure Measurements at Low Speeds on the NASA F-18 High Alpha Research Vehicle*, NASA TM-101726, 1990 (also presented at AGARD Vortex Flow Aerodynamics Conference, Scheveningen, Netherlands, Oct. 1-4, 1990).
27. Richwine, David M. and David F. Fisher, *In-Flight Leading-Edge Extension Vortex Flow-Field Survey Measurements on an F-18 Aircraft at High Angle of Attack*, NASA TM-4398, 1992. (Also available as AIAA-91-3248 using color reproduction.)

28. Shah, Gautam H., "Wind Tunnel Investigation of Aerodynamic and Tail Buffet Characteristics of Leading-Edge Extension Modifications to the F/A-18," AIAA-91-2889, Aug. 1991.
29. Lee, B. H. K. and F. C. Tang, "Characteristics of the Surface Pressures on a F/A-18 Vertical Fin Due to Buffet," *Journal of Aircraft*, vol. 31, no. 1, Jan.–Feb. 1994, pp. 228–235.
30. Meyn, Larry A. and Kevin D. James, "Full-Scale Wind-Tunnel Studies of F/A-18 Tail Buffet," *Journal of Aircraft*, vol. 33, no. 3, May–June 1996, pp. 589–595.
31. Gee, Ken, Scott M. Murman, and Lewis B. Schiff, "Computation of F/A-18 Tail Buffet," *Journal of Aircraft*, vol. 33, no. 6, Nov.–Dec. 1996, pp. 1181–1189.
32. Klein, Vladislav, Thomas P. Ratvasky, and Brent R. Cobleigh, *Aerodynamic Parameters of High-Angle-of-Attack Research Vehicle (HARV) Estimated From Flight Data*, NASA TM-102692, Aug. 1990.
33. Klein, Vladislav, "Aerodynamic Characteristics of High-Angle-of-Attack Research Vehicle (HARV) Determined From Flight Data," in *High-Angle-of-Attack Technology - Volume 1*, NASA CP-3149 part 1, May 1992, pp. 265–278.
34. Iliff, Kenneth W. and Kon-Sheng Charles Wang, *Extraction of Lateral-Directional Stability and Control Derivatives for the Basic F-18 Aircraft at High Angles of Attack*, NASA TM-4786, Feb. 1997.
35. Murri, Daniel G., Robert T. Biedron, Gary E. Erickson, Frank L. Jordan, Jr., and Keith D. Hoffler, "Development of Actuated Forebody Strake Controls for the F-18 High Alpha Research Vehicle," in *High-Angle-of-Attack Technology - Volume 1*, NASA CP-3149 part 1, May 1992, pp. 335–380.
36. Murri, Daniel G., Gautam H. Shah, Daniel J. DiCarlo, and Todd W. Trilling, "Actuated Forebody Strake Controls for the F-18 High-Alpha Research Vehicle," *Journal of Aircraft*, vol. 32, no. 3, May–June 1995, pp. 555–562. (Also available as AIAA-93-3675, Aug. 1993.)
37. Iliff, Kenneth W. and Kon-Sheng Charles Wang, *Flight-Determined Subsonic Longitudinal Stability and Control Derivatives of the F-18 High Angle of Attack Research Vehicle (HARV) With Thrust Vectoring*, NASA TP-97-206539, Dec. 1997.
38. Regenie, Victoria, Donald Gatlin, Robert Kempel, and Neil Matheny, *The F-18 High Alpha Research Vehicle: A High-Angle-of-Attack Testbed Aircraft*, NASA TM-104253, Sept. 1992. (Also available as AIAA-92-4121, Aug. 1992.)
39. Chacon, Vince, Joseph W. Pahle, and Victoria A. Regenie, *Validation of the F-18 High Alpha Research Vehicle Flight Control and Avionics Systems Modifications*, NASA TM-101723, Oct. 1990. (Also presented as paper for IEEE 9th Digital Avionics Systems Conferences, Virginia Beach, Virginia, Oct. 15–18, 1990.)
40. Regenie, Victoria A., Michael Earls, Jeanette Le, and Michael Thomson, *Experience With Ada on the F-18 High Alpha Research Vehicle Flight Test Program*, NASA TM-104259, Oct. 1992.
41. Iliff, Kenneth W. and Richard E. Maine, *Practical Aspects of Using a Maximum Likelihood Estimation Method to Extract Stability and Control Derivatives From Flight Data*, NASA TN-D-8209, Apr. 1976.

42. Bowers, Albion H. and Joseph W. Pahle, *Thrust Vectoring on the NASA F-18 High Alpha Research Vehicle*, NASA TM-4771, Nov. 1996.
43. Bowers, Albion H., Gregory K. Noffz, Sue B. Grafton, Mary L. Mason, and Lee R. Peron, *Multiaxis Thrust Vectoring Using Axisymmetric Nozzles and Postexit Vanes on an F/A-18 Configuration Vehicle*, NASA TM-101741, May 1991. (Also available in NASA CP-3149, vol. 1, part 2, May 1992, pp. 829–862.)
44. Mason, Mary L., Francis J. Capone, and Scott C. Asbury, *A Static Investigation of the Thrust Vectoring System of the F/A-18 High-Alpha Research Vehicle*, NASA TM-4359, June 1992.
45. Johnson, Steven A., *Aircraft Ground Test and Subscale Model Results of Axial Thrust Loss Caused by Thrust Vectoring Using Turning Vanes*, NASA TM-4341, Jan. 1992.
46. Ray, Ronald J., *Evaluation of Various Thrust Calculation Techniques on an F404 Engine*, NASA TP-3001, Apr. 1990.
47. Heller, Michael J., “Theory and Implementation of the HARV/TVCS Mixer Predictor, NASA Contract NAS2-12661: NASA High Alpha Research Vehicle Thrust Vectoring Control System (HARV-TVCS),” Report HARV-MJH-12, McDonnell Aircraft Co., McDonnell Douglas Corp., St. Louis, Missouri, Aug. 10, 1989.
48. Peron, Lee R. and Thomas Carpenter, *Thrust Vectoring for Lateral-Directional Stability*, NASA CR-186016, 1992.
49. Bundick, W. Thomas, Joseph W. Pahle, Jessie C. Yeager, and Fred L. Beissner, Jr., *Design of a Mixer for the Thrust-Vectoring System on the High-Alpha Research Vehicle*, NASA TM-110228, June 1996.
50. Moes, Timothy R. and Stephen A. Whitmore, *A Preliminary Look at Techniques Used to Obtain Airdata From Flight at High Angles of Attack*, NASA TM-101729, Dec. 1990.
51. Whitmore, Stephen A., Timothy R. Moes, and Terry J. Larson, *Preliminary Results From a Subsonic High Angle-of-Attack Flush Airdata Sensing (HI-FADS) System: Design, Calibration, and Flight Test Evaluation*, NASA TM-101713, Jan. 1990. (Also available as AIAA-90-0232, Jan. 1990.)
52. Whitmore, Stephen A., *Development of a Pneumatic High-Angle-of-Attack Flush Airdata Sensing (HI-FADS) System*, NASA TM-104241, Nov. 1991.
53. Moes, Timothy R., Stephen A. Whitmore, and Frank L. Jordan, *Flight and Wind-Tunnel Calibrations of a Flush Airdata Sensor at High Angles of Attack and Sideslip and at Supersonic Mach Numbers*, NASA TM-104265, 1993. (Also presented as AIAA-93-1017, Feb. 1993.)
54. Richwine, David M., Robert E. Curry, and Gene V. Tracy, *A Smoke Generator System for Aerodynamic Flight Research*, NASA TM-4137, Sept. 1989.
55. Yuhas, Andrew J., Ronald J. Ray, Richard R. Burley, William G. Steenken, Leon Lechtenberg, and Don Thornton, *Design and Development of an F/A-18 Inlet Distortion Rake: A Cost and Time Saving Solution*, NASA TM-4722, Oct. 1995.

56. Smith, C. Frederic, Steve D. Podleski, Wendy S. Barankiewicz, and Susan Z. Zeleznik, "Comparison of F/A-18A Inlet Flow Analyses with Flight Data part 1," *Journal of Aircraft*, vol. 33, no. 3, May–June 1996, pp. 457–462.
57. Smith, C. Frederic, Steve D. Podleski, Wendy S. Barankiewicz, and Susan Z. Zeleznik, "Comparison of F/A-18A Inlet Flow Analyses with Flight Data part 2," *Journal of Aircraft*, vol. 33, no. 3, May–June 1996, pp. 463–469.
58. Iliff, Kenneth W., Richard E. Maine, and Mary F. Shafer, *Subsonic Stability and Control Derivatives for an Unpowered, Remotely Piloted 3/8-Scale F-15 Airplane Model Obtained From Flight Test*, NASA TN D-8136, Jan. 1976.
59. Iliff, K. W., "Identification and Stochastic Control with Application to Flight Control in Turbulence," UCLA-ENG-7340, Ph.D. Dissertation, University of California Los Angeles, California, May 1973.
60. Maine, R. E. and K. W. Iliff, *Identification of Dynamic Systems*, AGARD-AG-300, vol. 2, Jan. 1985. (Also available as NASA RP-1138, Feb. 1985.)
61. Iliff, Kenneth W., "Identification and Stochastic Control of an Aircraft Flying in Turbulence," *Journal of Guidance and Control*, vol. 1, no. 2, Mar.–Apr. 1978, pp. 101–108.
62. Iliff, Kenneth W. and Lawrence W. Taylor, Jr., *Determination of Stability Derivatives From Flight Data Using a Newton-Raphson Minimization Technique*, NASA TN D-6579, Mar. 1972.
63. Maine, Richard E. and Kenneth W. Iliff, *Application of Parameter Estimation to Aircraft Stability and Control - The Output-Error Approach*, NASA RP-1168, June 1986.
64. Etkin, Bernard, *Dynamics of Flight—Stability and Control*, 2nd ed., John Wiley & Sons, New York, 1982.
65. Maine, Richard E. and Kenneth W. Iliff, *User's Manual for MMLE3, a General FORTRAN Program for Maximum Likelihood Parameter Estimation*, NASA TP-1563, Nov. 1980.
66. Iliff, Kenneth W. and Mary F. Shafer, *Extraction of Stability and Control Derivatives From Orbiter Flight Data*, NASA TM-4500, June 1993.
67. Weiss, Susanne, Holger Friehmelt, Ermin Plaetschke, and Detlef Rohlf, "X-31A System Identification Using Single-Surface Excitation at High Angles of Attack," *Journal of Aircraft*, vol. 33, no. 3, May–June 1996, pp. 485–490.
68. McDonnell Aircraft Company, "F/A-18 Basic Aerodynamic Data," MDC A8575, McDonnell Douglas Corporation, St. Louis, Missouri, 1984.
69. Pelikan, R. J. and R. L. Swingle, "F/A-18 Stability and Control Data Report," vols. I and II, MDC A7247, Rev. B, McDonnell Aircraft Co., McDonnell Douglas Corp., St. Louis, Missouri, Nov. 1982.





EC91 0010-006

Figure 1. The F-18 High Angle of Attack Research Vehicle (HARV).

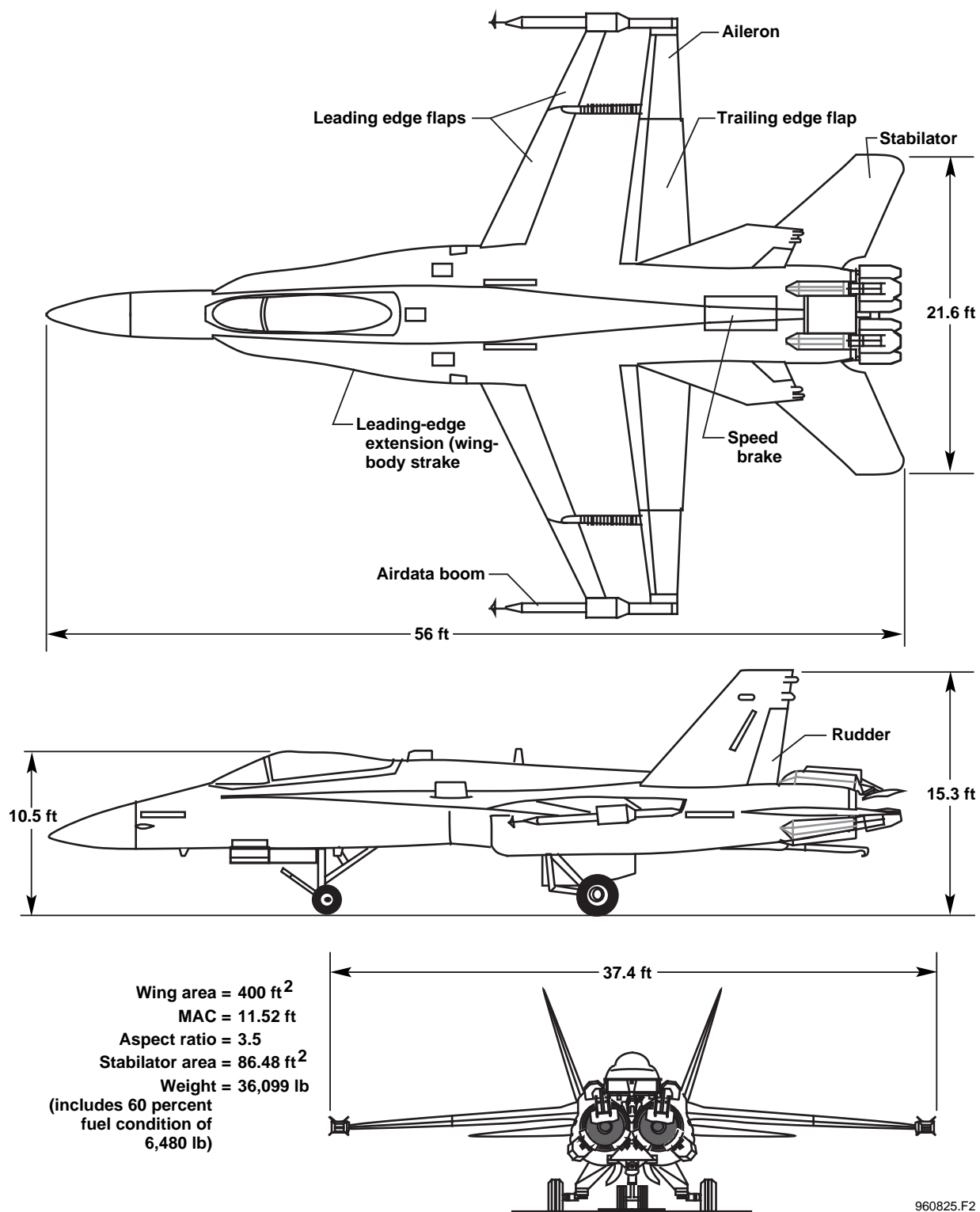


Figure 2. Three-view drawing of the F-18 HARV with major dimensions shown.

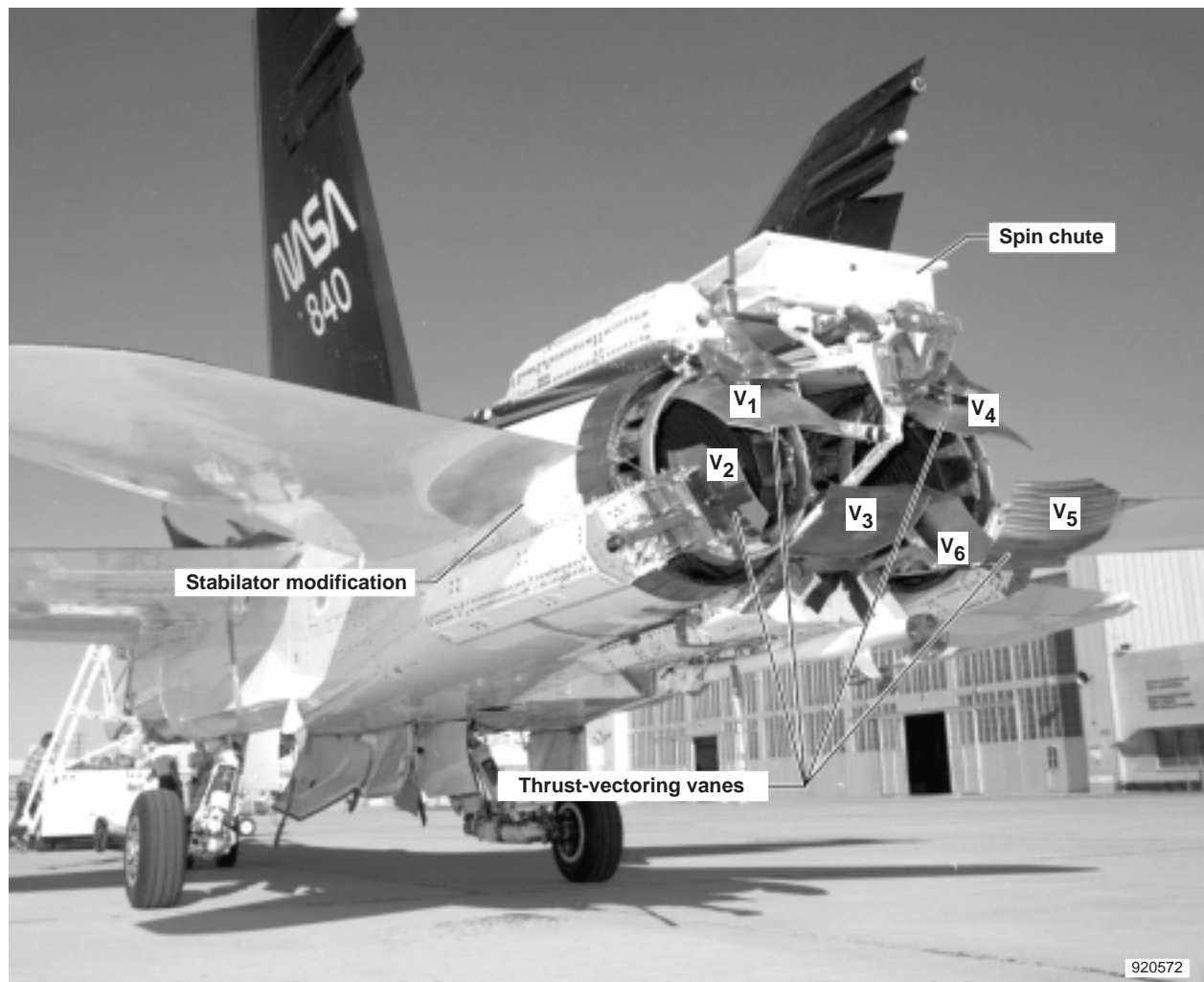


Figure 3. Thrust-vectoring control system (TVCS) hardware modification.

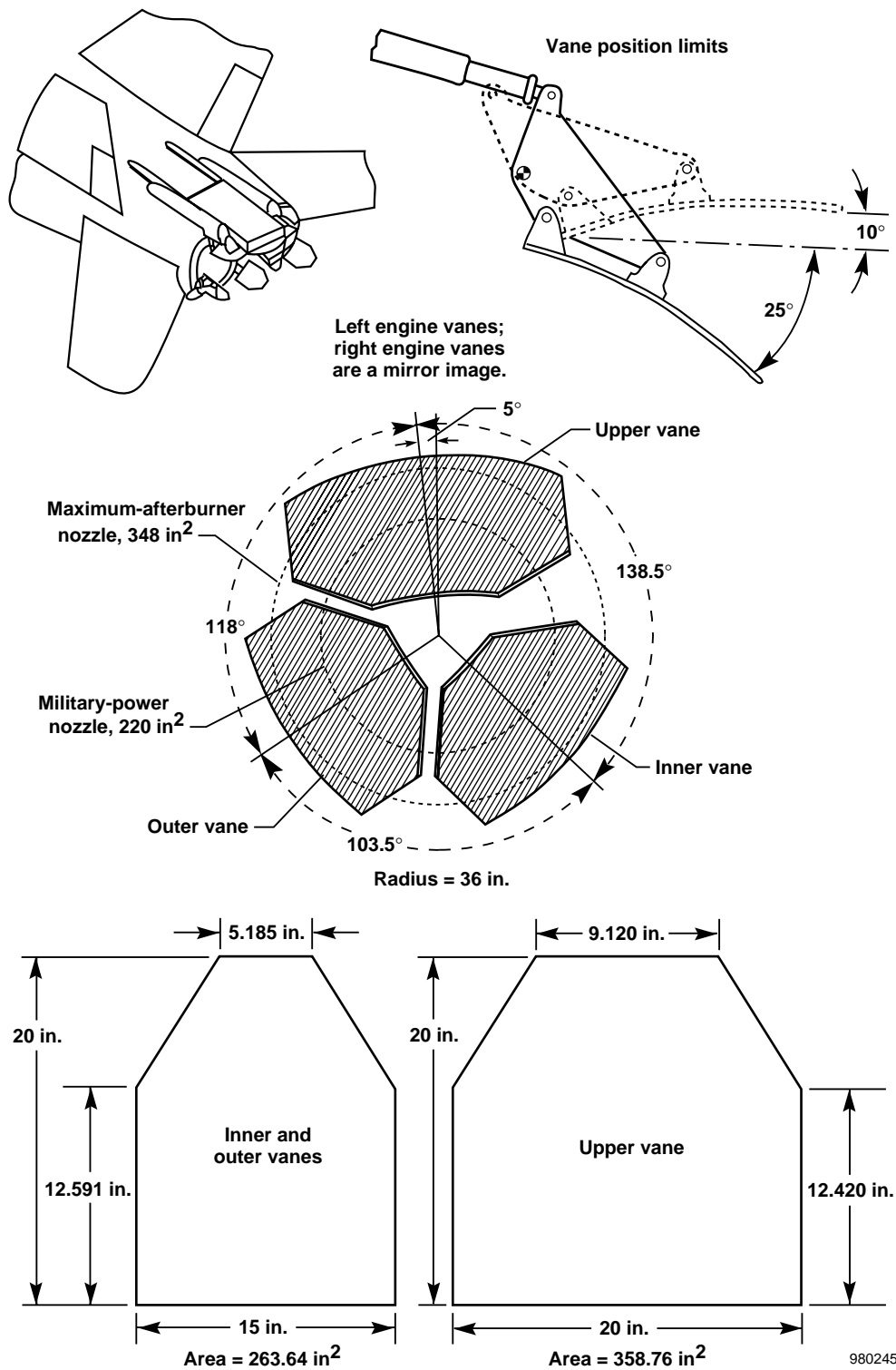
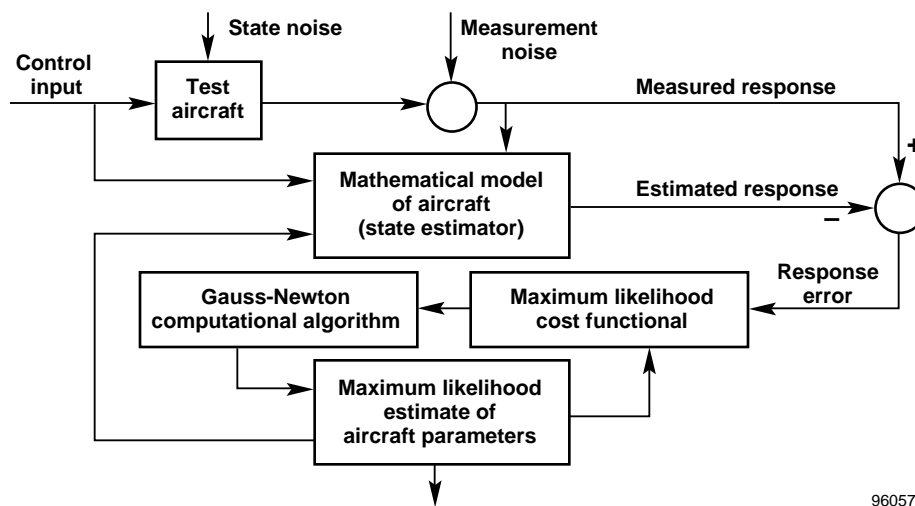
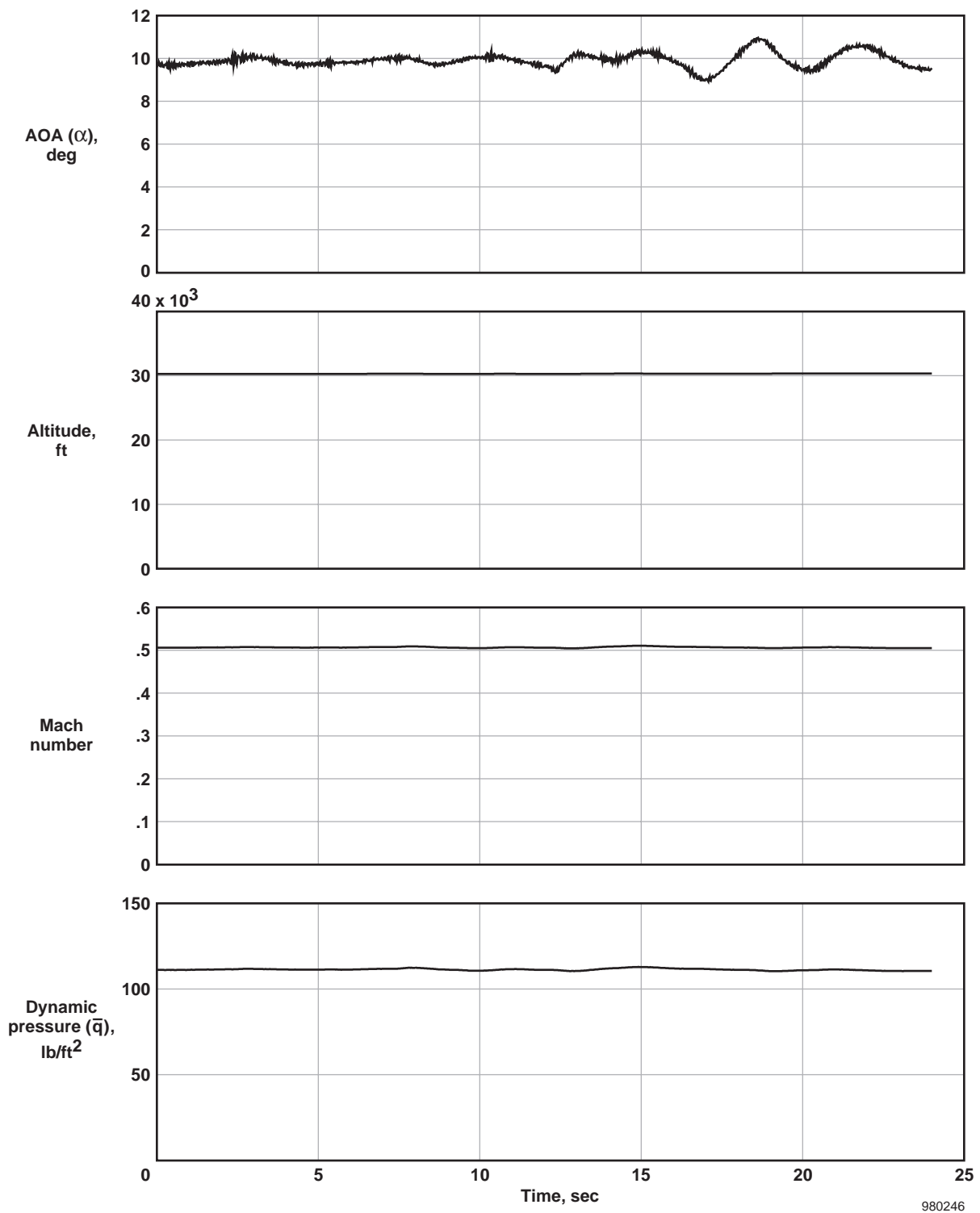


Figure 4. Four-view drawing of the TVCS.



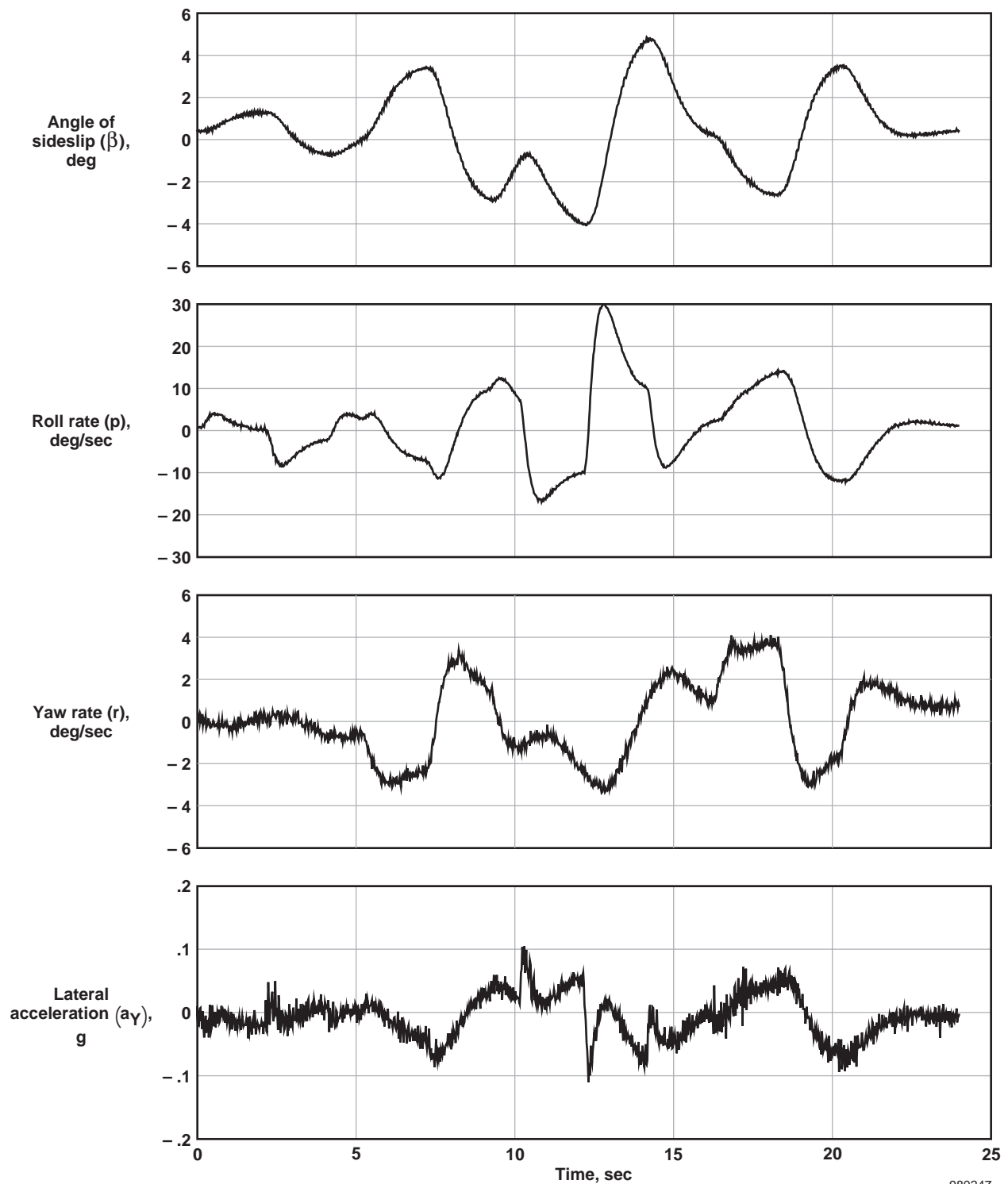
960578

Figure 5. The maximum likelihood estimation concept with state and measurement noise.



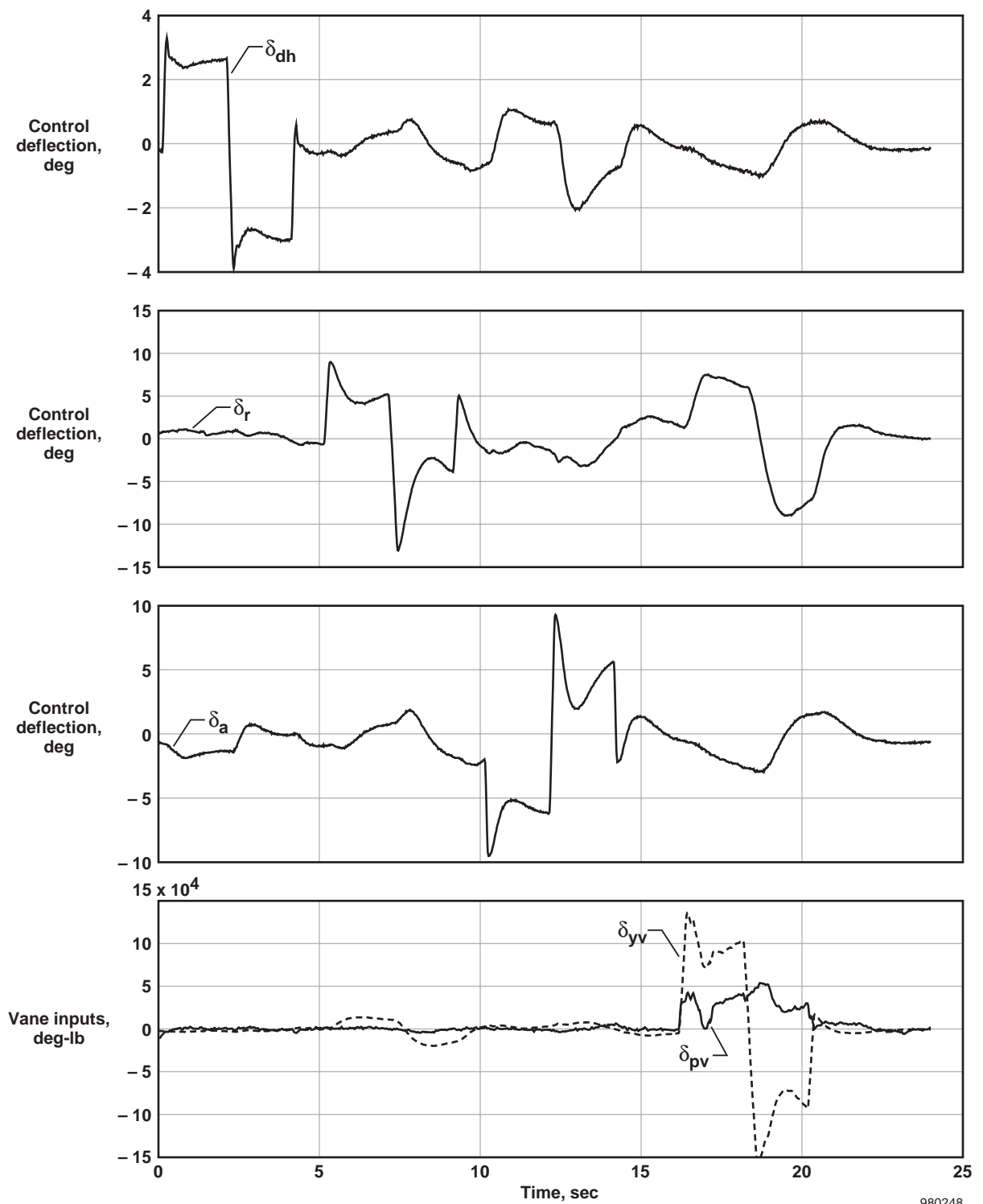
(a) Flight condition.

Figure 6. Time history data from a typical 10° AOA lateral-directional PID maneuver.



(b) Vehicle response variables.

Figure 6. Continued.

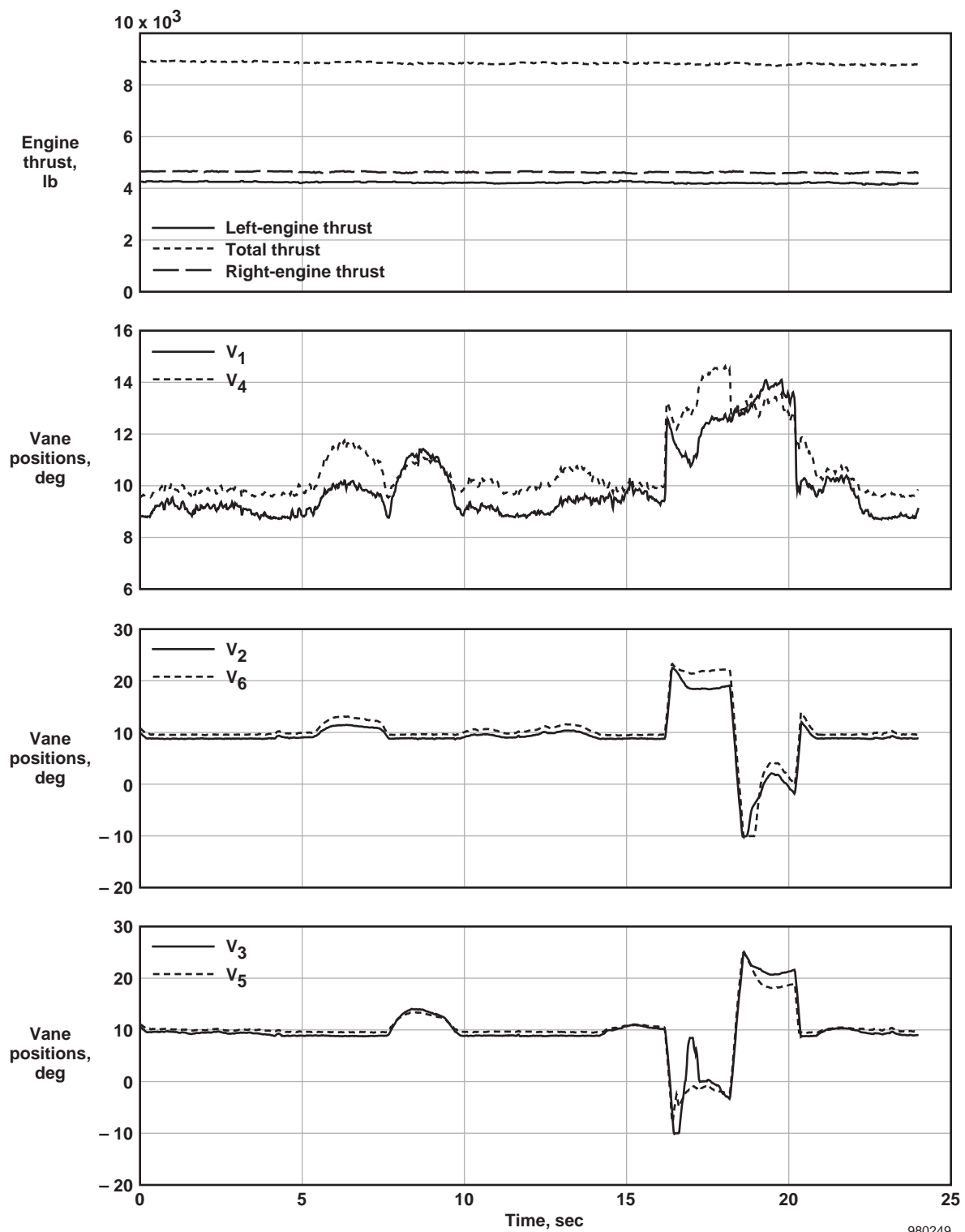


980248

(c) Control (input) variables.

Figure 6. Continued.

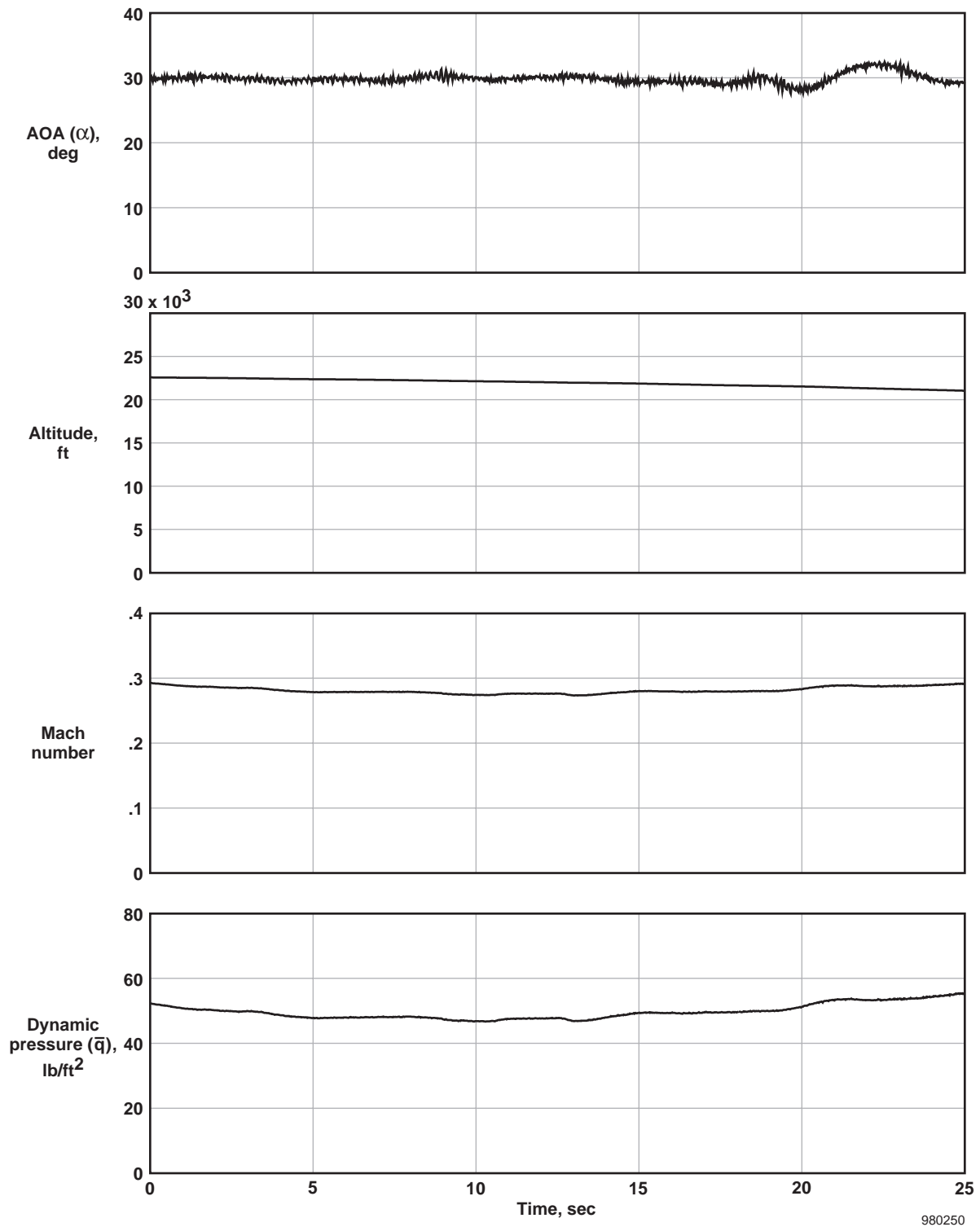




980249

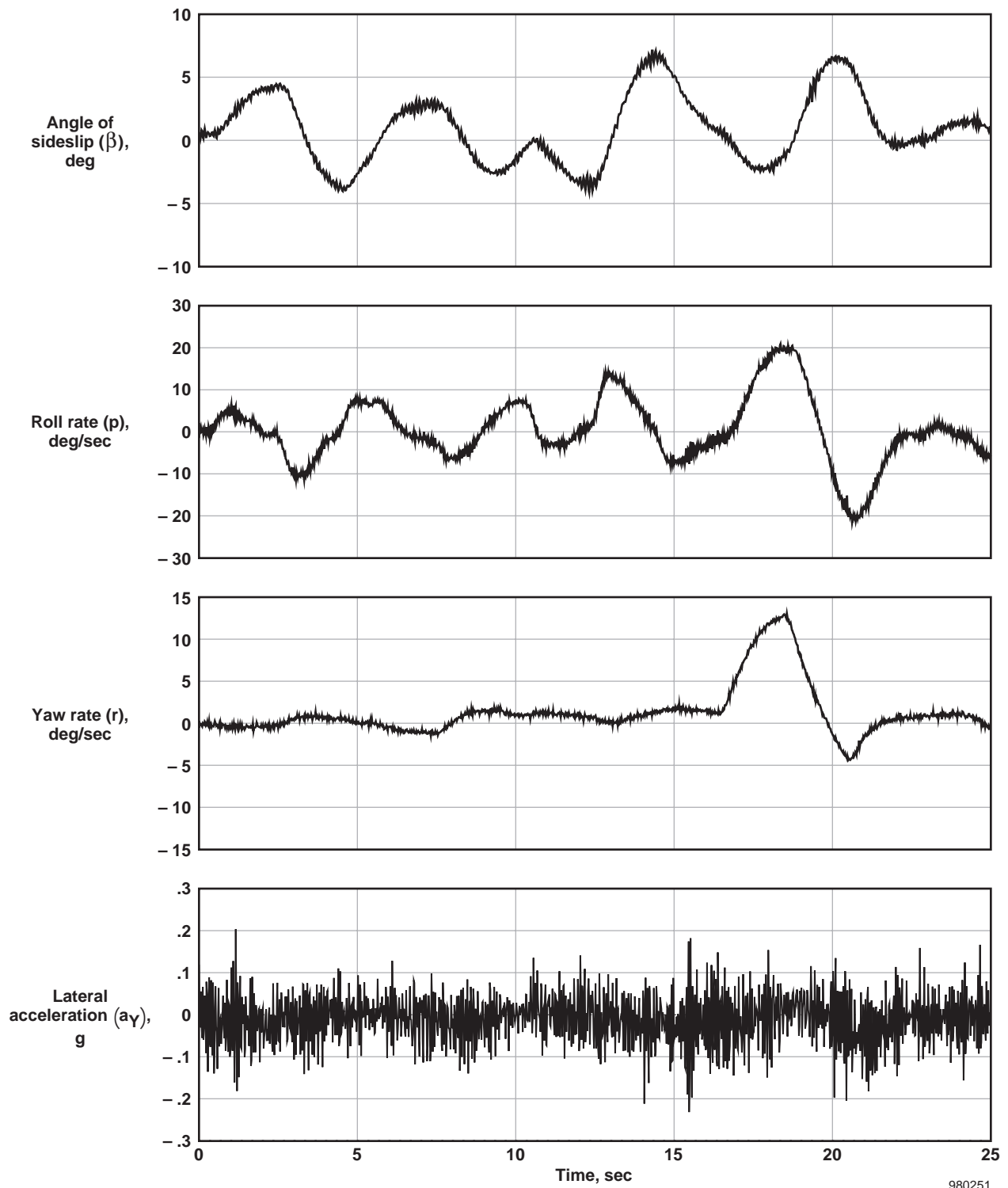
(d) Engine thrust and vane positions.

Figure 6. Concluded.

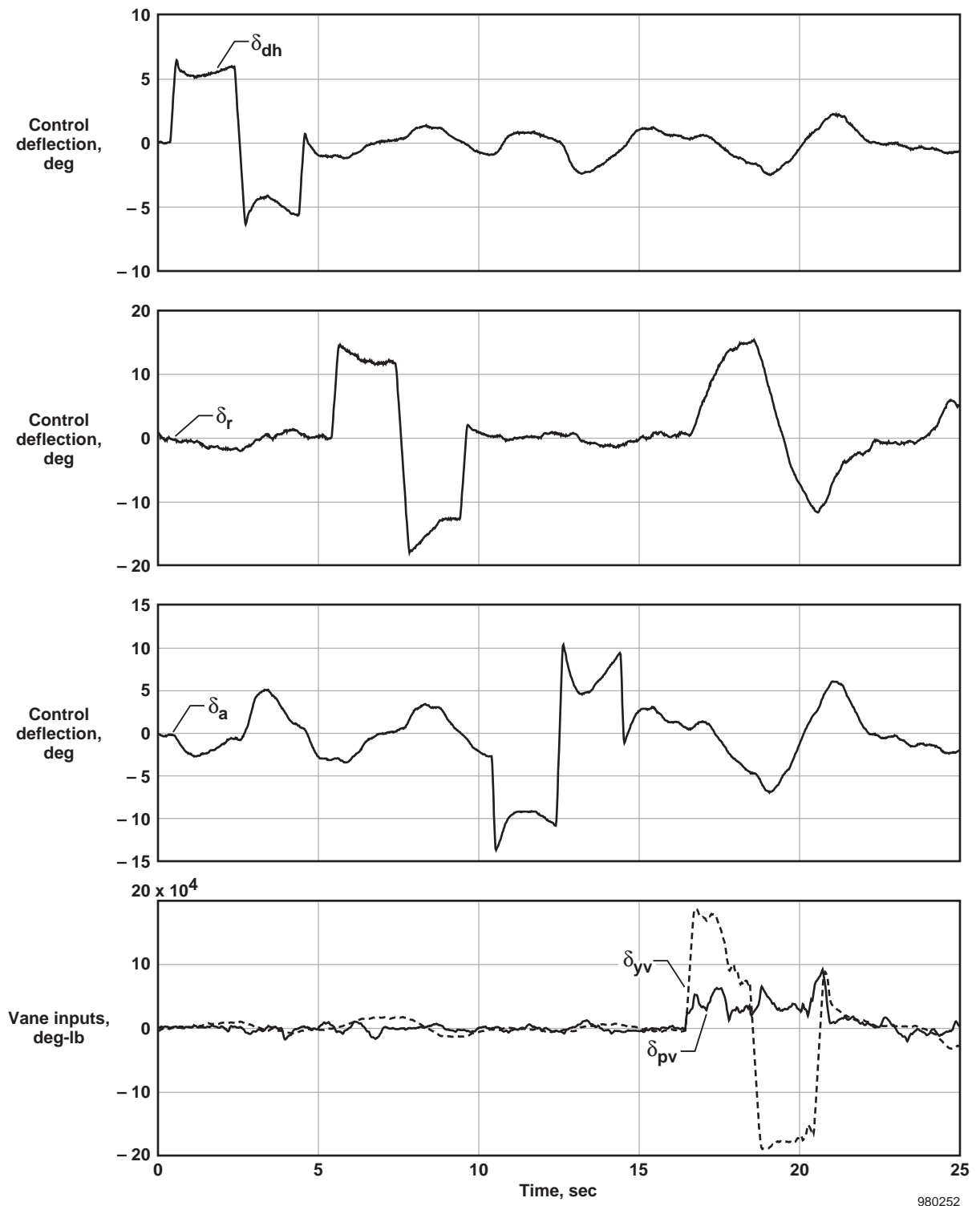


(a) Flight condition.

Figure 7. Time history data from a typical 30° AOA lateral-directional PID maneuver.



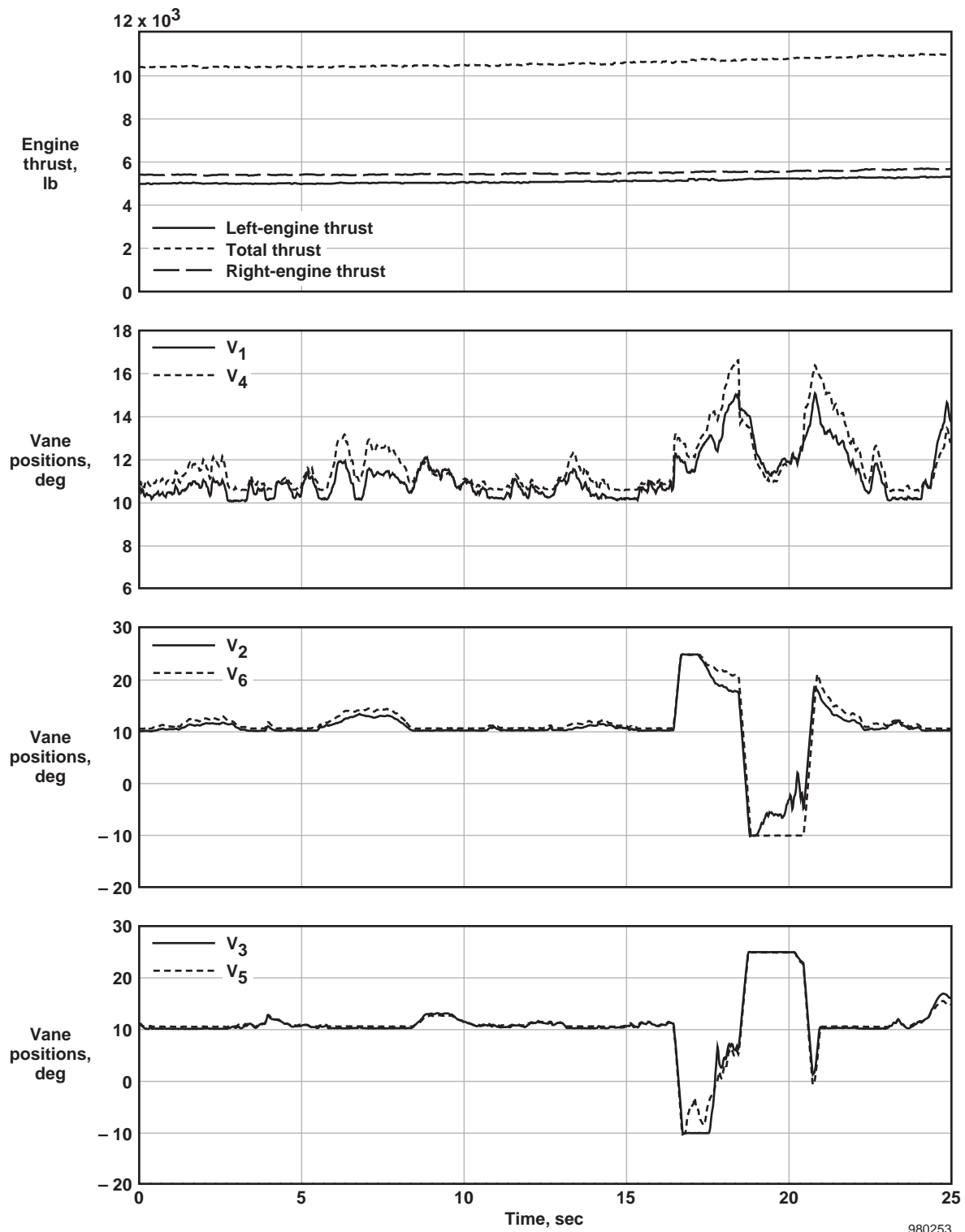
(b) Vehicle response variables.  
Figure 7. Continued.



980252

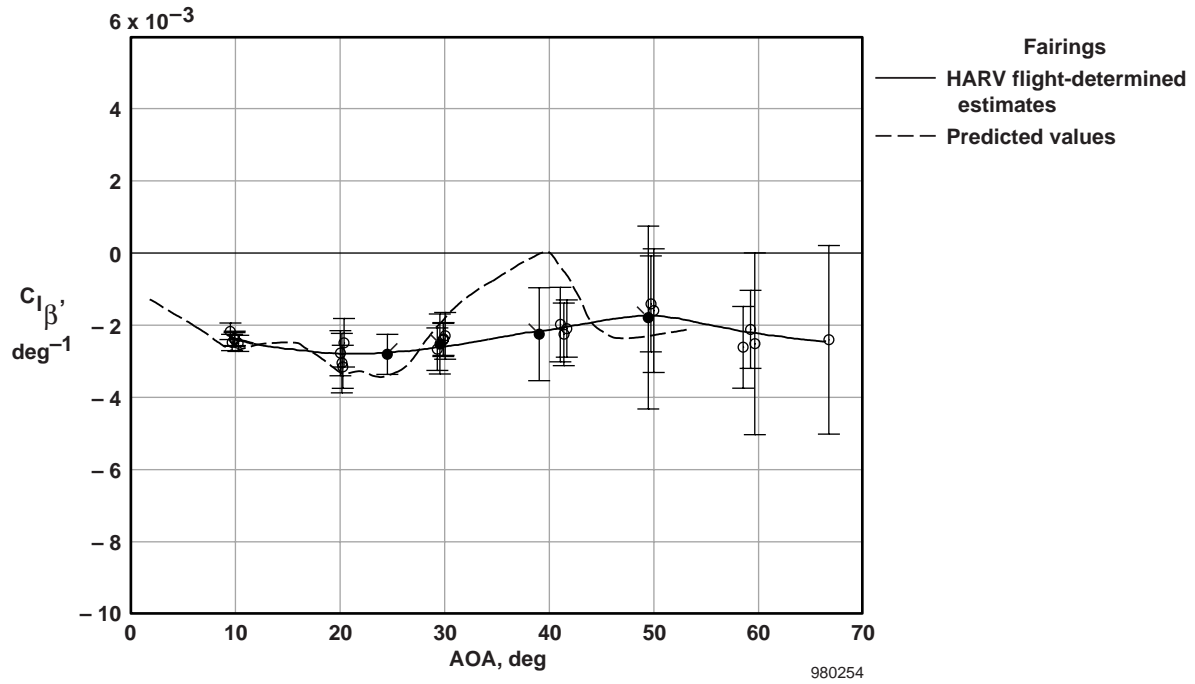
(c) Control (input) variables.

Figure 7. Continued.

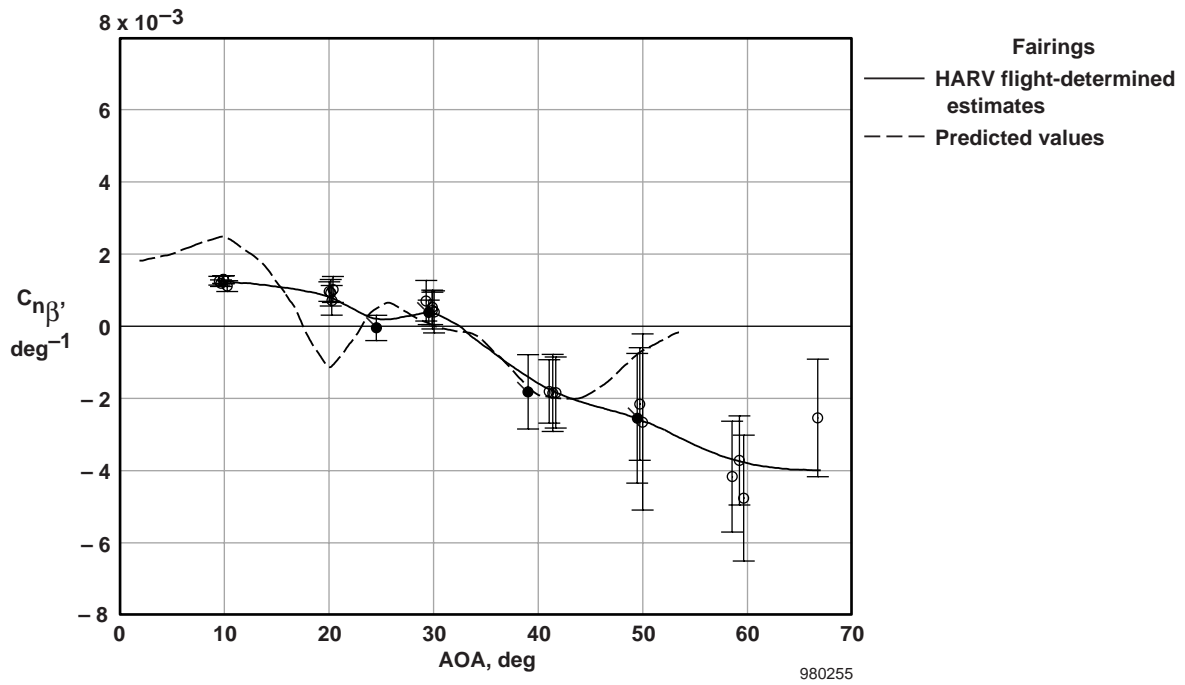


(d) Engine thrust and vane positions.

Figure 7. Concluded.

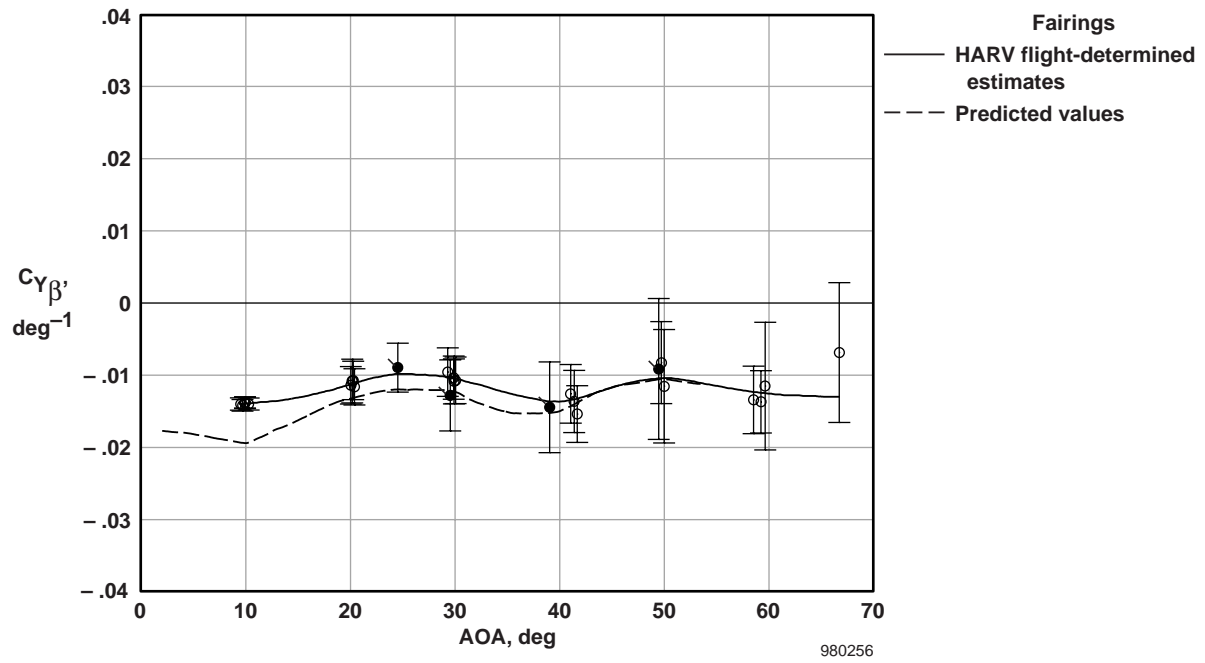


(a)  $C_{l_{\beta}}$  as a function of AOA.

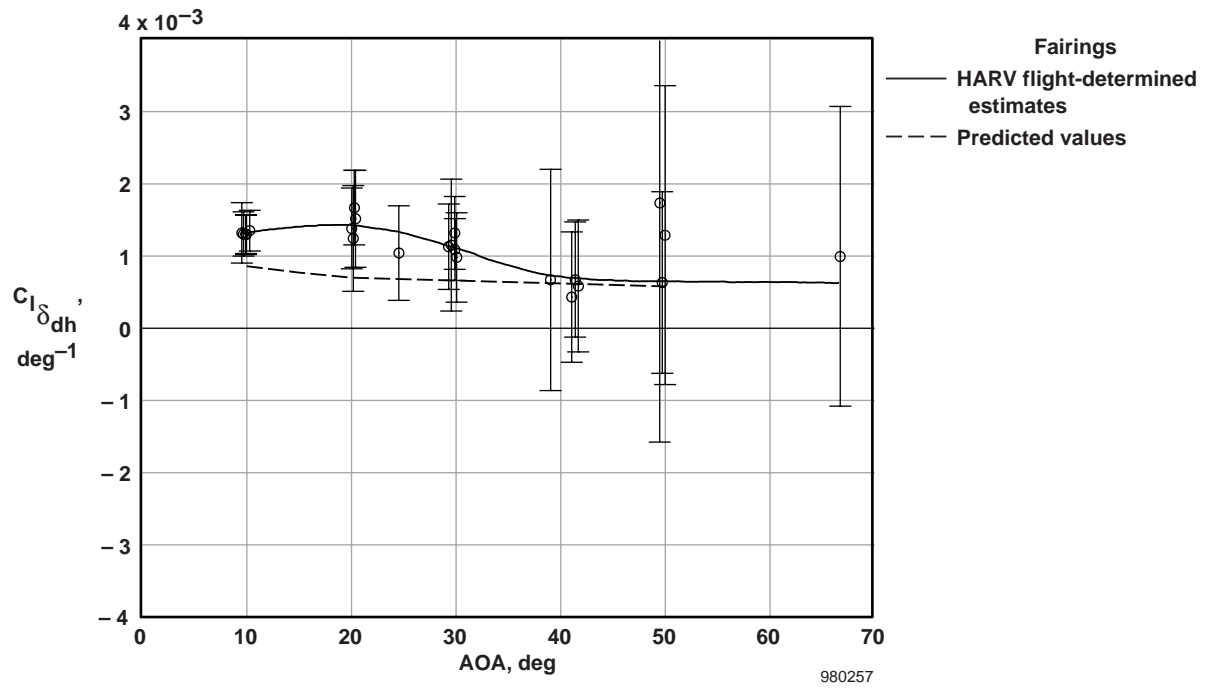


(b)  $C_{n_{\beta}}$  as a function of AOA.

Figure 8. HARV sideslip derivatives as functions of AOA.

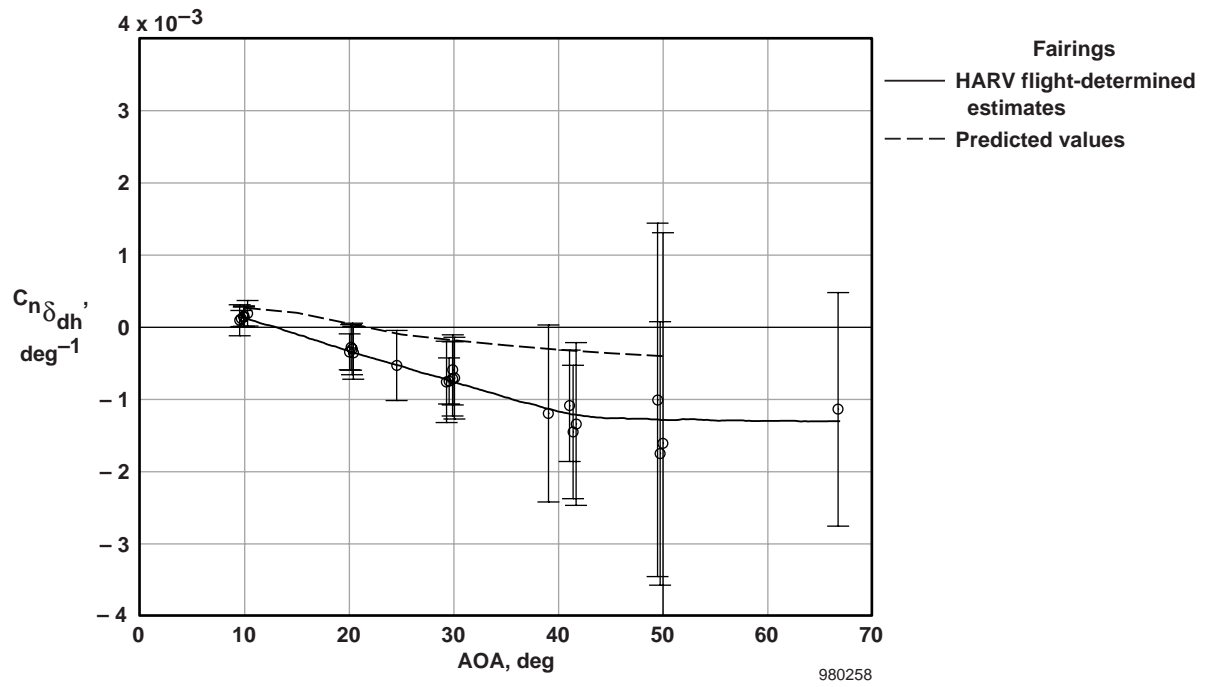


(c)  $C_{Y\beta}$  as a function of AOA.  
 Figure 8. Concluded.

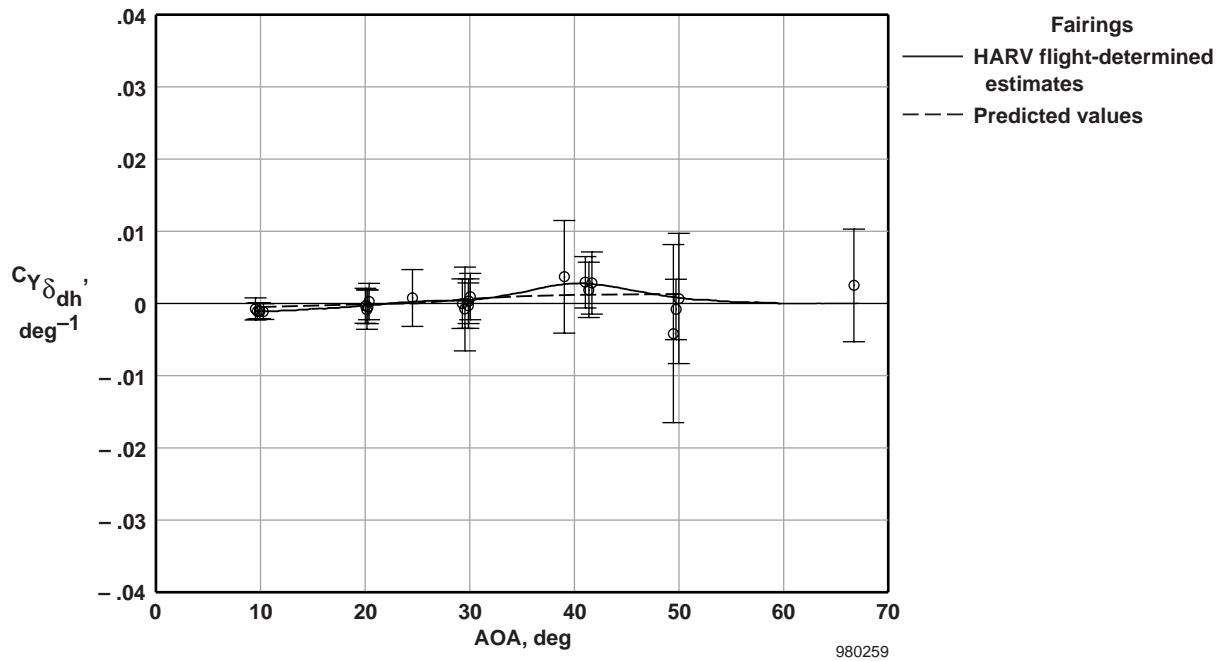


(a)  $C_{l_{\delta_{dh}}}$  as a function of AOA.

Figure 9. HARV differential horizontal stabilator derivatives as functions of AOA.



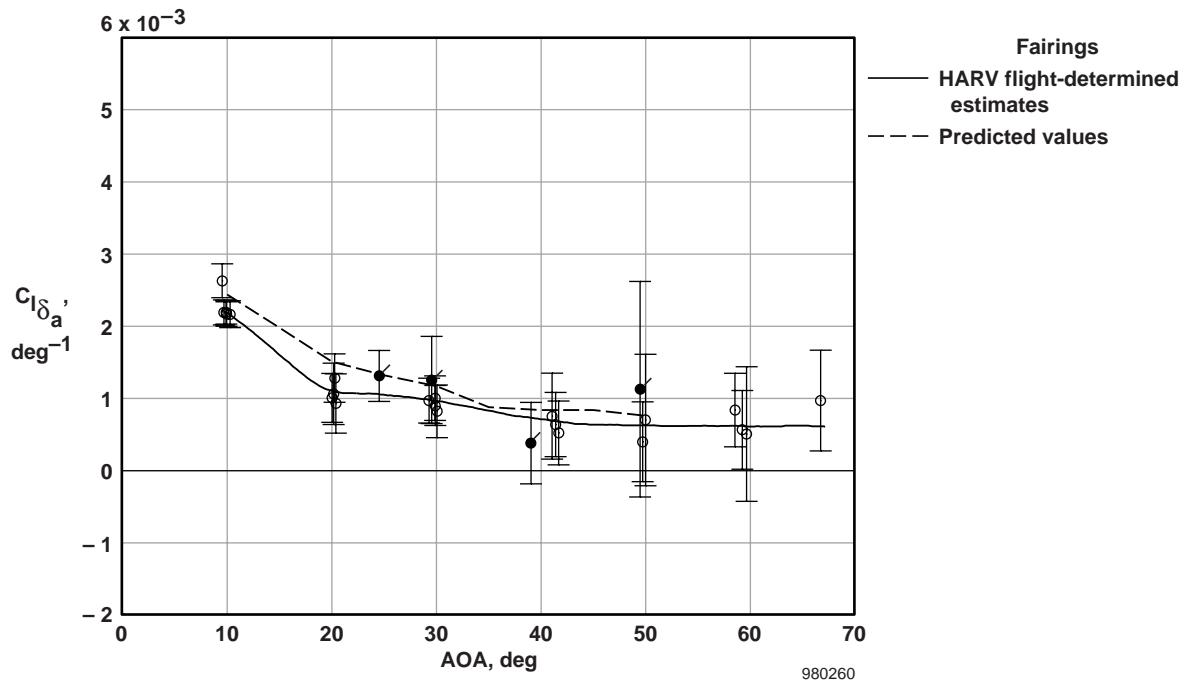
(b)  $C_{n\delta_{dh}}$  as a function of AOA.



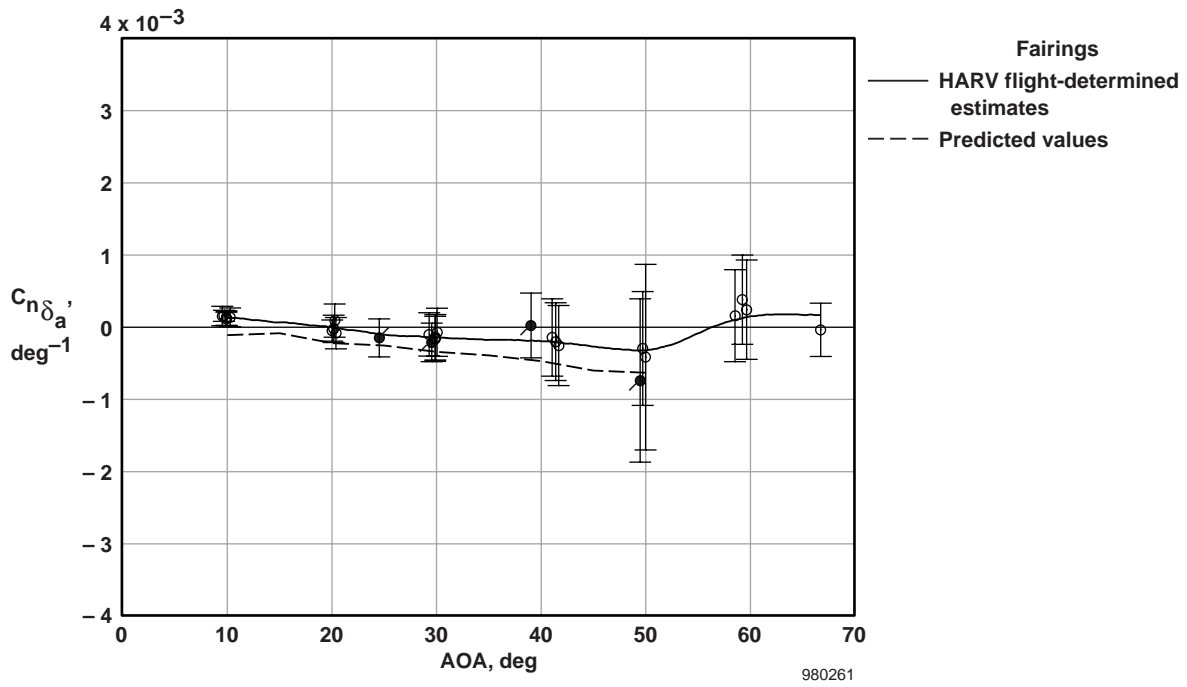
(c)  $C_{Y\delta_{dh}}$  as a function of AOA.

Figure 9. Concluded.



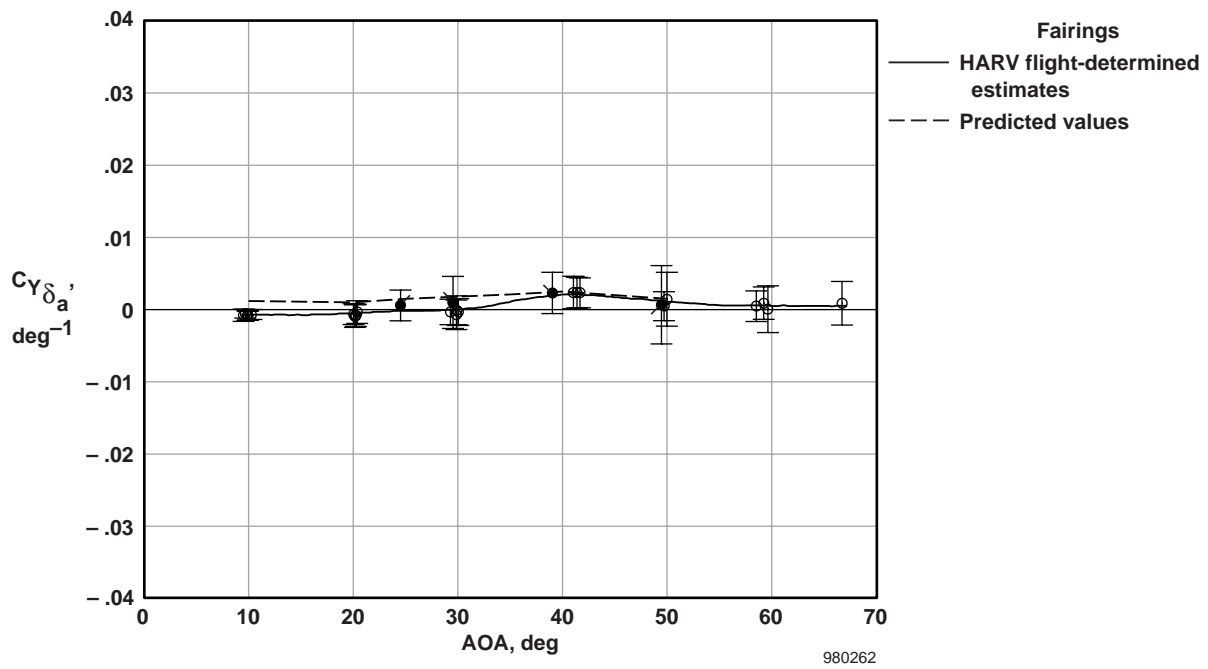


(a)  $C_{l_{\delta_a}}$  as a function of AOA.



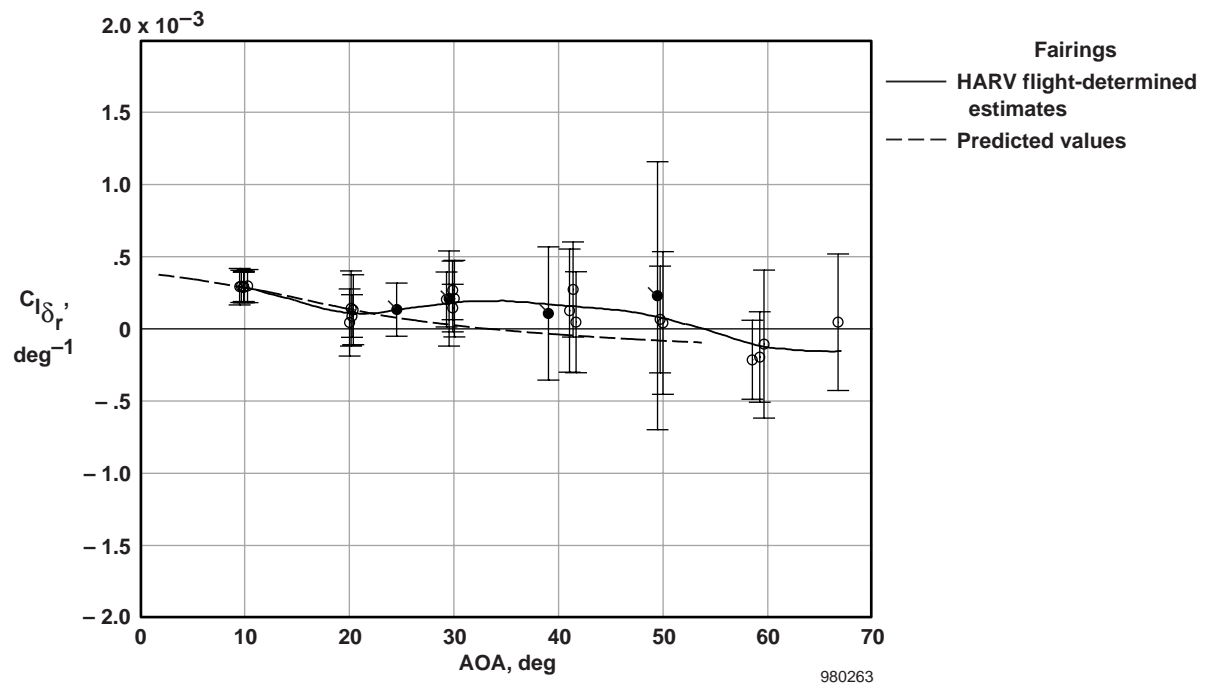
(b)  $C_{n_{\delta_a}}$  as a function of AOA.

Figure 10. HARV aileron derivatives as functions of AOA.



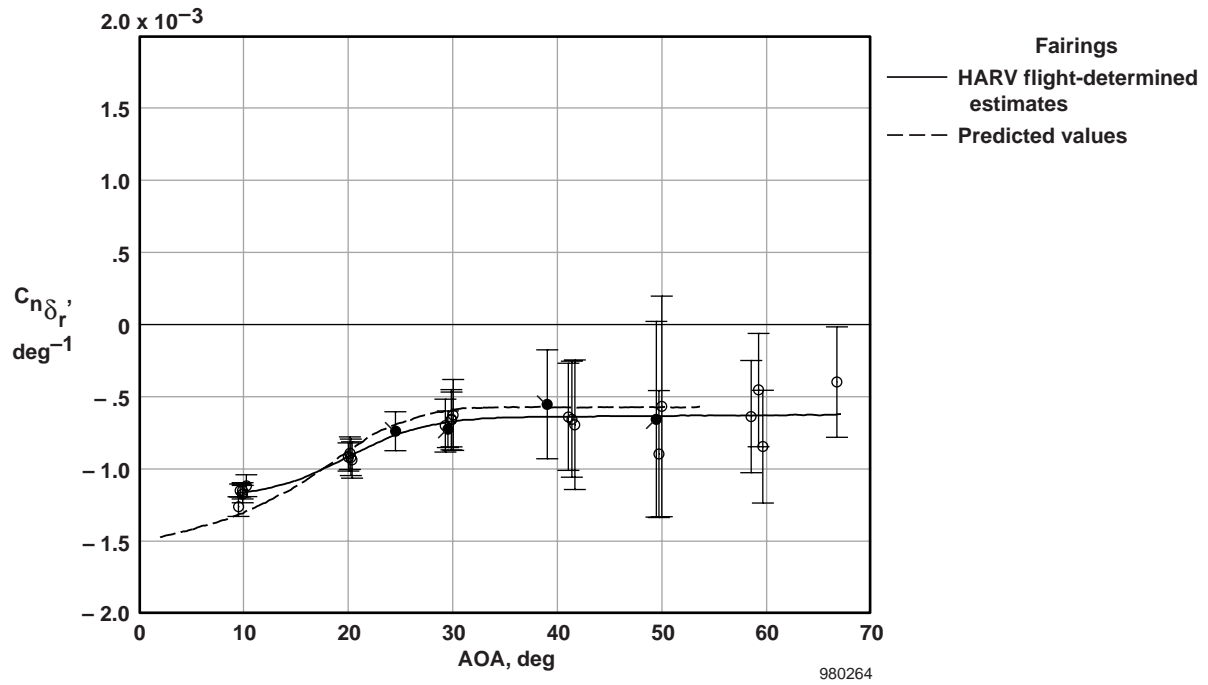
(c)  $C_{Y_{\delta_a}}$  as a function of AOA.

Figure 10. Concluded.

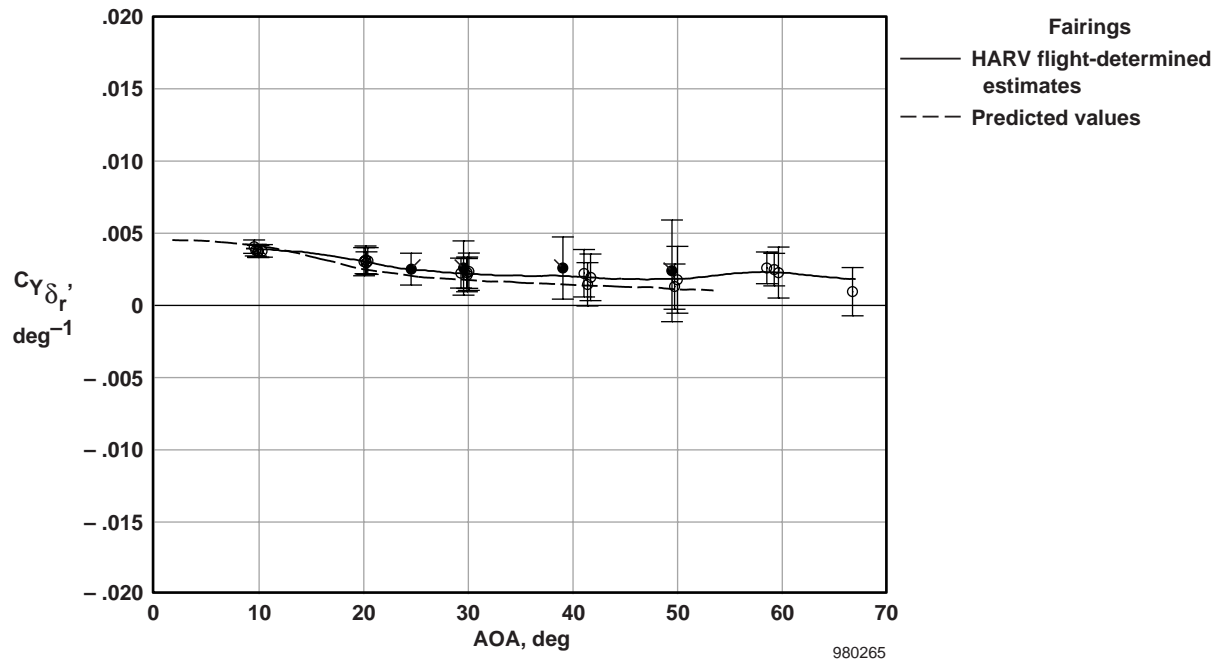


(a)  $C_{l_{\delta_r}}$  as a function of AOA.

Figure 11. HARV rudder derivatives as functions of AOA.

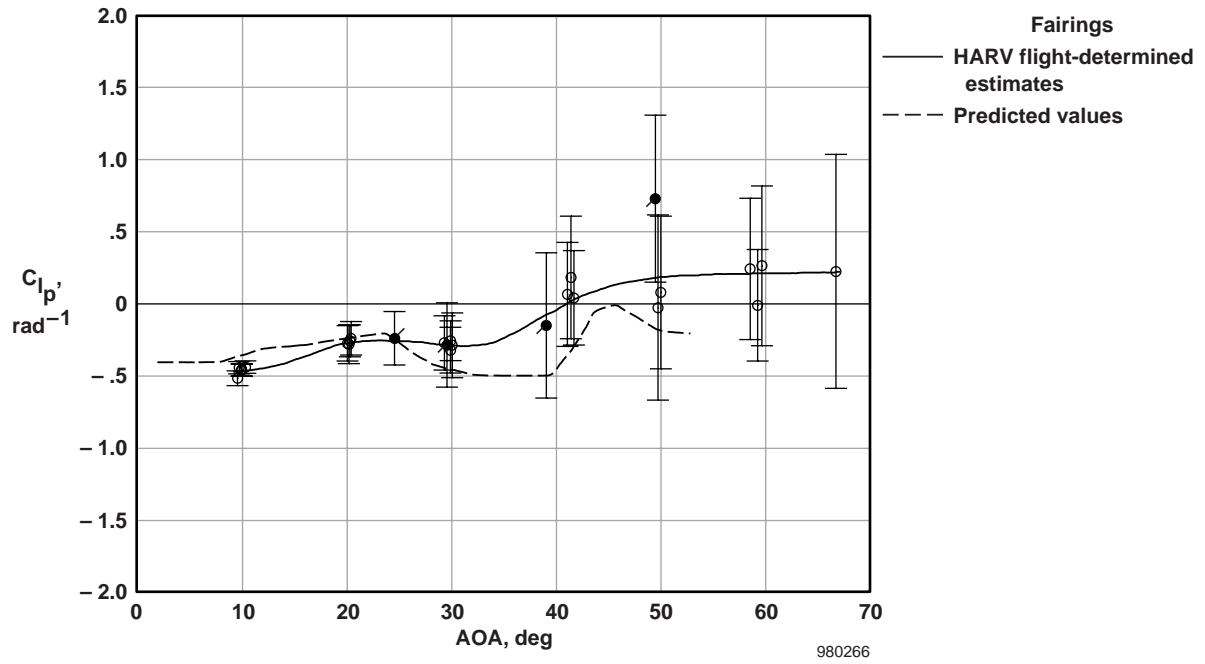


(b)  $C_{n_{\delta_r}}$  as a function of AOA.

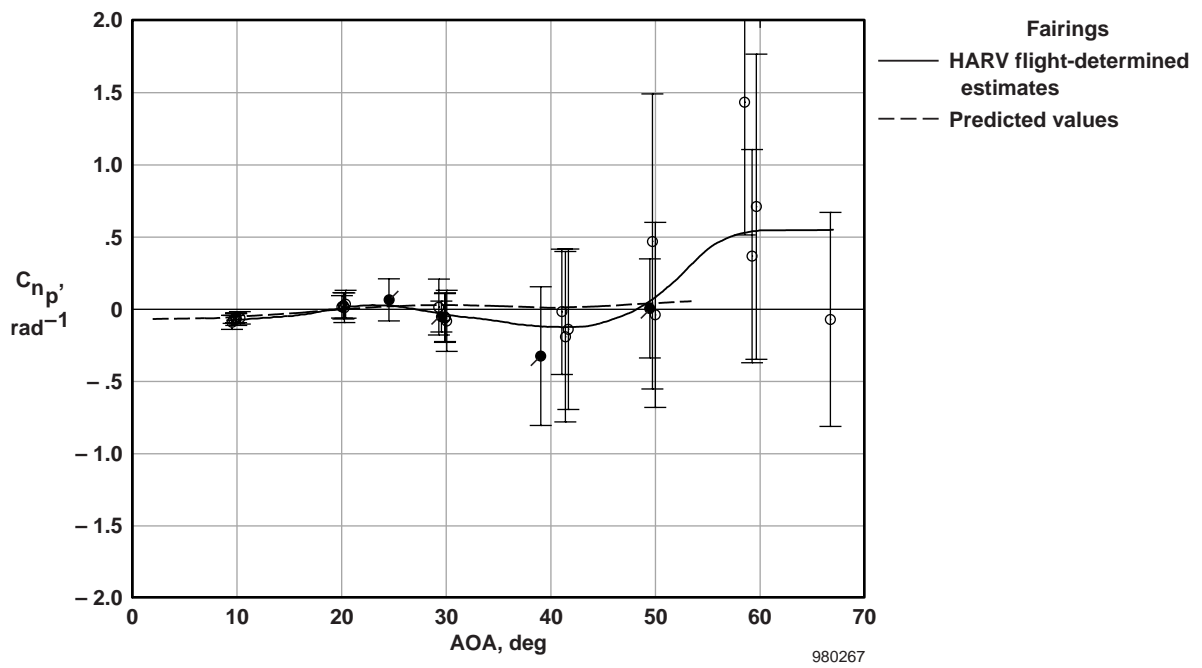


(c)  $C_{Y_{\delta_r}}$  as a function of AOA.

Figure 11. Concluded.

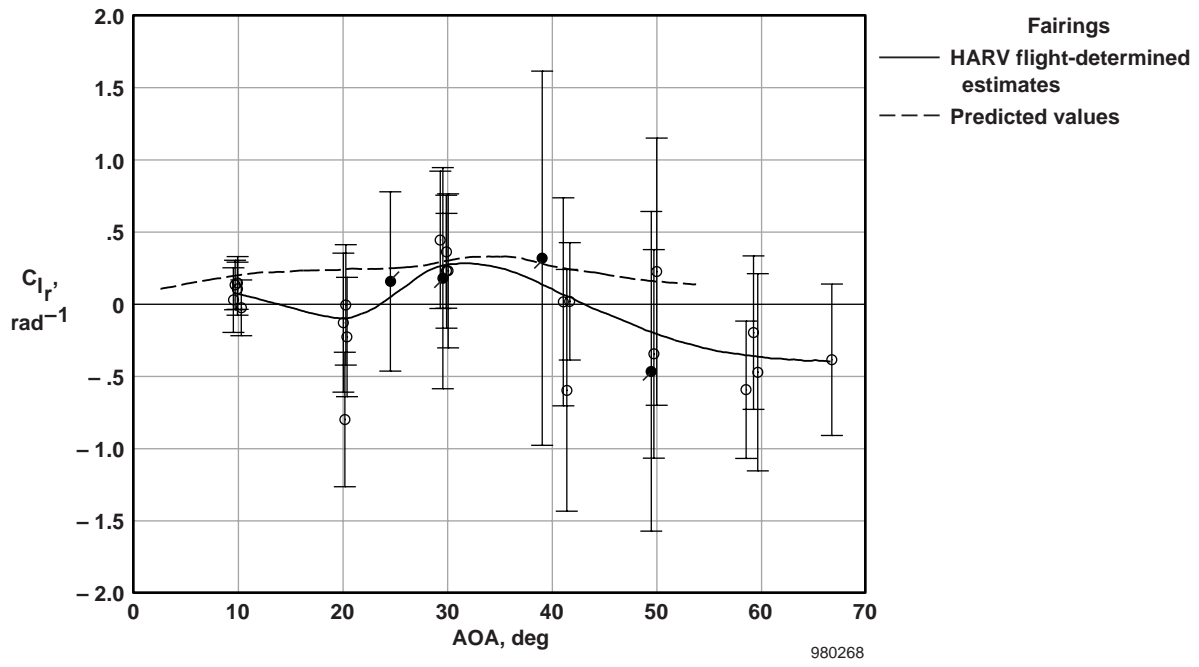


(a)  $C_{l_p}$  as a function of AOA.

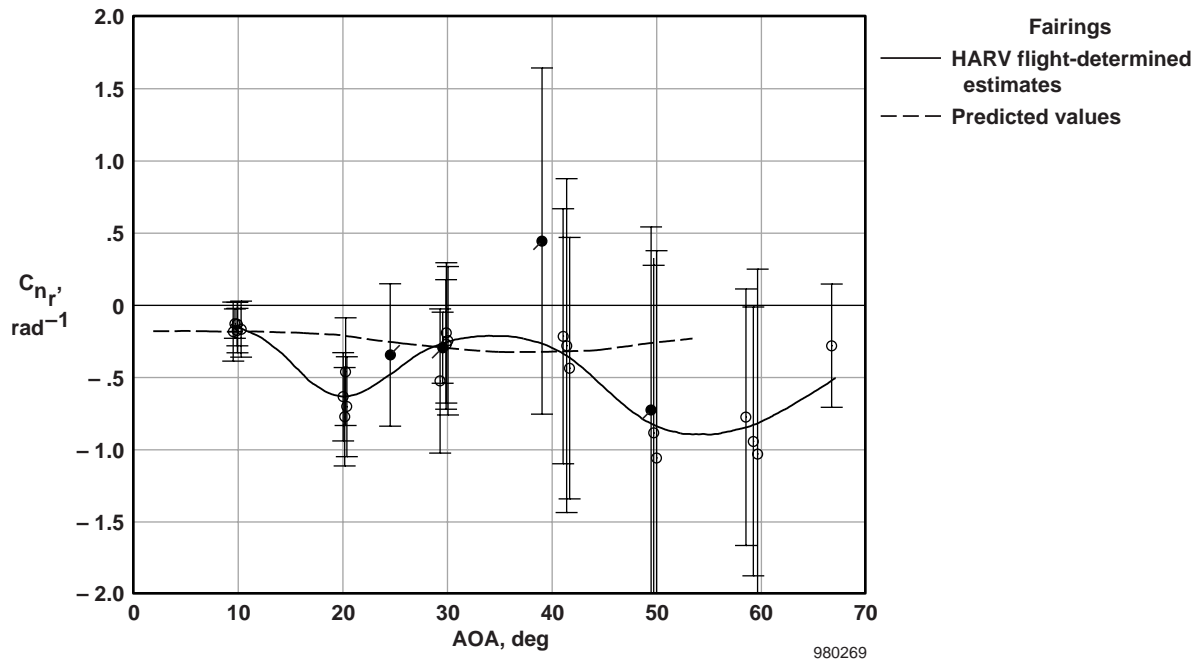


(b)  $C_{n_p}$  as a function of AOA.

Figure 12. HARV rotary derivatives as functions of AOA.

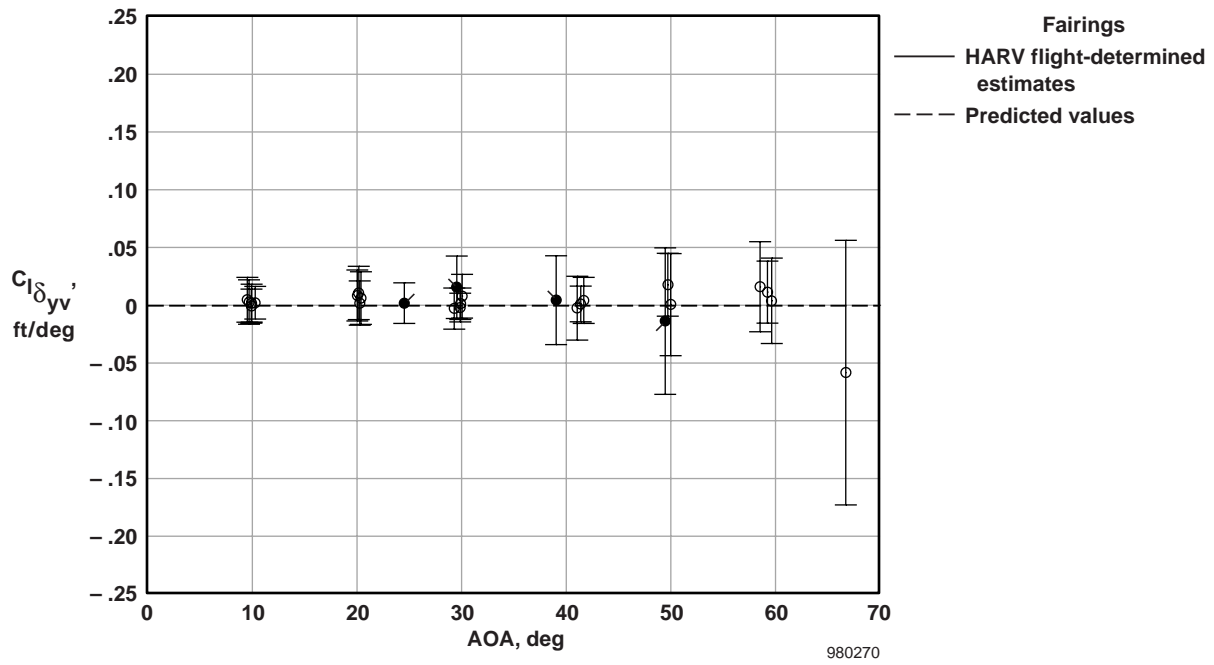


(c)  $C_{l_r}$  as a function of AOA.

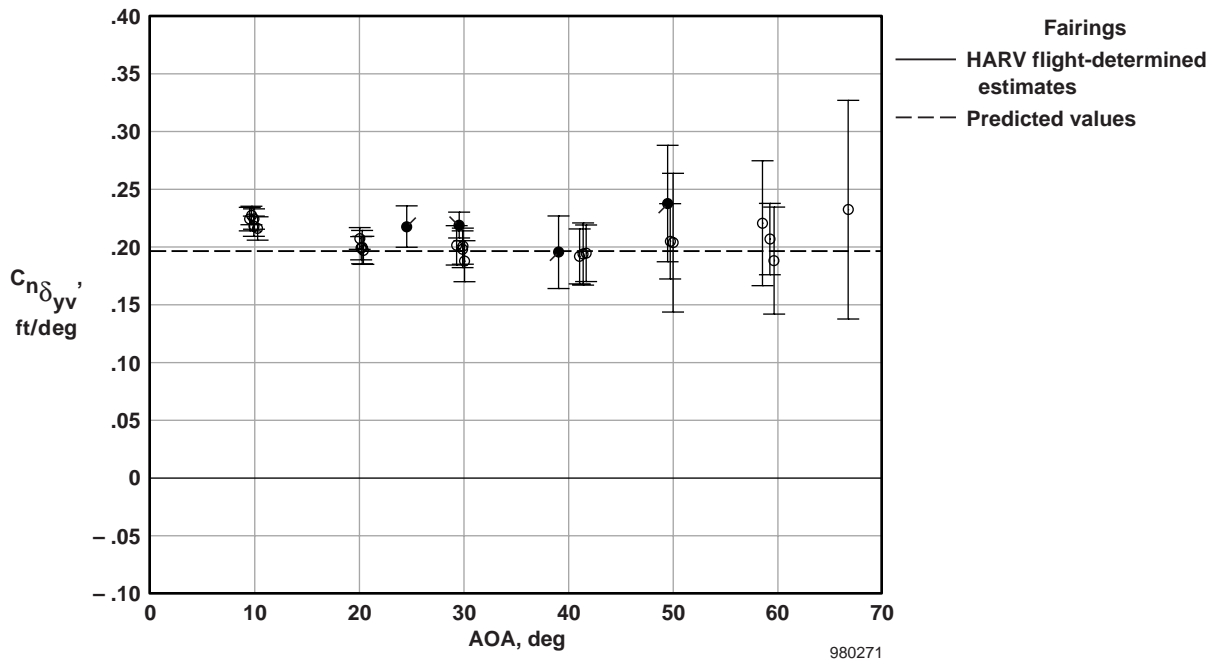


(d)  $C_{n_r}$  as a function of AOA.

Figure 12. Concluded.

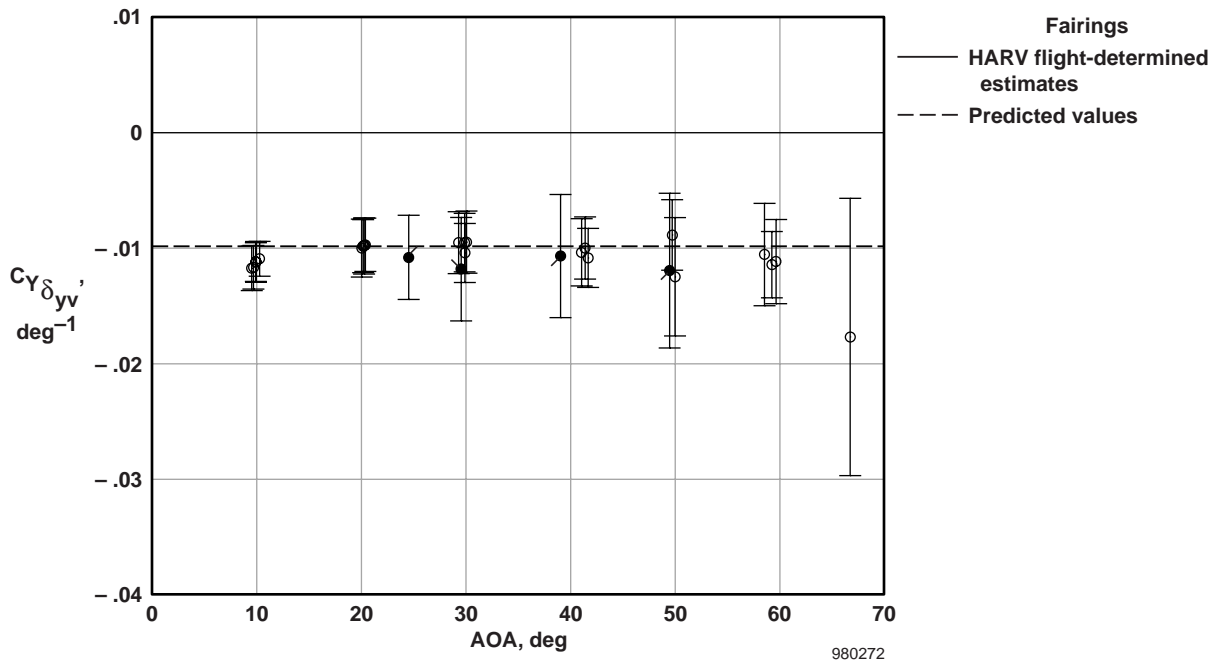


(a)  $C_{l_{\delta_{yv}}}$  as a function of AOA.



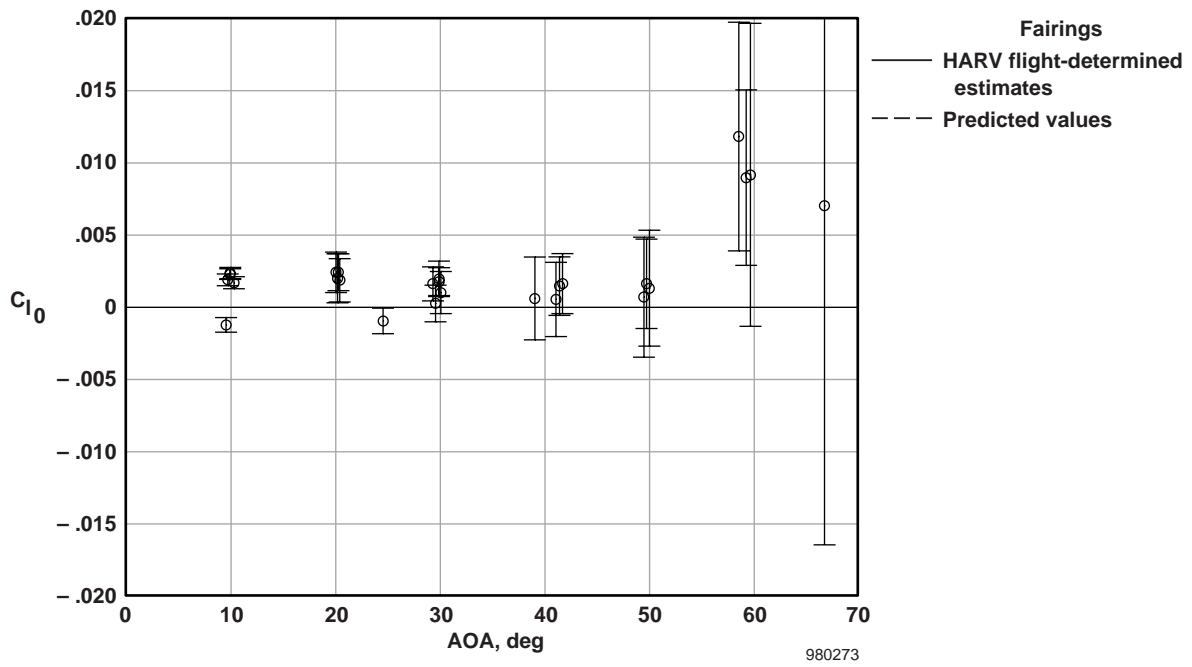
(b)  $C_{n_{\delta_{yv}}}$  as a function of AOA.

Figure 13. HARV thrust-vectoring derivatives as functions of AOA.



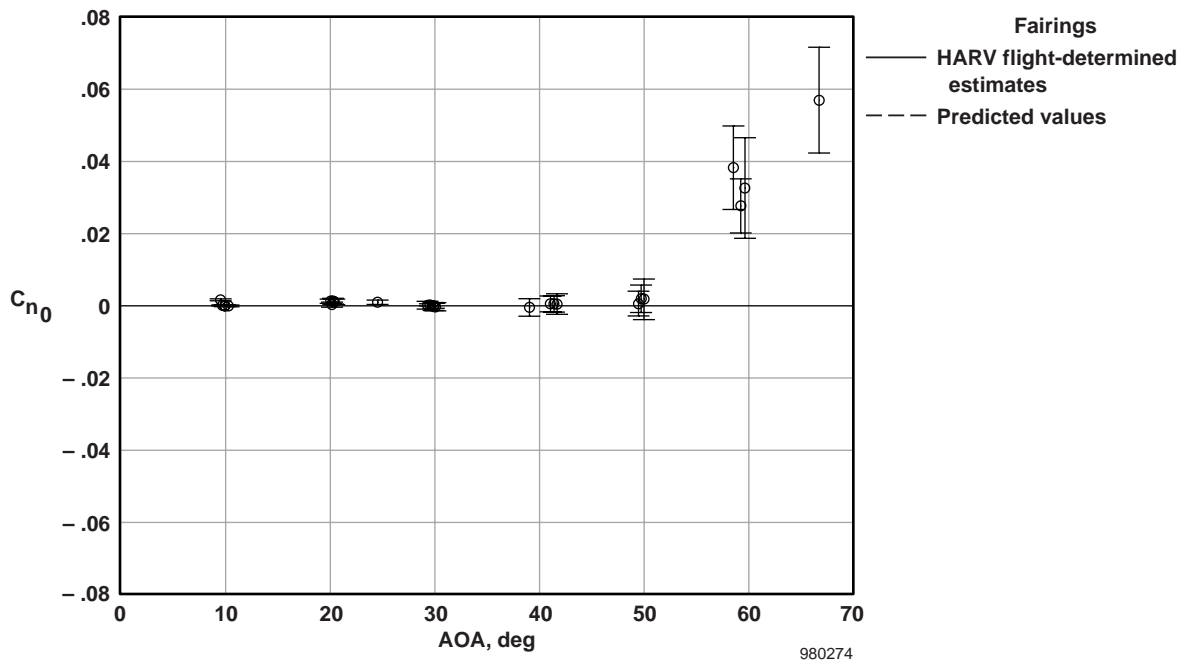
(c)  $C_{Y_{\delta_{yv}}}$  as a function of AOA.

Figure 13. Concluded.

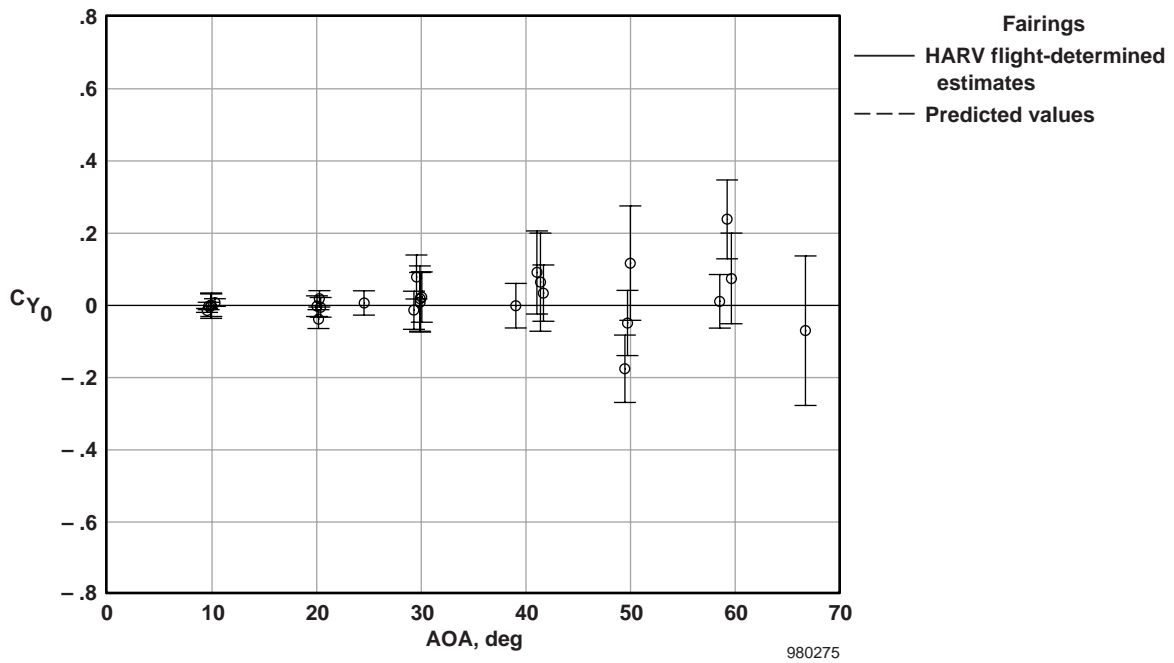


(a)  $C_{l_0}$  as a function of AOA.

Figure 14. HARV aerodynamic biases as functions of AOA.



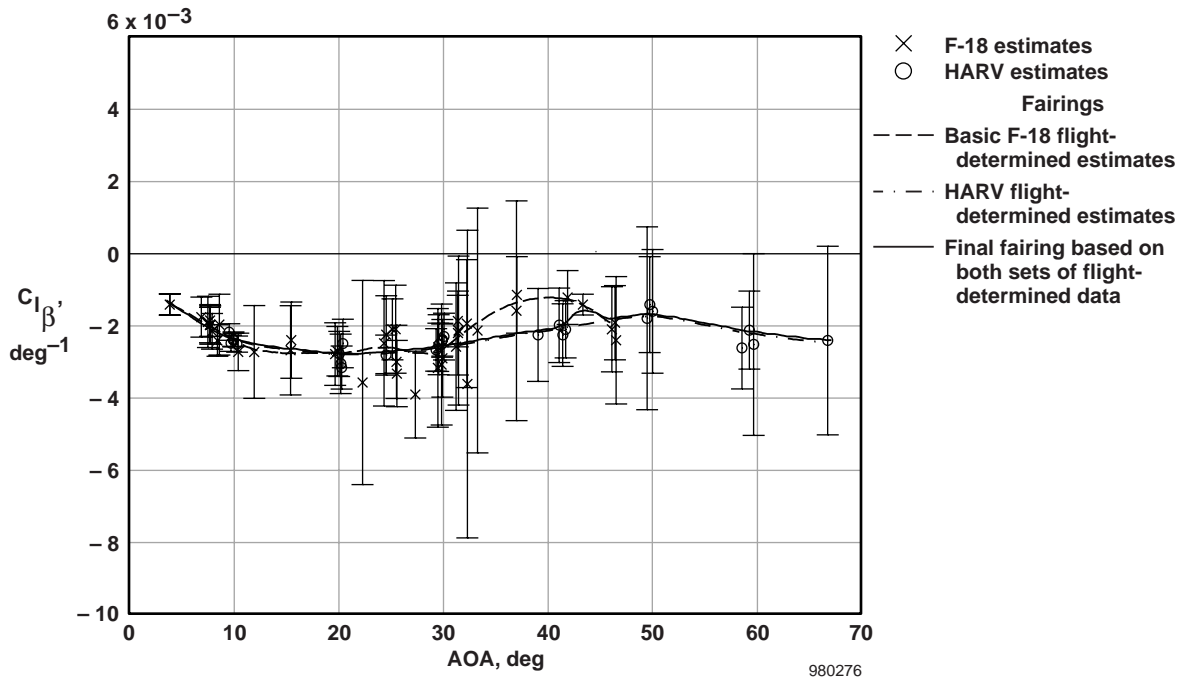
(b)  $C_{n_0}$  as a function of AOA.



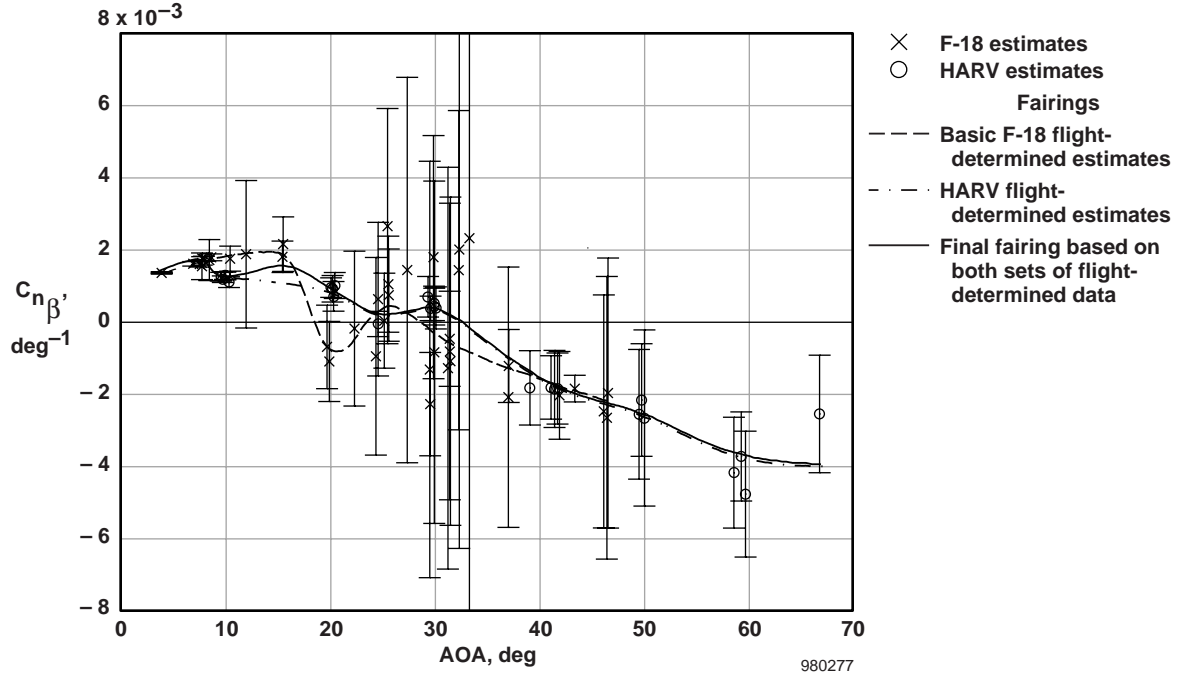
(c)  $C_{Y_0}$  as a function of AOA.

Figure 14.Concluded.



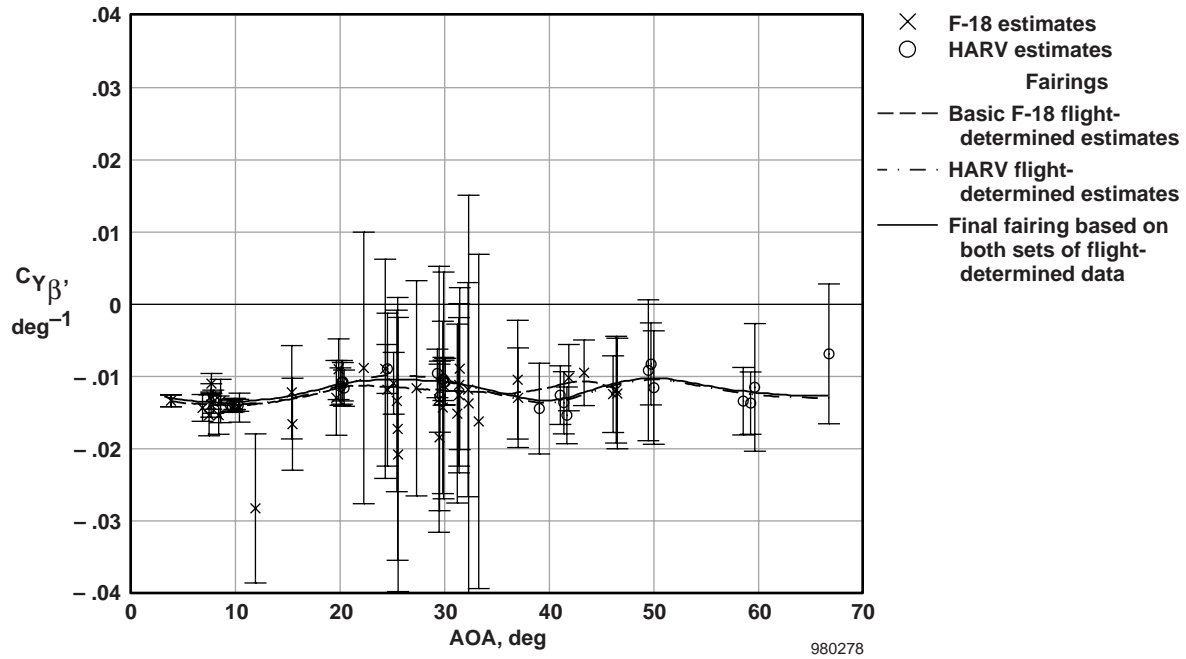


(a)  $C_{l_{\beta}}$  as a function of AOA.



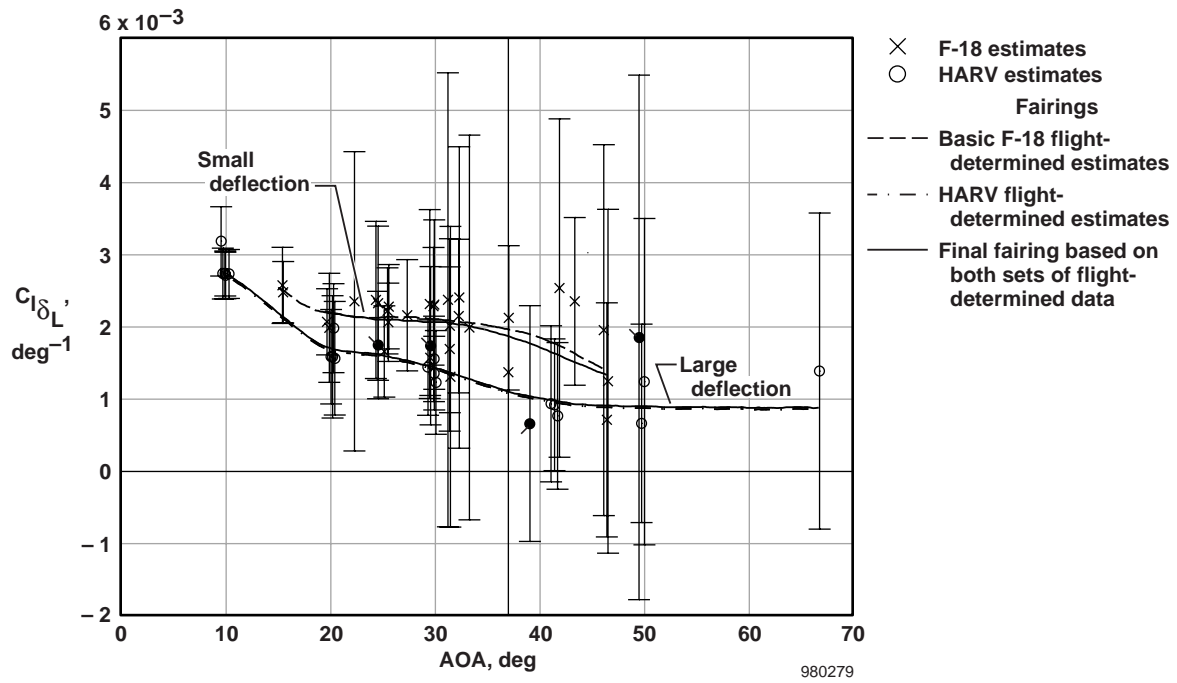
(b)  $C_{n_{\beta}}$  as a function of AOA.

Figure 15. Basic F-18 and HARV sideslip derivatives as functions of AOA.



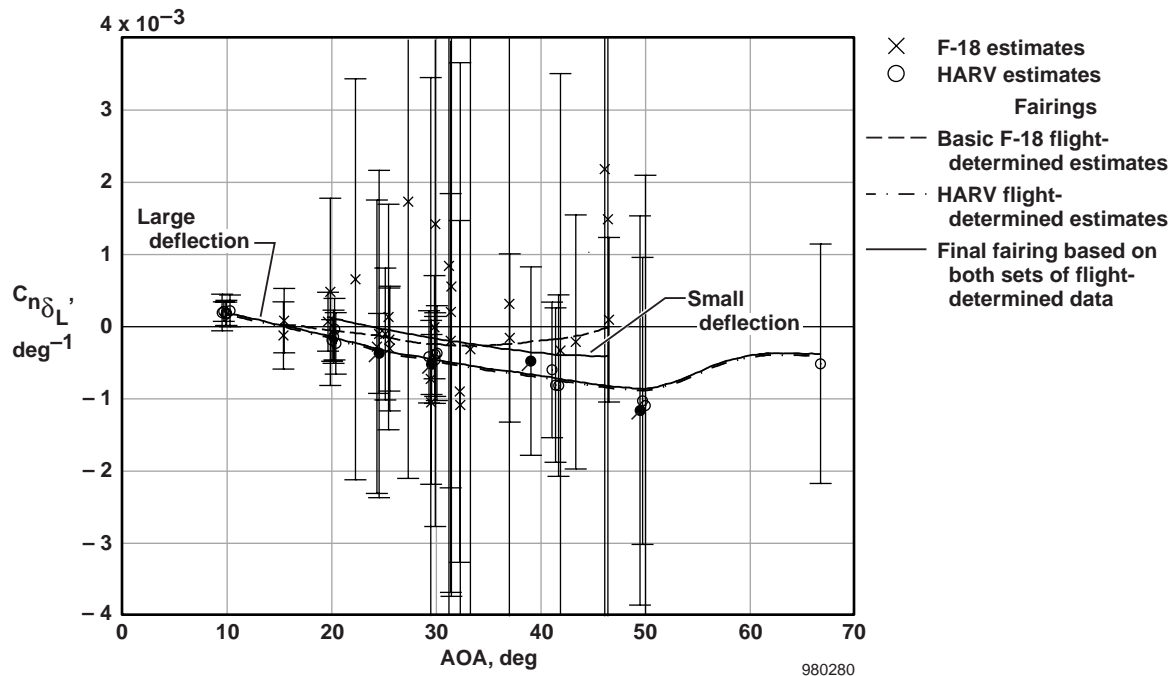
(c)  $C_{Y_{\beta}}$  as a function of AOA.

Figure 15. Concluded.

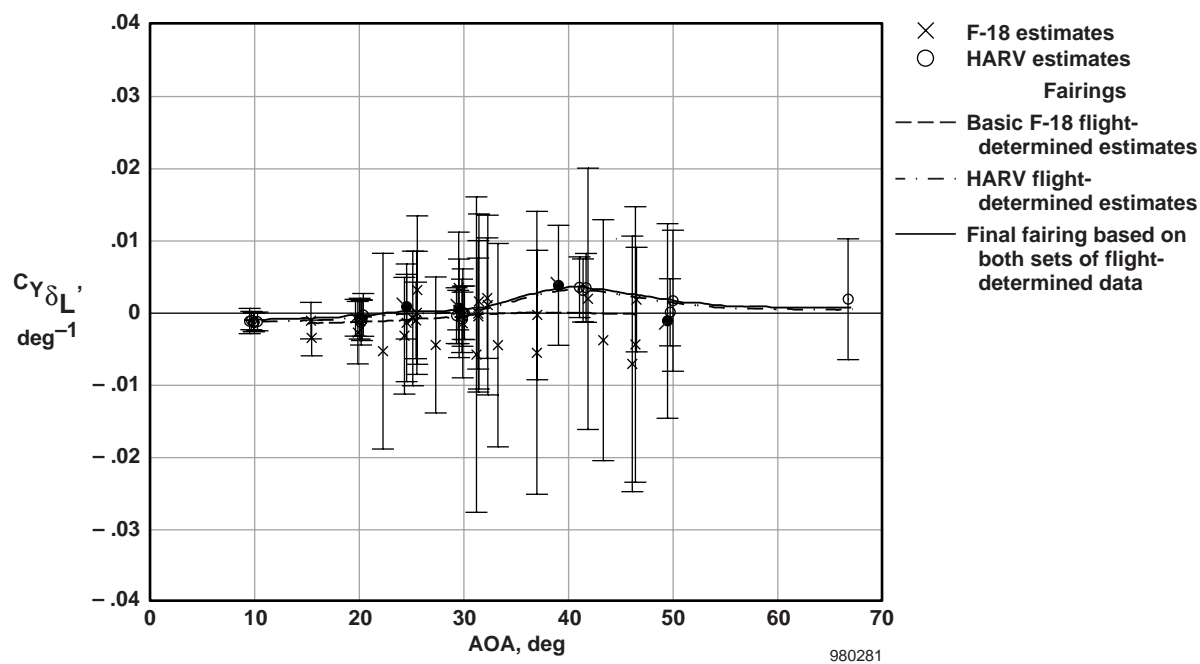


(a)  $C_{l_{\delta_L}}$  as a function of AOA.

Figure 16. Basic F-18 and HARV equivalent lateral control derivatives as functions of AOA and basic F-18 control input waveforms.

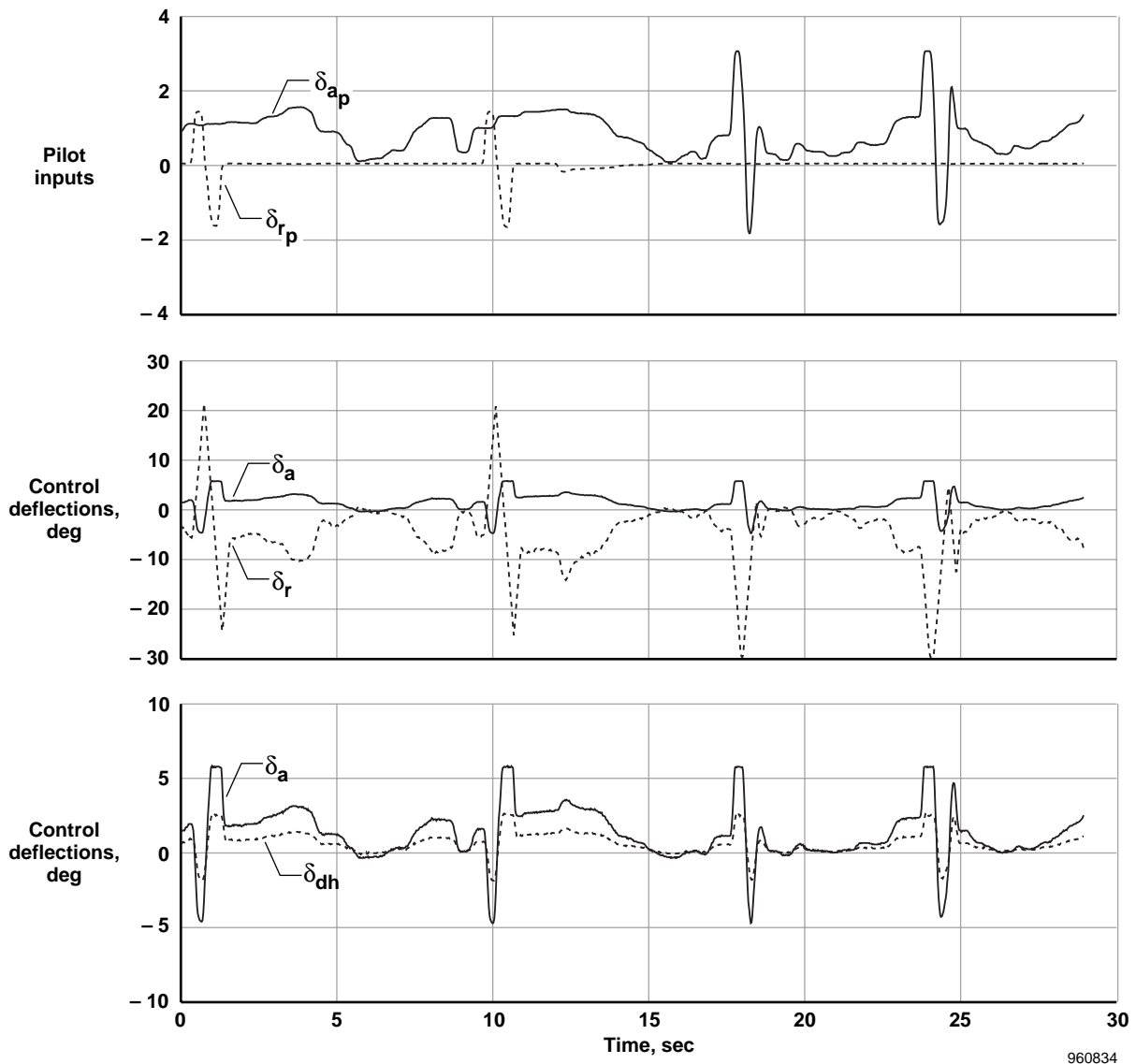


(b)  $C_{n_{\delta_L}}$  as a function of AOA.



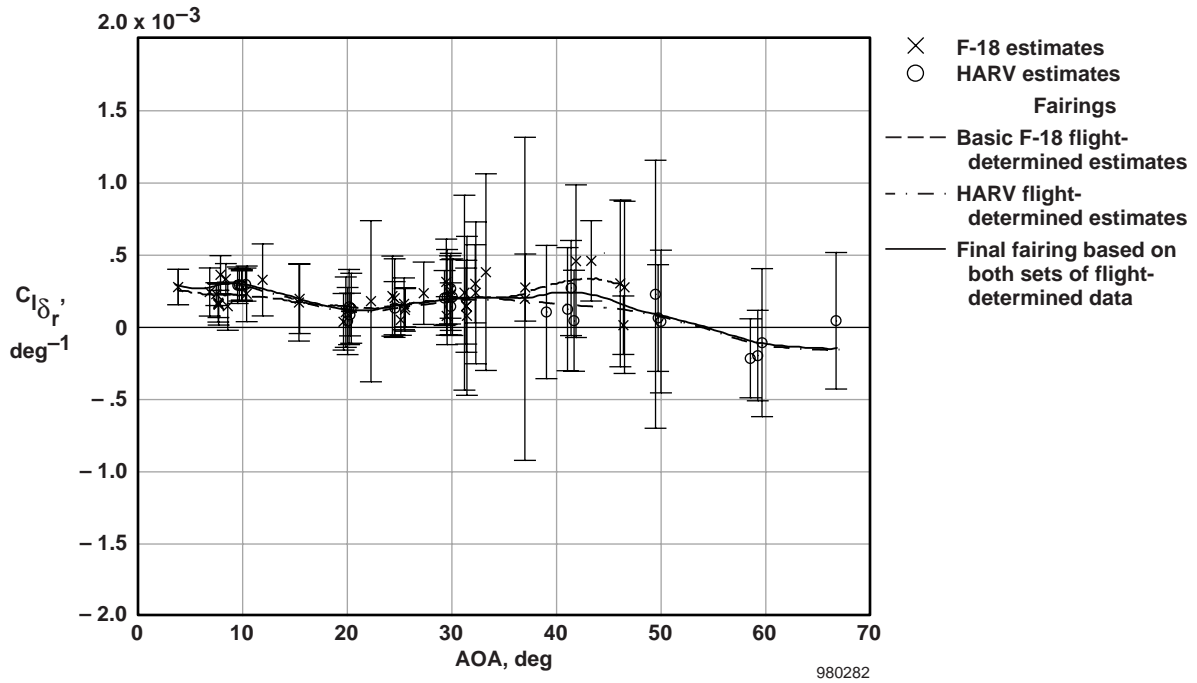
(c)  $C_{Y_{\delta_L}}$  as a function of AOA.

Figure 16. Continued.

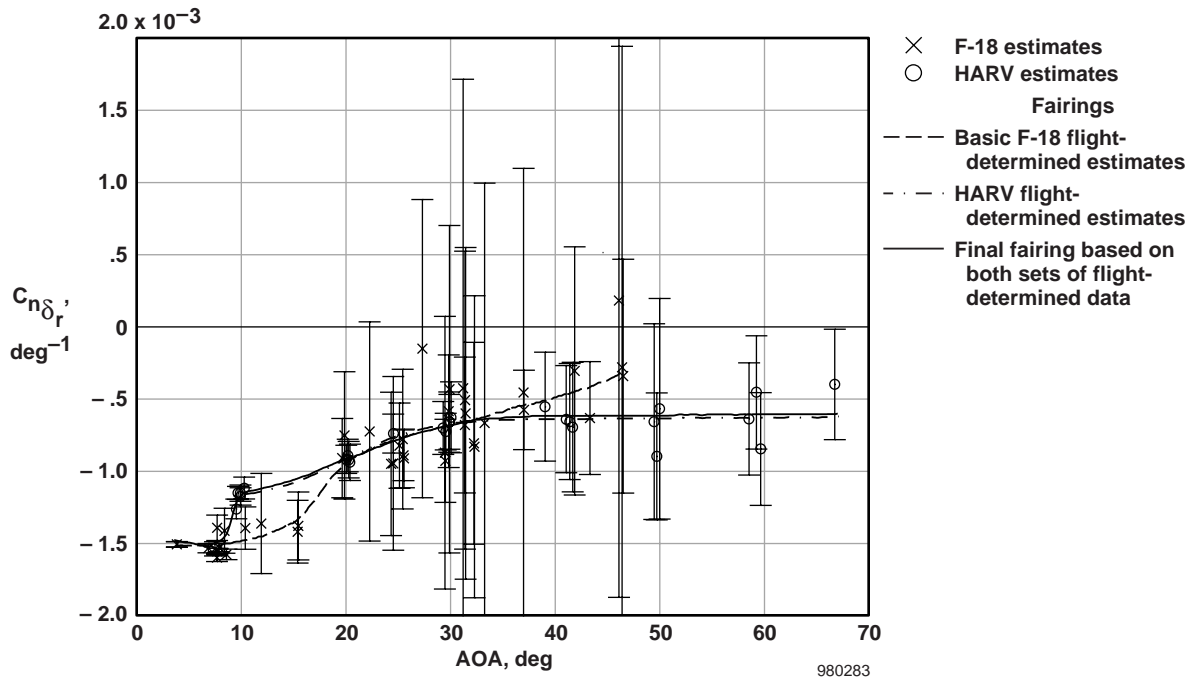


(d) Basic F-18 control input waveforms.

Figure 16. Concluded.

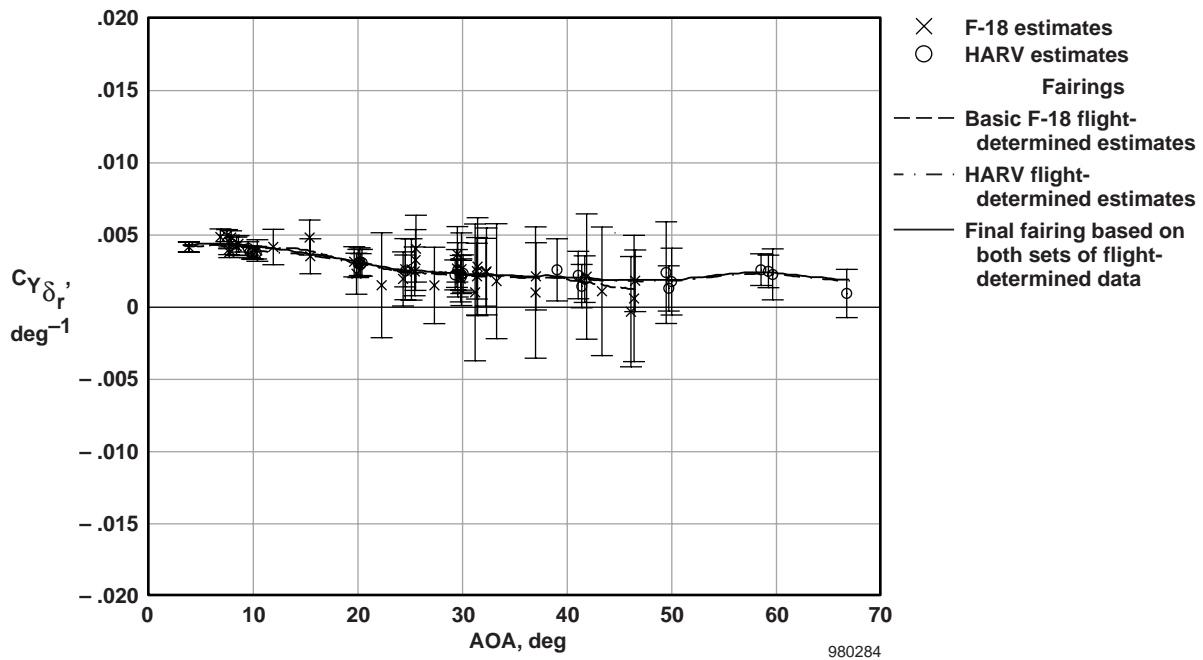


(a)  $C_{l_{\delta_r}}$  as a function of AOA.



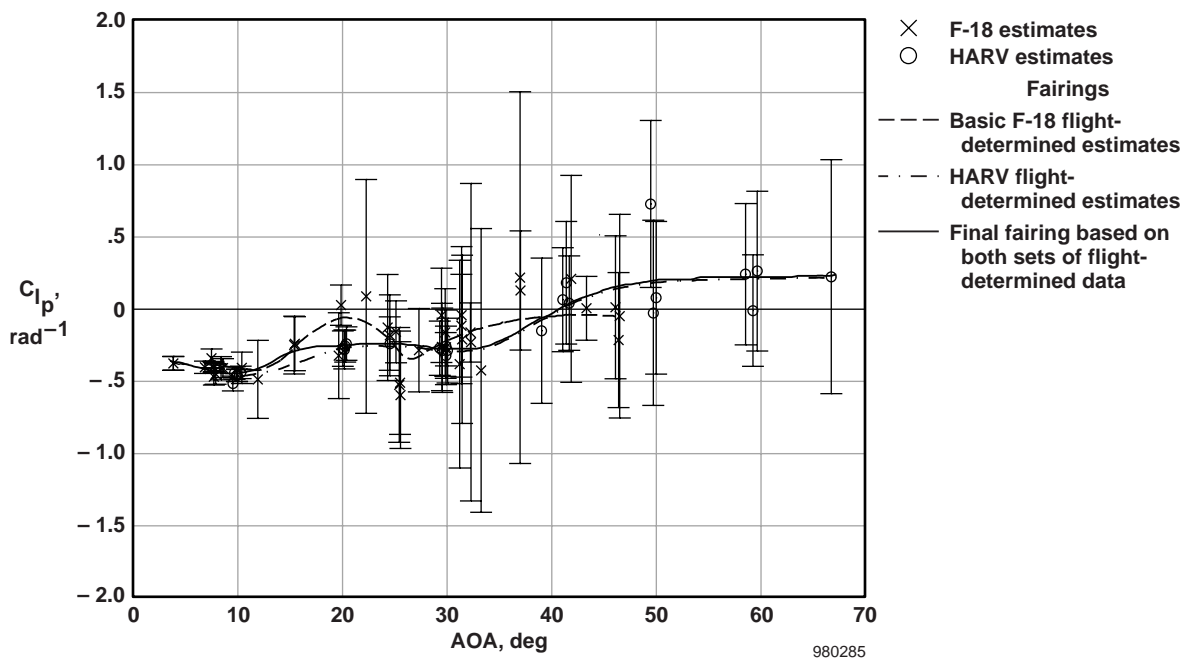
(b)  $C_{n_{\delta_r}}$  as a function of AOA.

Figure 17. Basic F-18 and HARV rudder derivatives as functions of AOA.



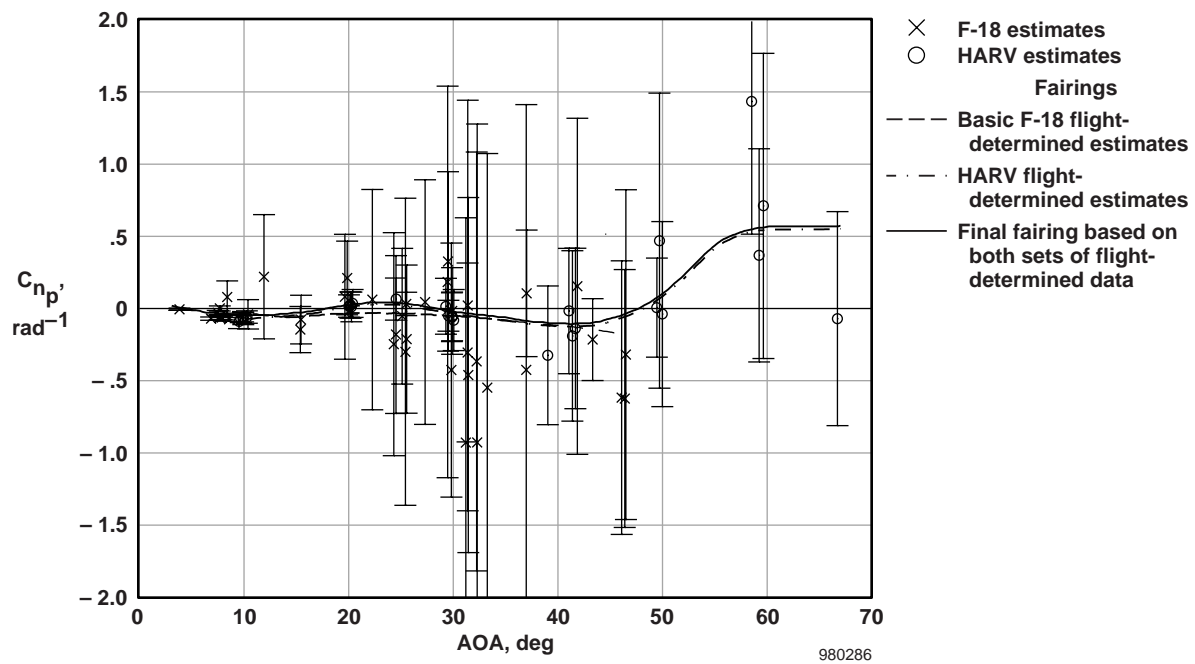
(c)  $C_{Y_{\delta_r}}$  as a function of AOA.

Figure 17. Concluded.

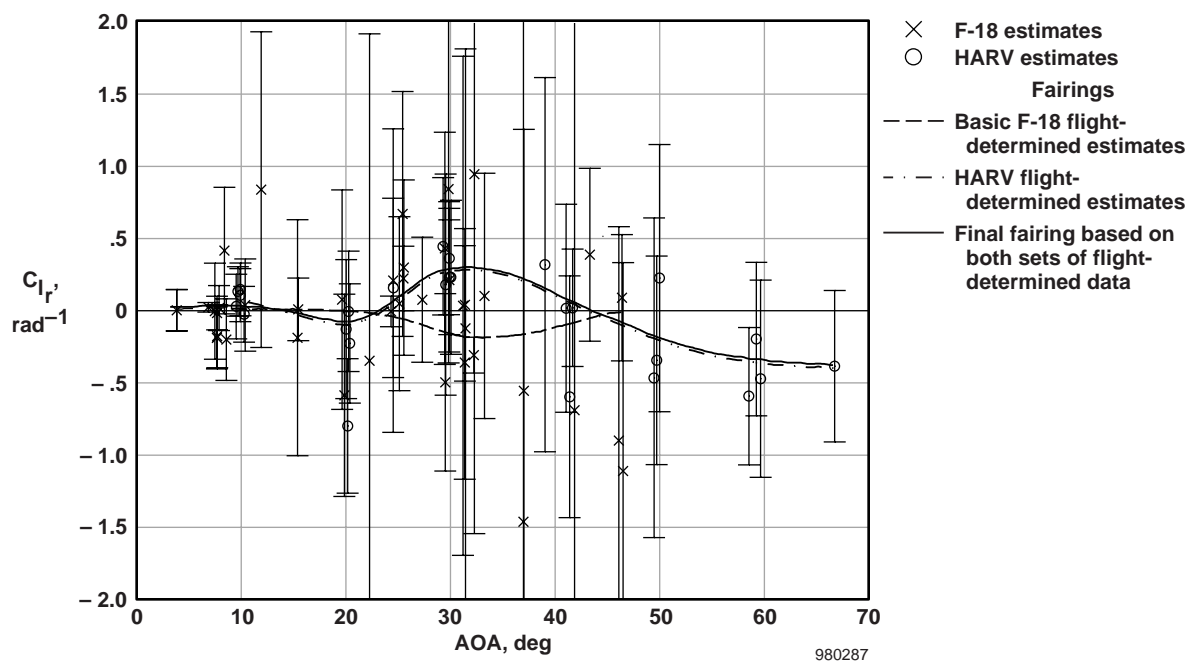


(a)  $C_{l_p}$  as a function of AOA.

Figure 18. Basic F-18 and HARV rotary derivatives as functions of AOA.

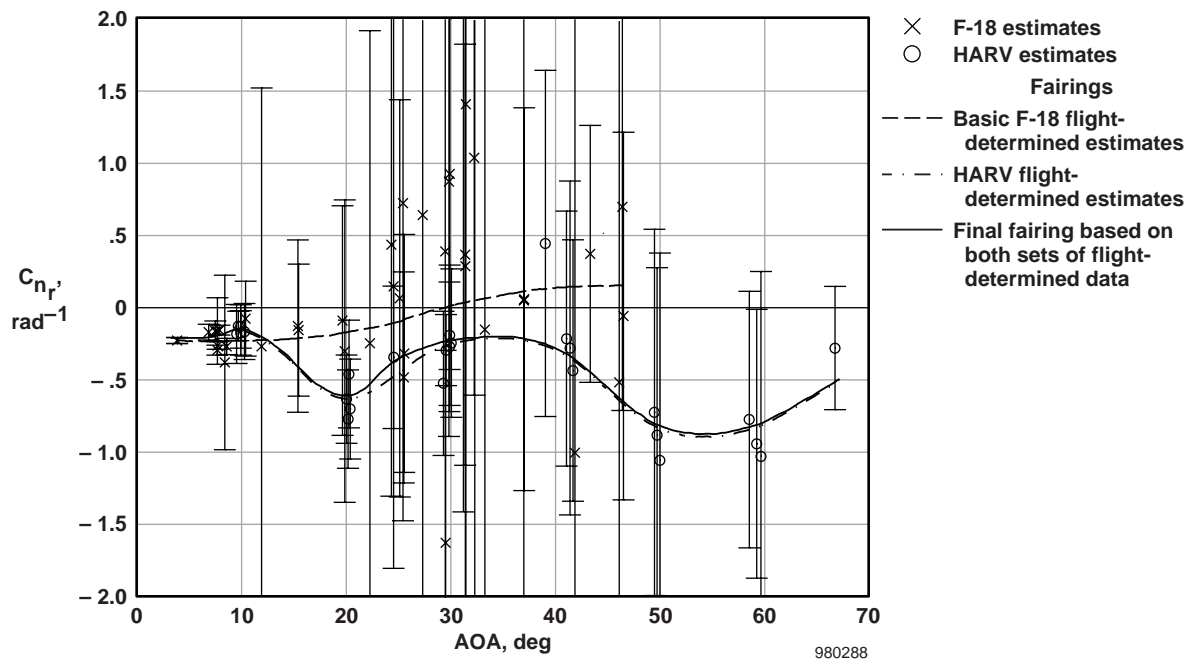


(b)  $C_{n_p'}$  as a function of AOA.



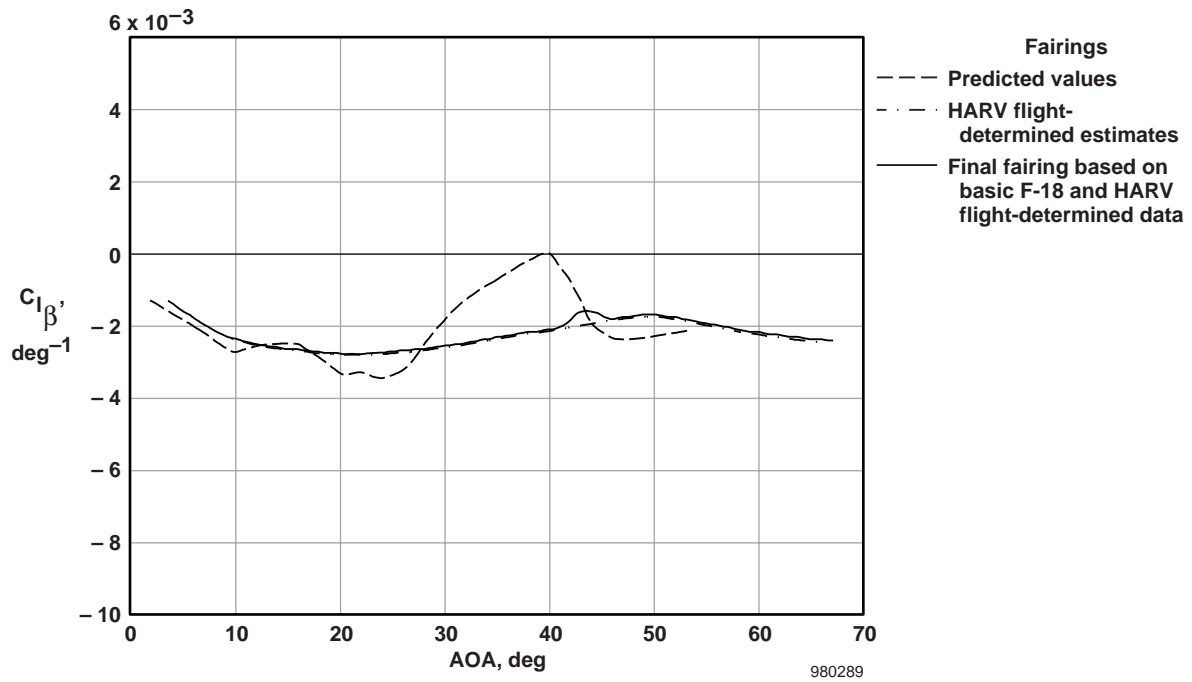
(c)  $C_{l_r'}$  as a function of AOA.

Figure 18. Continued.



(d)  $C_{n_r}$  as a function of AOA.

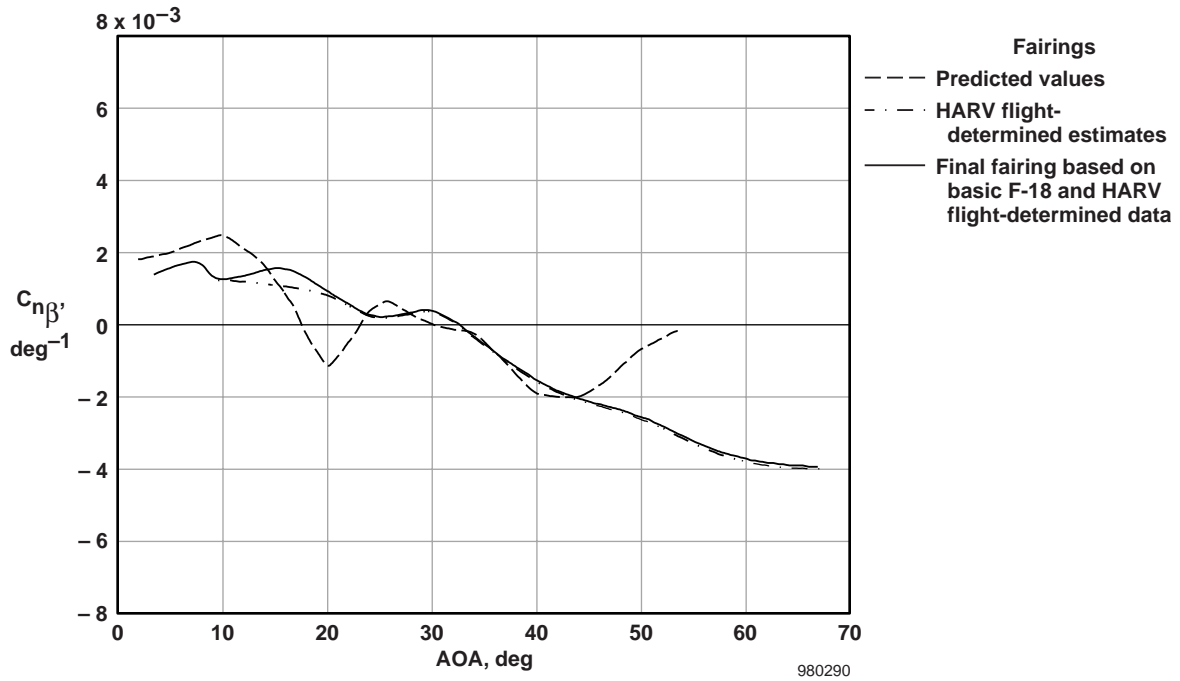
Figure 18. Concluded.



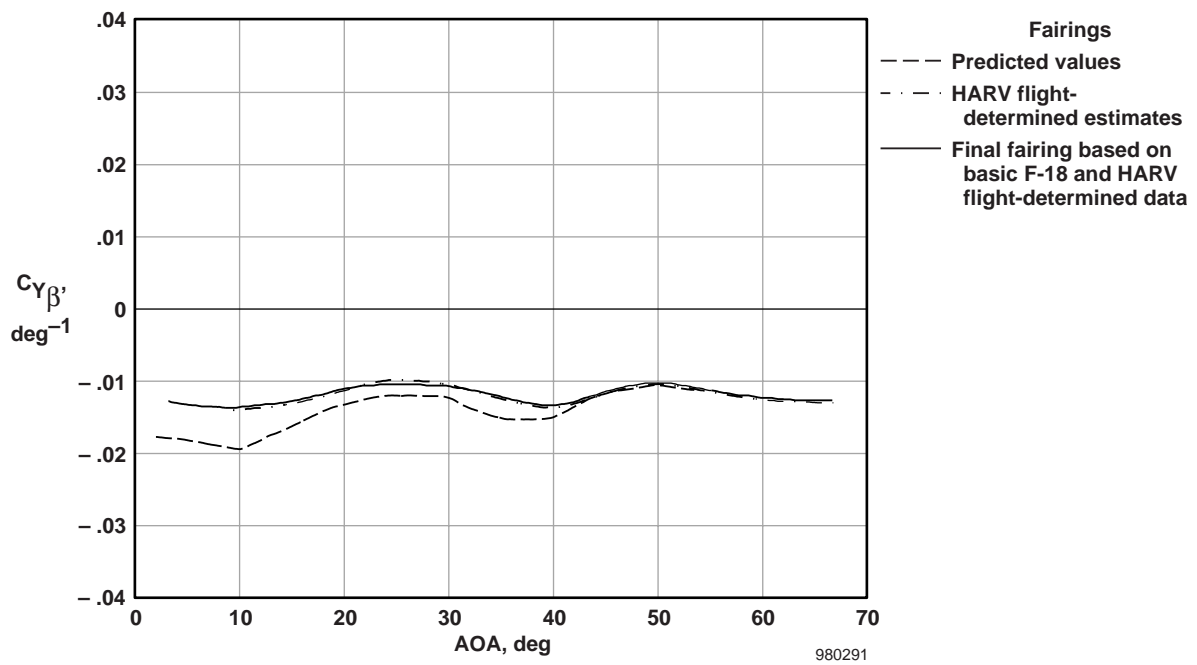
(a)  $C_{l_\beta}$  as a function of AOA.

Figure 19. Prediction and HARV sideslip derivatives as functions of AOA.



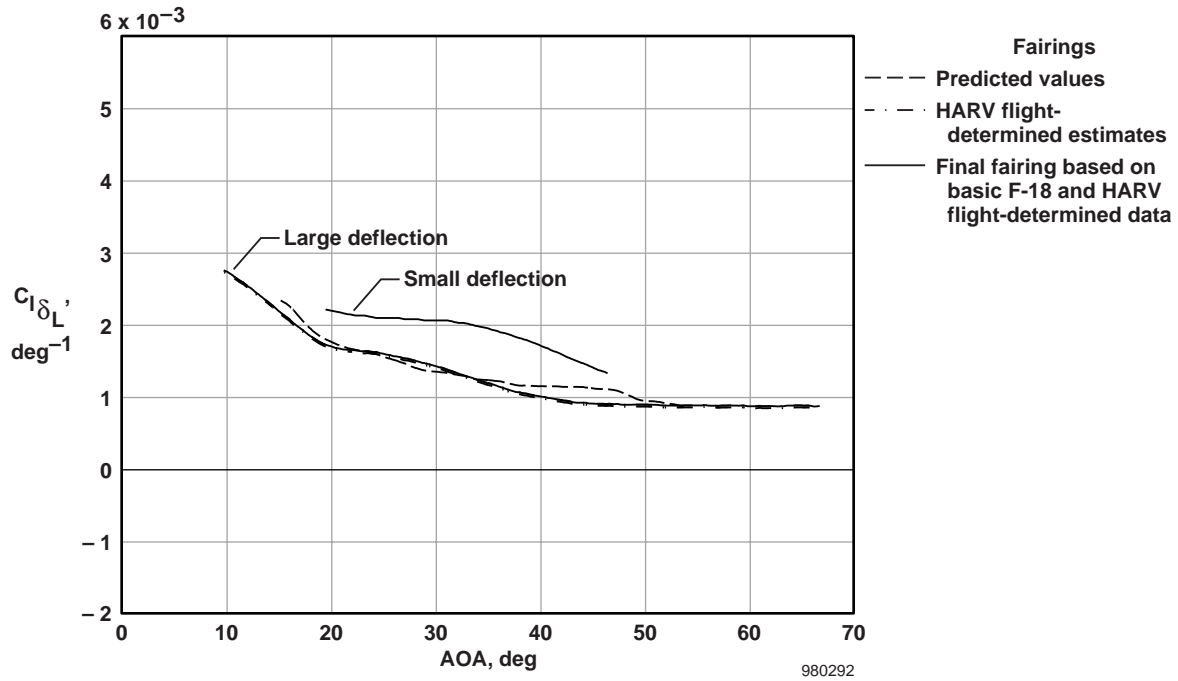


(b)  $C_{n\beta}$  as a function of AOA.

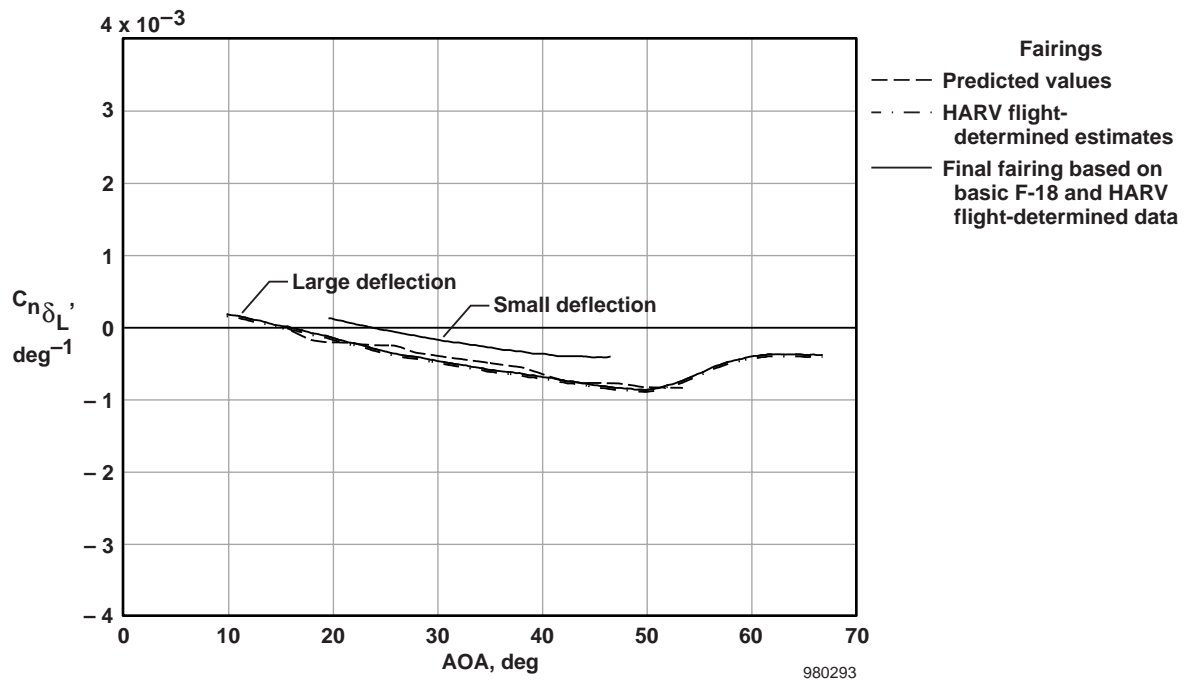


(c)  $C_{Y\beta}$  as a function of AOA.

Figure 19. Concluded.

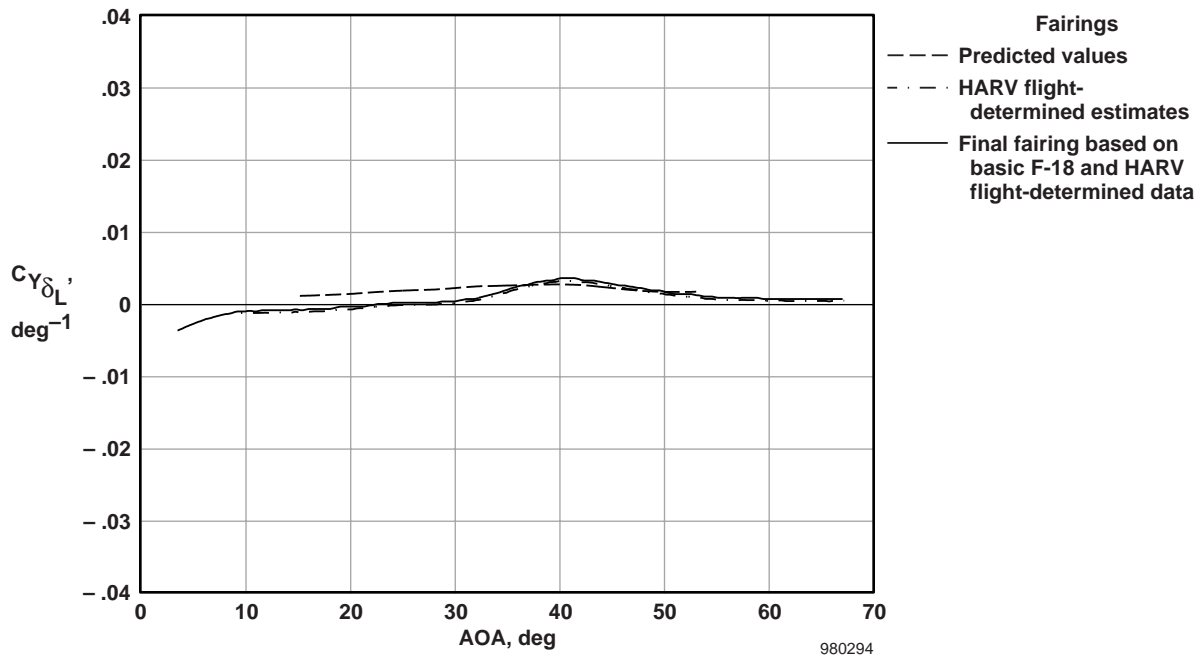


(a)  $C_{l_{\delta_L}}$  as a function of AOA.



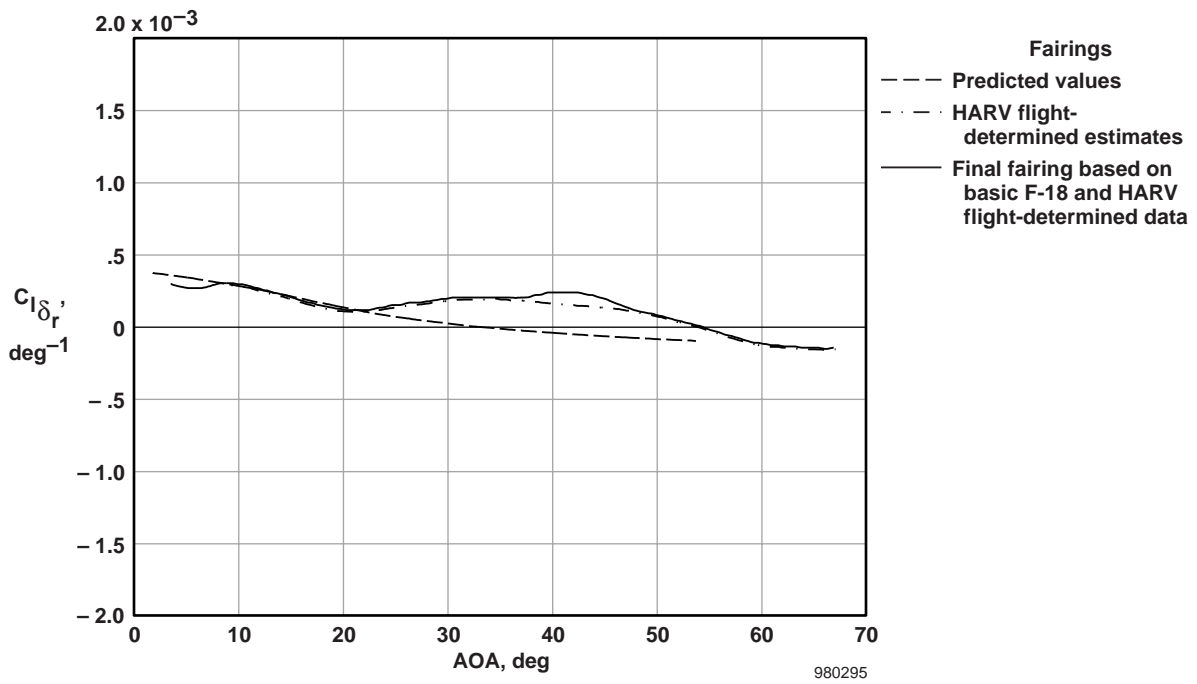
(b)  $C_{n_{\delta_L}}$  as a function of AOA.

Figure 20. Prediction and HARV equivalent lateral control derivatives as functions of AOA.



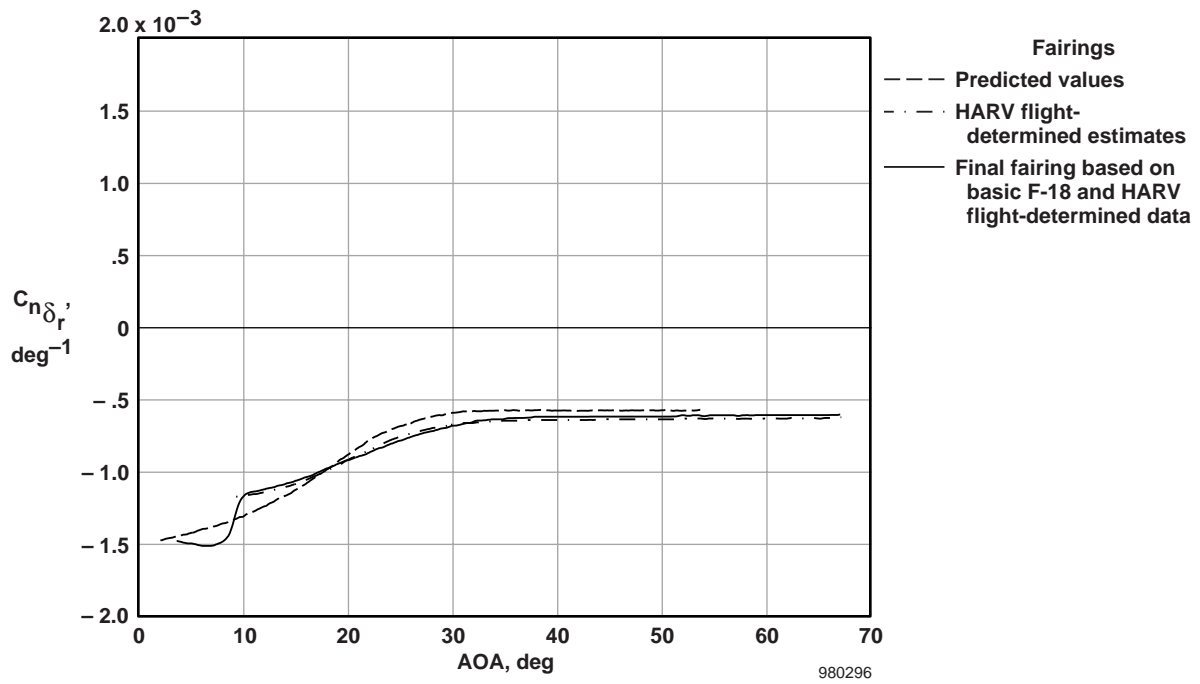
(c)  $C_{Y_{\delta_L}}$  as a function of AOA.

Figure 20. Concluded.

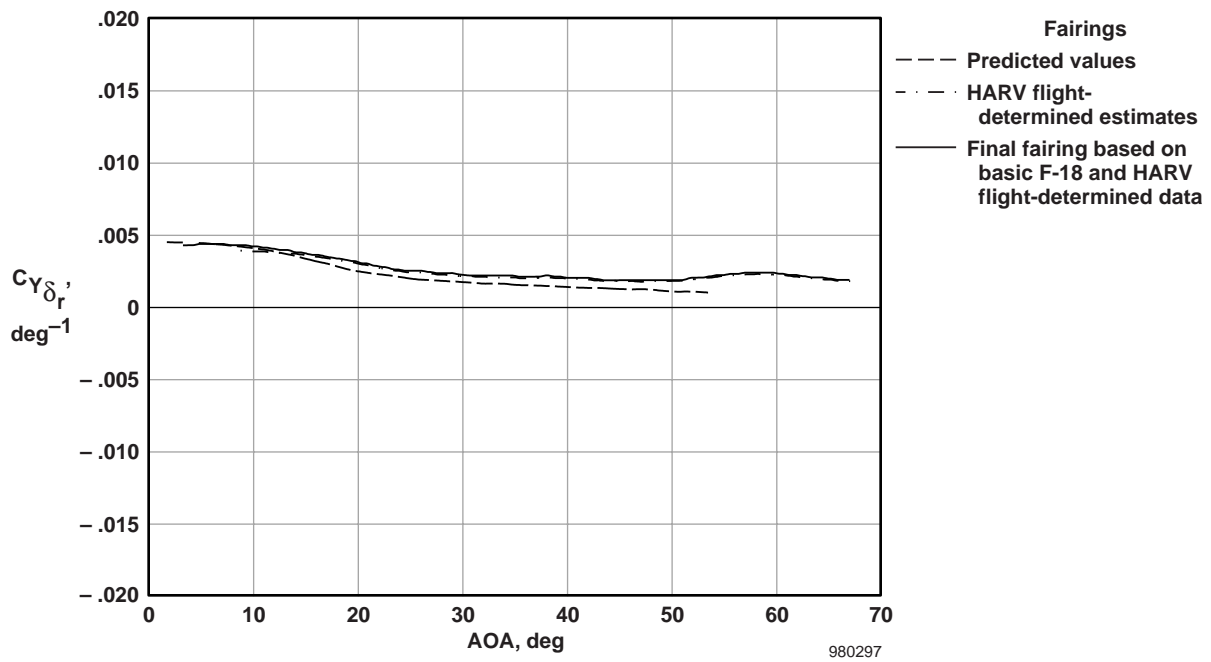


(a)  $C_{l_{\delta_r}}$  as a function of AOA.

Figure 21. Prediction and HARV rudder derivatives as functions of AOA.

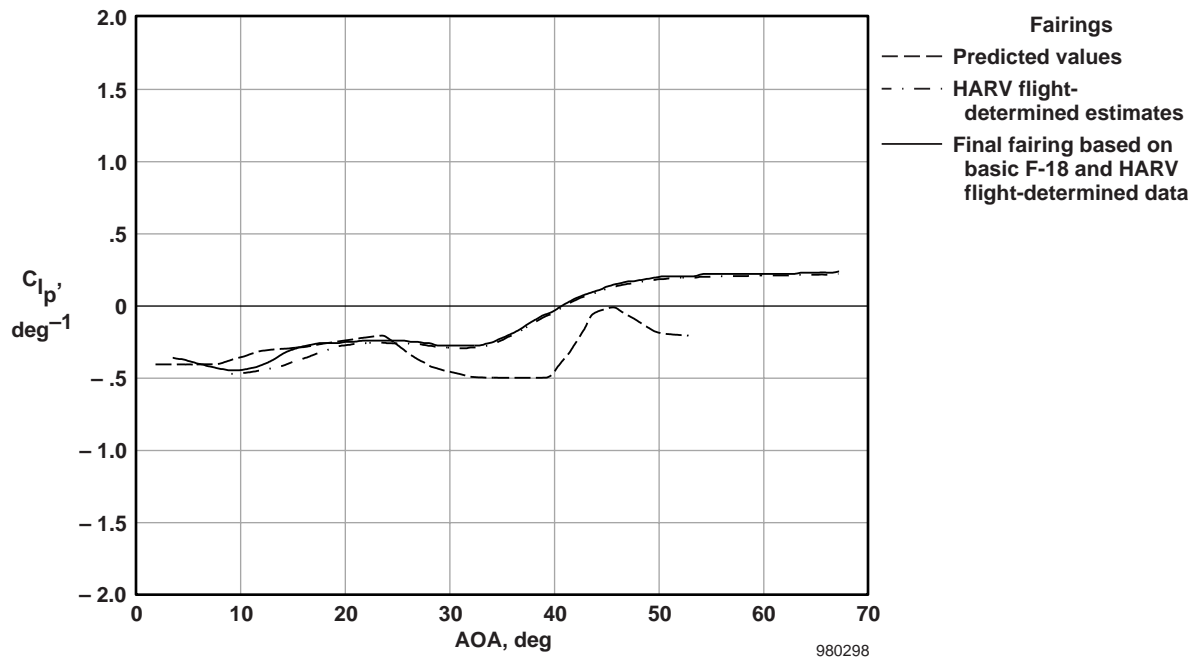


(b)  $C_{n_{\delta_r}}$  as a function of AOA.

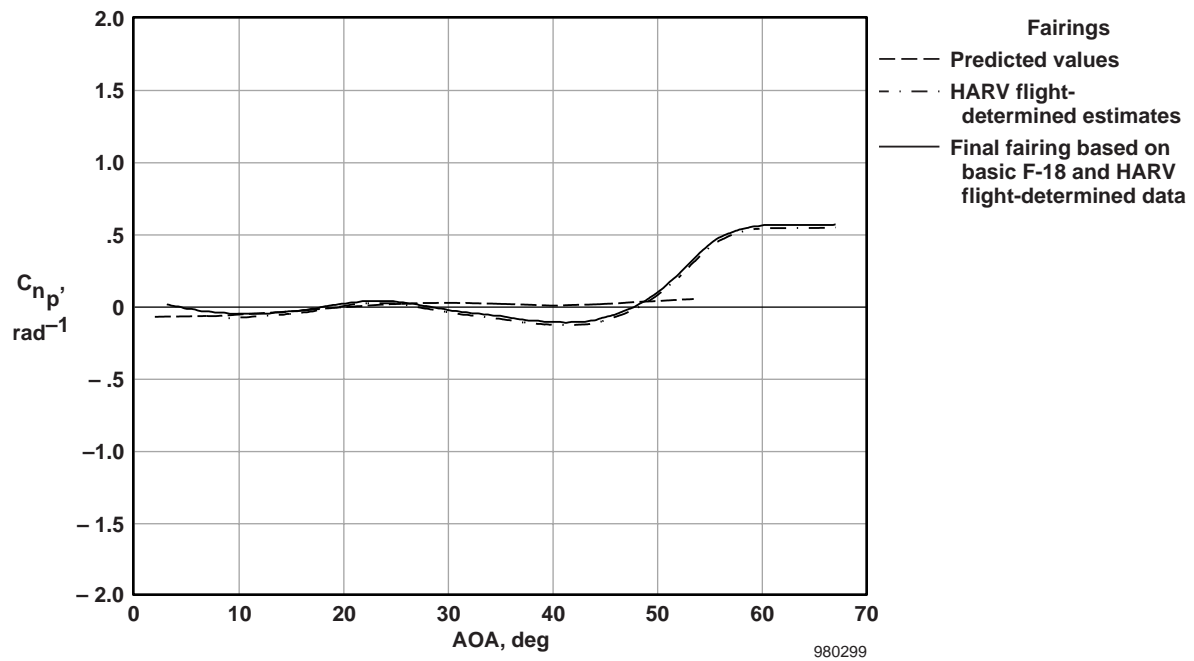


(c)  $C_{Y_{\delta_r}}$  as a function of AOA.

Figure 21. Concluded.

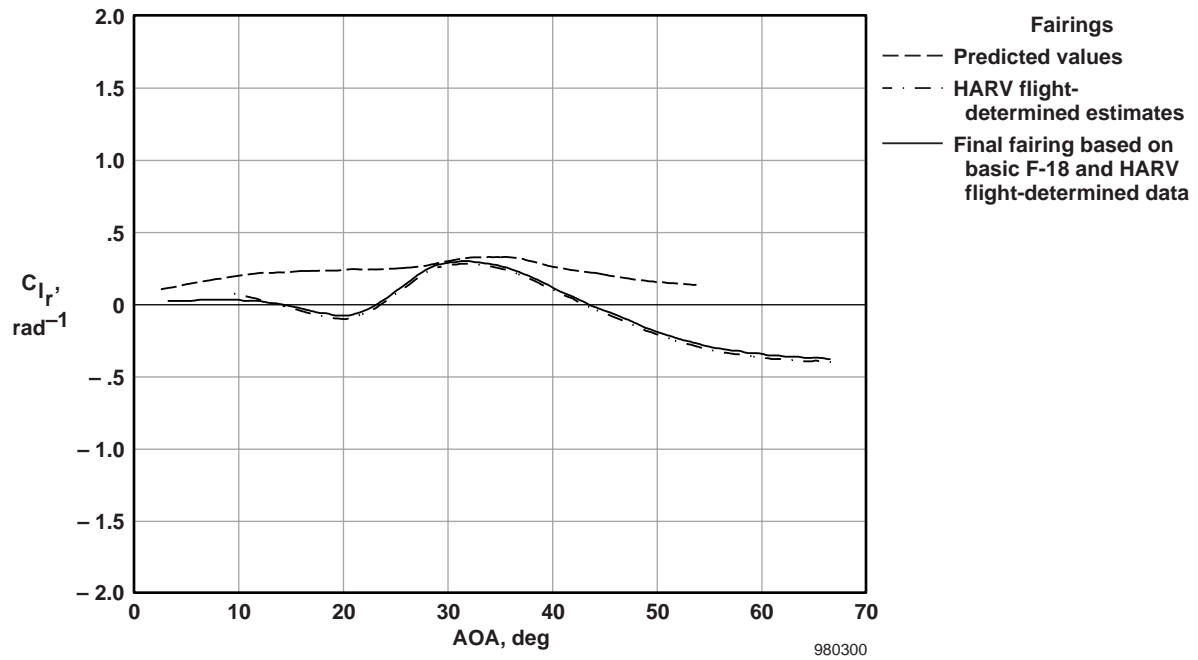


(a)  $C_{l_p}$  as a function of AOA.

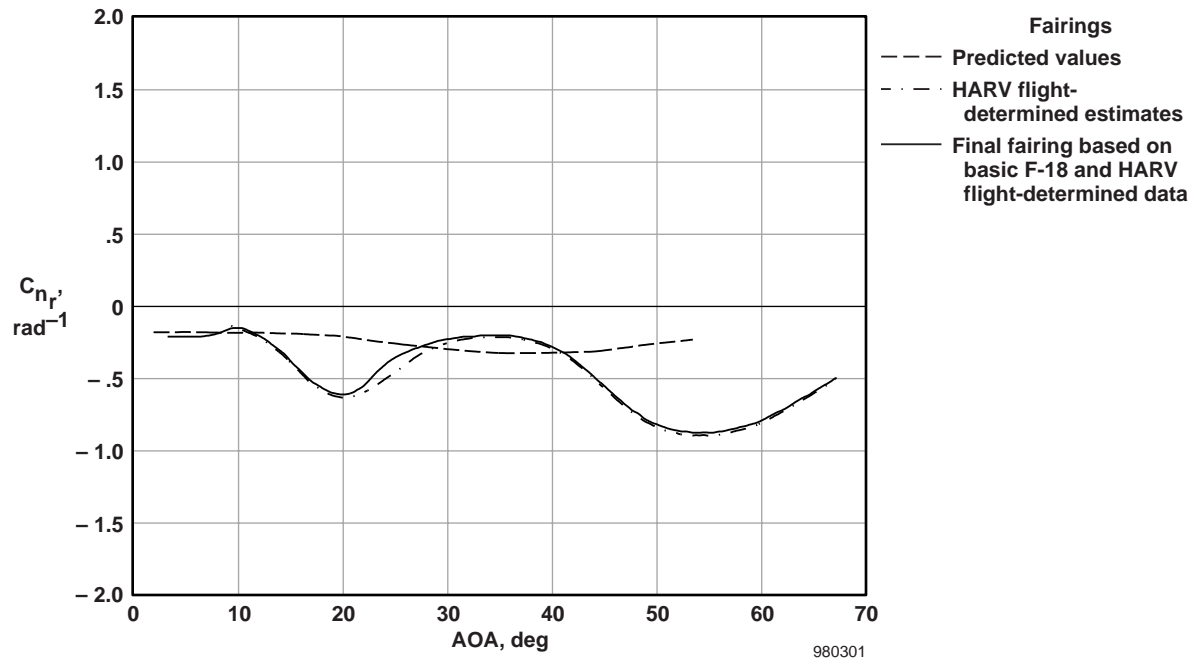


(b)  $C_{n_p}$  as a function of AOA.

Figure 22. Prediction and HARV rotary derivatives as functions of AOA.

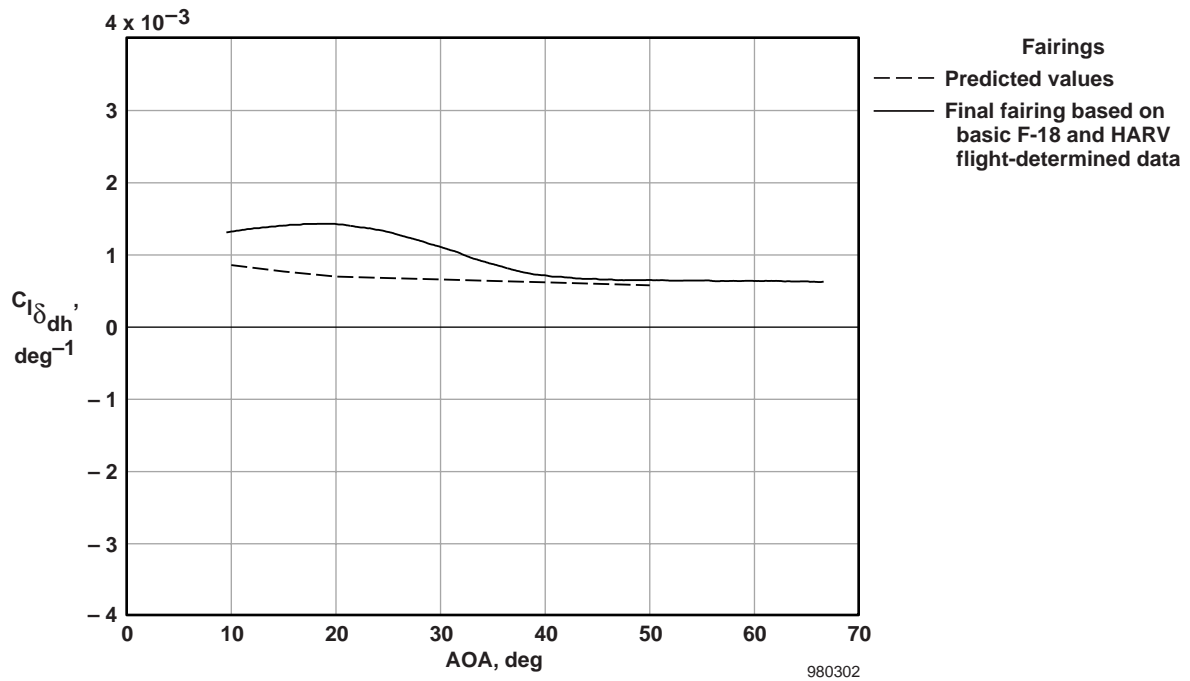


(c)  $C_{l_r}$  as a function of AOA.

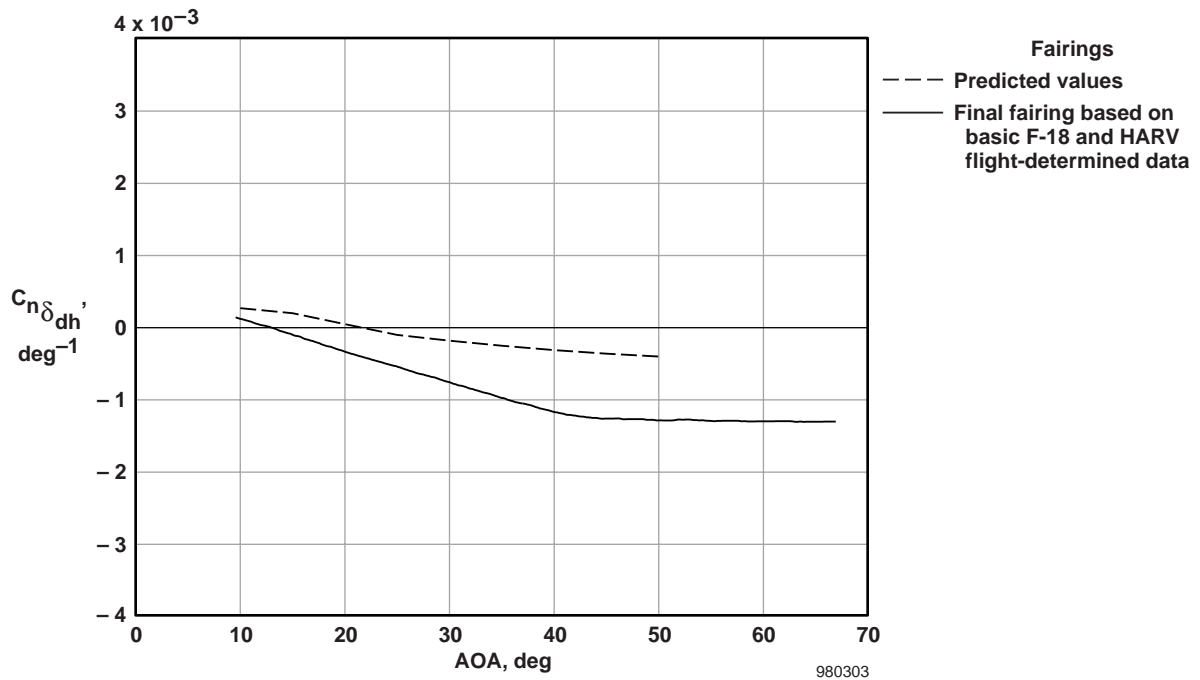


(d)  $C_{n_r}$  as a function of AOA.

Figure 22. Concluded.

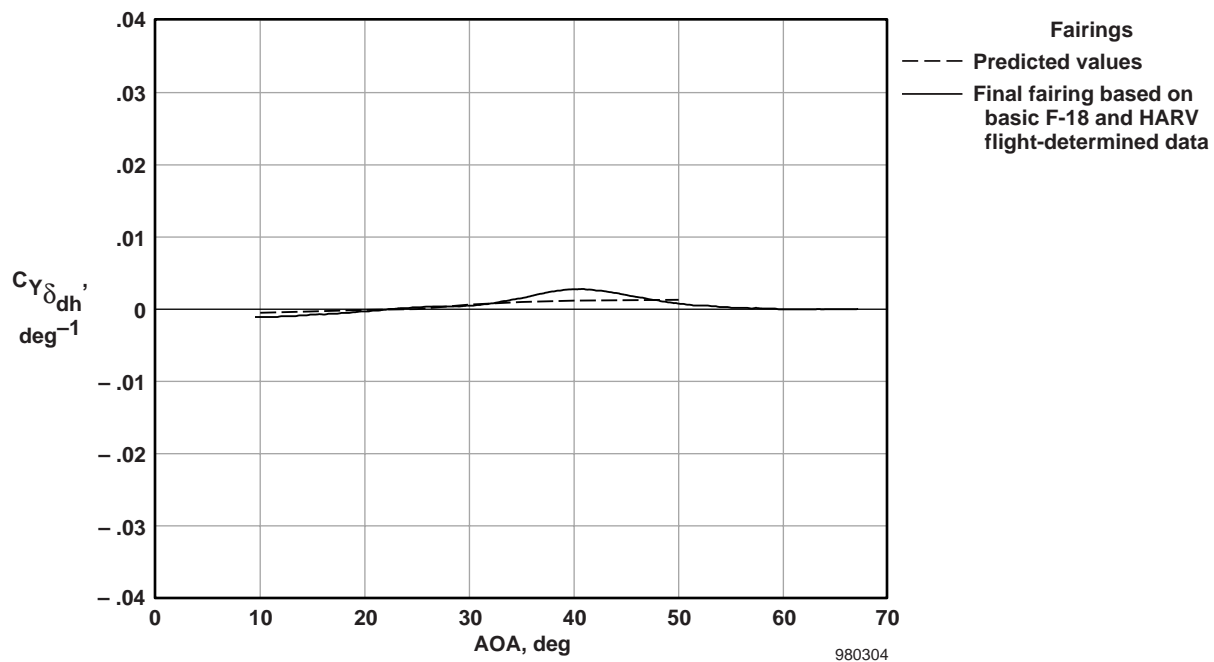


(a)  $C_{l_{\delta_{dh}}}$  as a function of AOA.



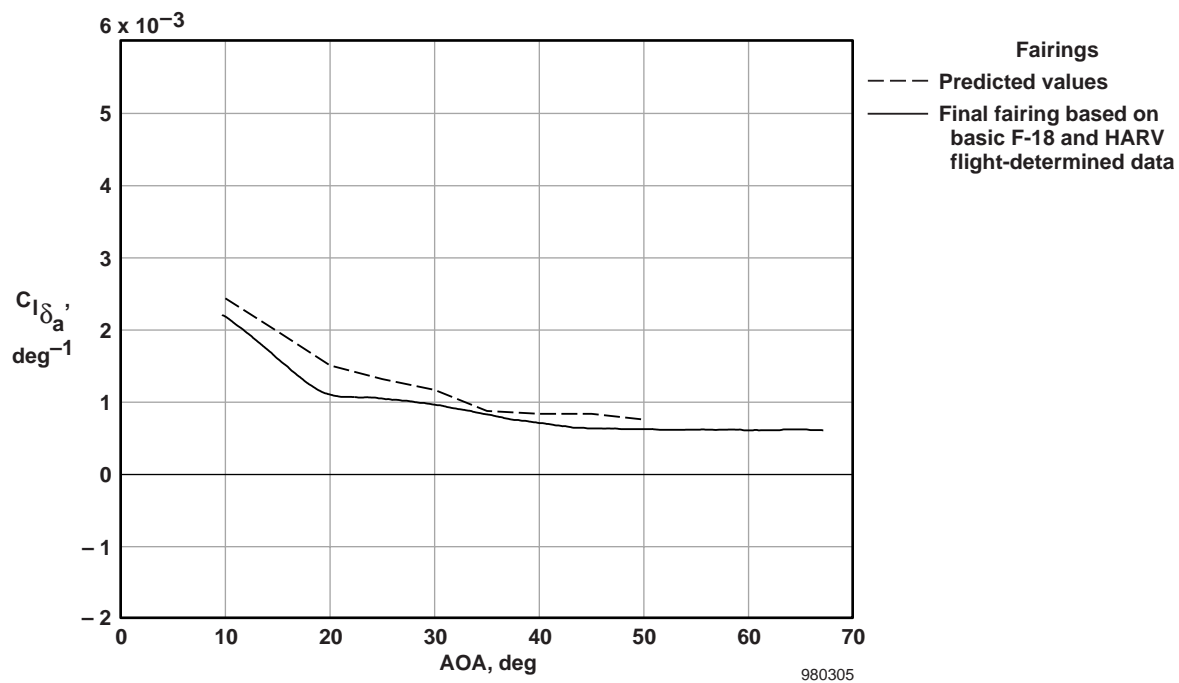
(b)  $C_{n_{\delta_{dh}}}$  as a function of AOA.

Figure 23. Prediction and HARV differential horizontal stabilator derivatives as functions of AOA.



(c)  $C_{Y_{\delta_{dh}}}$  as a function of AOA.

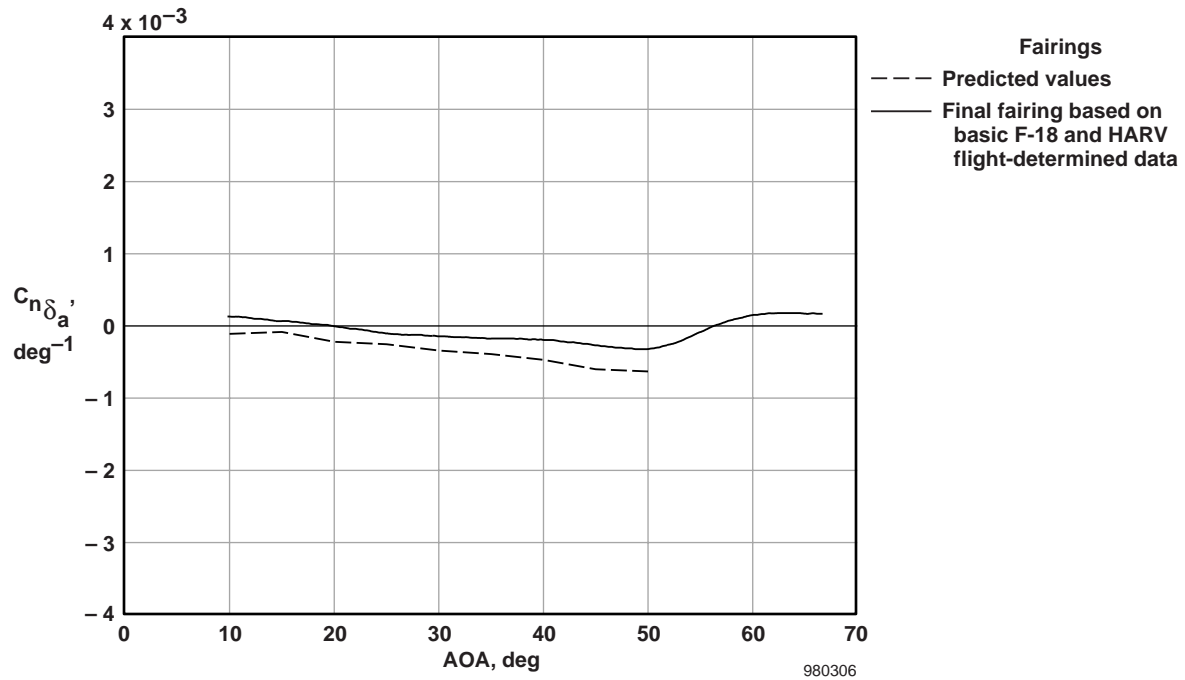
Figure 23. Concluded.



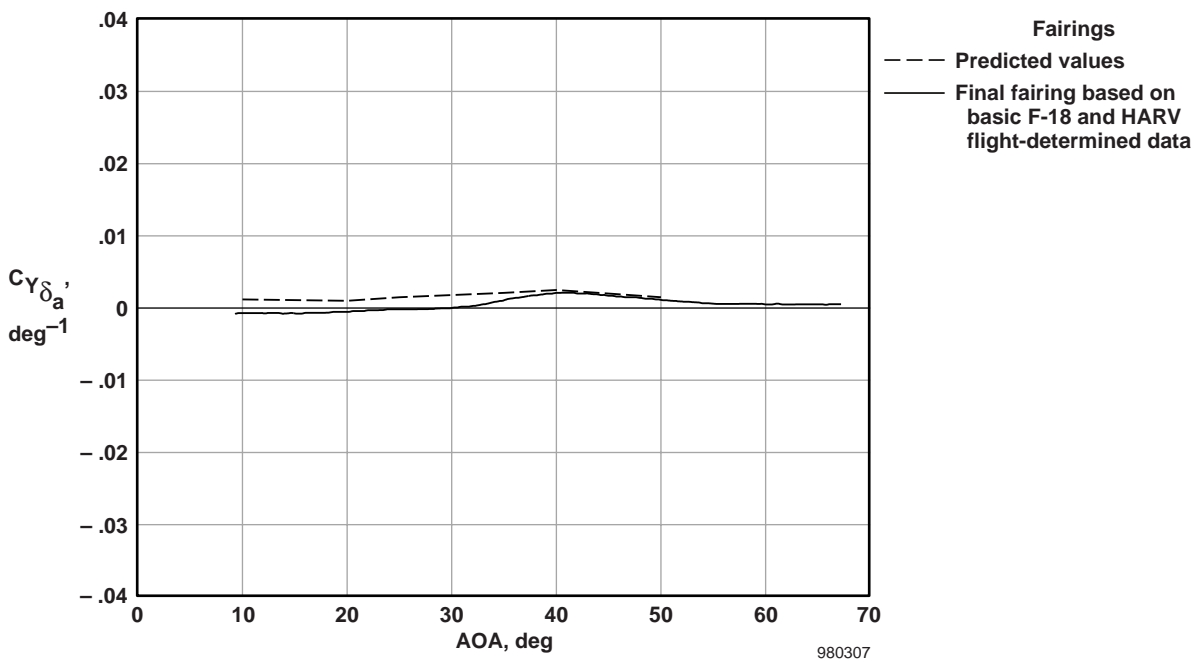
(a)  $C_{l_{\delta_a}}$  as a function of AOA.

Figure 24. Prediction and HARV aileron derivatives as functions of AOA.





(b)  $C_{n\delta_a}$  as a function of AOA.



(c)  $C_{Y\delta_a}$  as a function of AOA.

Figure 24. Concluded.

REPORT DOCUMENTATION PAGE			Form Approved OMB No. 0704-0188	
Public reporting burden for this collection of information is estimated to average 1 hour per response, including the time for reviewing instructions, searching existing data sources, gathering and maintaining the data needed, and completing and reviewing the collection of information. Send comments regarding this burden estimate or any other aspect of this collection of information, including suggestions for reducing this burden, to Washington Headquarters Services, Directorate for Information Operations and Reports, 1215 Jefferson Davis Highway, Suite 1204, Arlington, VA 22202-4302, and to the Office of Management and Budget, Paperwork Reduction Project (0704-0188), Washington, DC 20503.				
1. AGENCY USE ONLY (Leave blank)		2. REPORT DATE January 1999		3. REPORT TYPE AND DATES COVERED Technical Paper
4. TITLE AND SUBTITLE Flight-Determined, Subsonic, Lateral-Directional Stability and Control Derivatives of the Thrust-Vectoring F-18 High Angle of Attack Research Vehicle (HARV), and Comparisons to the Basic F-18 and Predicted Derivatives			5. FUNDING NUMBERS  WU 529-50-04-00-RR-00-000	
6. AUTHOR(S)  Kenneth W. Iliff, Kon-Sheng Charles Wang				
7. PERFORMING ORGANIZATION NAME(S) AND ADDRESS(ES)  NASA Dryden Flight Research Center P.O. Box 273 Edwards, California 93523-0273			8. PERFORMING ORGANIZATION REPORT NUMBER  H-2252	
9. SPONSORING/MONITORING AGENCY NAME(S) AND ADDRESS(ES)  National Aeronautics and Space Administration Washington, DC 20546-0001			10. SPONSORING/MONITORING AGENCY REPORT NUMBER  NASA/TP-1999-206573	
11. SUPPLEMENTARY NOTES  Kon-Sheng Charles Wang is a member of the technical staff of The Aerospace Corporation, P.O. Box 92957, Los Angeles, CA 90009-2957.				
12a. DISTRIBUTION/AVAILABILITY STATEMENT  Unclassified—Unlimited Subject Category 08			12b. DISTRIBUTION CODE	
13. ABSTRACT (Maximum 200 words)  The subsonic, lateral-directional, stability and control derivatives of the thrust-vectoring F-18 High Angle of Attack Research Vehicle (HARV) are extracted from flight data using a maximum likelihood parameter identification technique. State noise is accounted for in the identification formulation and is used to model the uncommanded forcing functions caused by unsteady aerodynamics. Preprogrammed maneuvers provided independent control surface inputs, eliminating problems of identifiability related to correlations between the aircraft controls and states. The HARV derivatives are plotted as functions of angles of attack between 10° and 70° and compared to flight estimates from the basic F-18 aircraft and to predictions from ground and wind-tunnel tests. Unlike maneuvers of the basic F-18 aircraft, the HARV maneuvers were very precise and repeatable, resulting in tightly clustered estimates with small uncertainty levels. Significant differences were found between flight and prediction; however, some of these differences may be attributed to differences in the range of sideslip or input amplitude over which a given derivative was evaluated, and to differences between the HARV external configuration and that of the basic F-18 aircraft, upon which most of the prediction was based. Some HARV derivative fairings have been adjusted using basic F-18 derivatives (with low uncertainties) to help account for differences in variable ranges and the lack of HARV maneuvers at certain angles of attack.				
14. SUBJECT TERMS Aerodynamics, F-18 aircraft, HARV, High angle of attack, Maximum likelihood estimation, Parameter estimation, Parameter identification, Stability and control derivatives, Thrust vectoring, Wind-tunnel predictions			15. NUMBER OF PAGES 91	
			16. PRICE CODE A04	
17. SECURITY CLASSIFICATION OF REPORT Unclassified	18. SECURITY CLASSIFICATION OF THIS PAGE Unclassified	19. SECURITY CLASSIFICATION OF ABSTRACT Unclassified	20. LIMITATION OF ABSTRACT  Unlimited	